RADAR-DERIVED FORECASTS OF CLOUD-TO-GROUND LIGHTNING OVER HOUSTON, TEXAS

A Thesis

by

RICHARD MATTHEW MOSIER

Submitted to the Office of Graduate Studies of
Texas A&M University
in partial fulfillment of the requirements for the degree of

MASTER OF SCIENCE

December 2009

Major Subject: Atmospheric Sciences

RADAR-DERIVED FORECASTS OF CLOUD-TO-GROUND LIGHTNING OVER HOUSTON, TEXAS

A Thesis

by

RICHARD MATTHEW MOSIER

Submitted to the Office of Graduate Studies of
Texas A&M University
in partial fulfillment of the requirements for the degree of

MASTER OF SCIENCE

Approved by:

Co-Chairs of Committee,	Courtney Schumacher
	Richard E. Orville
Committee Members,	Francisco Olivera
Head of Department,	Kenneth Bowman

December 2009

Major Subject: Atmospheric Sciences

ABSTRACT

Radar-derived Forecasts of Cloud-to-Ground Lightning over Houston, Texas.

(December 2009)

Richard Matthew Mosier, B.S., Texas A&M University

Co-Chairs of Advisory Committee: Dr. Courtney Schumacher
Dr. Richard E. Orville

Ten years (1997 – 2006) of summer (June, July, August) daytime (14 – 00 Z) Weather Surveillance Radar – 1988 Doppler data for Houston, TX were examined to determine the best radar-derived lightning forecasting predictors. Convective cells were tracked using a modified version of the Storm Cell Identification and Tracking (SCIT) algorithm and then correlated to cloud-to-ground lightning data from the National Lightning Detection Network (NLDN).

Combinations of three radar reflectivity values (30, 35, and 40 dBZ) at four isothermal levels (-10, -15, -20, and updraft -10°C) and a new radar-derived product, vertically integrated ice (VII), were used to optimize a radar-based lightning forecast algorithm. Forecasts were also delineated by range and the number of times a cell was identified and tracked by the modified SCIT algorithm. This study objectively analyzed 65,399 unique cells, and 1,028,510 to find the best lightning forecast criteria.

Results show that using 30 dBZ at the -20 °C isotherm on cells within 75 km of the radar that have been tracked for at least 2 consecutive scan produces the best forecasts with a critical success index (CSI) of 0.71. The best VII predictor was 0.734 kg m^{-2} on cells within 75 km of the radar that have been tracked for at least 2 consecutive scans

producing a CSI of 0.68. Results of this study further suggest that combining the radar reflectivity and VII methods can result in a more accurate lightning forecast than either method alone.

ACKNOWLEDGEMENTS

I would like to thank my committee chairs, Dr. Richard Orville and Dr. Courtney Schumacher, and my other committee member, Dr. Francisco Olivera, for their guidance and support throughout the course of this research.

Thanks also go to my friends and colleagues and the department faculty and staff for making my time at Texas A&M University a great experience. I have sincerely enjoyed my time at this great university.

I must also thank my church family, who has supported me through everything, and my family, for all of their encouragement. The most thanks must go to my wife, who has supported me in everything and encouraged me in those difficult times and very late nights.

TABLE OF CONTENTS

Page

Page

LIST OF FIGURES

FIGURE Page

FIGURE Page

FIGURE Page

LIST OF TABLES

TABLE Page

1. INTRODUCTION

1.1 The Necessity of Lightning Research

The American Meteorological Society's *Glossary of Meteorology* (Glickman 2000) defines lightning as a "transient, high-current electric discharge with path lengths measured in kilometers." Uman (1986) defined lightning as the self-propagating process of electric discharge that results from the accumulation of positive and negative space charges that typically occur within convective clouds. Lightning poses a significant threat to life and property and is therefore a concern of the National Weather Service (NWS). Curran et al. (2000) showed that lightning ranked second in weather-related deaths in the United States between 1959 and 1991 (Table 1.1) and ranked first in some years (Table 1.2). Texas was ranked in the top ten in lightning fatalities (3rd), casualties (7th), injuries (8th), and damage reports (9th) yet there has been only one study (Clements and Orville 2008) that has examined lightning forecasting within the state. More recent studies show years show similar trends. For example, the 2008 NWS Weather Fatalities, Injury, and Damage Statistics 30-year (1978 – 2007) average has lightning as the second most frequent cause of weather related fatalities with an average of58 fatalities per year. As a result, the forecasting of cloud-to-ground (CG) lightning strikes is of great importance. In addition, the National Lightning Safety Institute (NLSI) estimates lightning related damage in the 4-5 billion dollar range annually across the United States.

This thesis follows the style of *Journal of Atmospheric Sciences.*

As a result, the forecasting of cloud-to-ground (CG) lightning, i.e. lightning that reaches the surface, is of great importance.

1.1.1 Thunderstorm Charge Structure

A "thunderstorm" is defined as a local storm that is accompanied by thunder and lightning produced by a cumulonimbus cloud (Glickman 2000). The presence of lightning indicates that there must be some type of charge separation within the storm. C.T.R Wilson (1916, 1920, 1929) conducted influential research regarding thunderstorm charge structure in the early twentieth century. His studies showed a positive dipole (i.e. the positive charge above the negative charge) structure in thunderstorms. However, this result was controversial since measurements at the surface, at a distance from a thunderstorm, can produce conflicting results (MacGorman and Rust 1998). Wormell (1930, 1939) concluded that most storms had a positive dipole, but a few had a negative dipole (i.e. the negative charge above the positive charge). In-situ measurements were made by Simpson and Scrase (1937) and Simpson and Robinson (1947) since ground-based measurements were inconclusive. Their results suggested that there is typically a positive dipole structure, with an additional area of positive charge below the main negative region. They hypothesized that electrified storms had: 1) a small region (0.5 km radius) of positive charge, approximately +4C total, around the 0°C level, 2) a negatively charged region, with an approximately 1 km radius and -20C total charge, around the -7°C level, and 3) another positively charged region, with an approximately 2km radius and +24C total charge, where temperatures were less than -20°C. It is this "dipole/tripole" structure, shown in Figure 1.1, which is generally accepted as the

conceptual model for thunderstorms. More recently, additional research has suggested the possibility of an additional layer of negative charge on the upper cloud boundary (Krehbiel 1986, Marshall et al. 1989), called the screening layer. The actual structure of the charge separation can be very complex (Zigeler and MacGorman 1994), but the dipole/tripole plus screening layer structure is generally used when examining the gross charge distribution of a thunderstorm.

1.1.2 Thunderstorm Electrification

Any process of cloud electrification must include both a small-scale process that electrifies hydrometeors (i.e.,liquid or frozen water particles) and a process that creates the charge separation observed (Rakov and Uman 2006). MacGorman and Rust (1998) list a number of possible mechanisms including ion capture, inductive charging of rebounding particles, non-inductive graupel-ice collisions, convection and charging during the melting of frozen hydrometeors. One of the most widely accepted mechanisms at this time is non-inductive graupel-ice collision. This theory, first proposed by Reynolds et al. (1957), also called non-inductive charging (NIC), has gained recognition because it does not require an initial electric field to polarize the hydrometeors. The inductive charging theory requires an initial electric field and it is commonly believed that the earth's fair weather electric field, which is 0.1 kV near the surface (Rakov and Uman 2006), is not strong enough to create the charging observed within thunderstorms (MacGorman and Rust 1998). Lab results show that NIC is a more reasonable option (Reynolds et al. 1957, Takahashi 1978, Gaskell and Illingworth 1980, Jayaratne et al. 1983).

Takahashi (1978) presented groundbreaking work on NIC. Takahashi showed that high electrification occurs when riming probes rotate in an environment containing both ice crystals and supercooled droplets, but the sign and magnitude of the charge was dependent on temperature and cloud water content (CWC). Figure 1.2 shows the results of this research. He also discusses the physical mechanisms of charge separation which are based on the thermoelectric effect. The thermoelectric effect results in protons moving in directions determined by the temperature gradient such that the warmer areas will be more negatively charged and colder areas will be more positively charged. Figure 1.3 shows the three physical mechanisms he discusses.

The first mechanism occurs at low temperature and CWC (below 0.1 g m^{-3}). Since latent heat is released during riming, the temperature of the surface will be warmer and the thermoelectric effect will cause the protons to move towards the interior of the rime. Therefore, broken ice crystals that impact the rime will be negatively electrified while the rime will be positively electrified (Figure 1.3a).

The second mechanism occurs at CWC between 0.1 to 4 g m^{-3} and charges the rime negatively. The rime receives a negative charge when ice crystals impact the warm riming surface. Protons move toward the ice crystals because of the warmer temperature of the rime. Therefore when an ice crystal impacts the rime a slightly positive charge is transferred to the ice crystal (Figure 1.3b).

The third mechanism occurs when CWC is greater than 4 g m^{-3} and charges the rime positively. Since the CWC is high, a thin water layer exists on the riming surface. This water surface tends to be more negatively charged near its surface and more positively charged near the intersection of the water and riming surface. Again, this is

due to the thermoelectric effect where more H^+ ions move towards the ice (riming surface) while more OH^- ions remain on the thin water layer. As a result, when ice crystals collide with the rime they remove portions of the negatively charged water layer (Figure 1.3c).

Takahashi (1978) concluded that the electric fields observed in thunderstorms result from a process of graupel formation and collisions with ice crystals within the updraft of a thunderstorm. Higher electrification in the cloud regions with lower temperatures is expected due to the abundance of ice crystals.

Therefore, the electric structure observed by Simpson and Scrase (1937) and Simpson and Robinson (1941) is due to the negatively charged graupel falling in the updraft column while the ice crystals are lofted into the anvil cloud due to their different terminal velocities (Williams 2001). When temperatures increase above -10°C, positive graupel electrification occurs. As a result, the lower positive charge and the main negative charge result from graupel charging, while the upper positive is due to the lofting of the positively charged ice crystals.

However, temperature and CWC are not the only elements that control charge transfer. Jayarante et al. (1983) and Keith and Saunders (1990) found that while charge transfer depends on temperature and CWC, it also depends on the size of the ice crystal intersecting with the graupel, the speed of the impact, and the purity of the water particles. For example, Keith and Saunders (1990) showed an increase in charge transfer resulting from an increase of ice crystal diameter. Further studies (Jayaratne and Saunders 1985, Baker et al. 1987) concluded that liquid particles that did not collide with the graupel did not have an effect on the charge transfer. Therefore subsequent studies

(Saunders et al. 1991, Saunders and Brooks 1992) adjusted the CWC to account for the particles that did not collide with the graupel due to aerodynamic forces. This adjusted CWC was called the effective liquid water content. This new parameter is used on the plot in Figure 1.4, which places the results from Saunders et al. (1991) onto the results from Takahashi (1978). Differences are noted in the figure, mainly in the lower left of the figure where the CWC is small and the temperatures are warm. The reason for these differences are not completely known, but are expected to be a result of the difficulty in obtaining good measurements at low CWC and warm temperatures (MacGorman and Rust 1998).

Cloud water content and aerodynamic forces are not the only factors affecting the effective liquid water content. Brooks et al. (1997) found that an increase in the velocity of the riming target increased both the impact velocity of ice crystals and the rate of collisions with cloud droplets. As a result, they suggested that the rime accretion rate was the main factor that influenced charge transfer, and that the effective liquid water content was a method of including this factor into the charge transfer relationship.

MacGorman and Rust (1998) provide a summary of the graupel-ice charging mechanism: 1) a large rimed particle and a small amount of CWC are needed for significant charging, 2) graupel become positively charged when CWC is high, 3) graupel becomes negatively charged when CWC is low, 4)graupel charge positively, for most CWC, at 0 °C, 5) increasing the ice crystal size increases the amount of charge transfer during a collision, 6) results from an individual collision may be different than the mean results found in laboratory studies (i.e. Takahashi 1978, Jayaratne et al 1983), and 7) charge transfer is strongly affected by the purity of the ice involved in the collision.

The NIC theory provides a viable method for producing the gross charge structure observed in thunderstorms, but it is largely based on laboratory studies and there is still uncertainty related to the exact microphysical processes that induce the NIC process. In-situ measurements by Dye et al. (1986) showed that the NIC method is a probable method of charge separation between -10 and -20 °C. Studies from several other field campaigns (Goodman et al. 1988, Carey and Rutledge 1996, Carey and Rutledge 2000) also suggest a strong correlation between precipitation-sized ice mass (i.e. graupel) and the production of lightning, which strengthens the viability of the NIC theory. Peterson et al. (2005) give a brief overview of how the NIC theory works within thunderstorms. First, you need a vigorous updraft (also noted in Takahashi 1978), which leads to mixed phase microphysics. The mixed phase microphysics then lead to small- and large-scale charge separations (methods of separation described above from Takahashi). This charge separation often results in lightning production.

1.1.3 Lightning

There are two types of lightning: intra-cloud (IC) and cloud-to-ground (CG). An IC flash occurs completely within a cloud while a CG flash lowers cloud charge to the ground. This study only focuses on CG flashes. As a result, most of the discussion here will be related only to CG flash processes. Figure 1.5 shows the four types of CG lightning: (a) downward negative lightning, (b) upward negative lightning, (c) downward positive lightning, and (d) upward positive lightning. Type (a), downward negative lightning, accounts for 90 percent of all CG flashes (Orville and Huffines 2001, Rakov and Uman 2006). Type (c), downward positive lightning, accounts for approximately 10

percent of all CG flashes. The other two types, (b) and (d), only occur from objects that are greater than 100 m tall. As a result of their height, these objects "trigger" lightning as the charge propagates from their tops. A negative (positive) flash brings negative (positive) charge to ground.

Figure 1.6 shows a typical lightning flash process. This process begins with the initial breakdown within the cloud. The breakdown process is not well understood and may be the result of an IC discharge that bridges the main negative charge region with the lower positive charge region (Rakov and Uman 2006). After this breakdown process, a downward-moving leader is formed. During the first stroke of a lightning flash this leader is called the "stepped leader" because it appears to "step" down towards the ground discretely. These steps are normally 1 μs in duration and tens of meters in length and are typically 20 to 50 μs apart (Rakov and Uman 2006). The stepped leader forms a conducting path between the cloud and the ground. The first stroke leader is typically branched, as the process attempts to follow the path of least resistance. As a result, the first stroke typically stores more charge along its path than subsequent strokes.

As the leader approaches the ground, the electric field increases and eventually reaches the point of breakdown. At this point, upward-connecting leaders initiate from various objects such as the ground, trees, and houses to begin the attachment process. The attachment process ends whenever contact is made between the downward and upward moving leaders. At this point, the first return stroke begins.

The return stroke then acts to transport the charge stored in the channel created by the stepped-leader to the ground. The average peak current of the return stroke is 30 kA (Berger et al. 1975, Rakov and Uman 2006) and occurs on the order of microseconds. If

the first stroke is the only stroke in a flash, the lightning is called a single-stroke flash. Most negative flashes are composed of more than one stroke while most positive flashes are composed of only one stroke.

In a multiple stroke flash, the residual channel created by the first stroke is then navigated by an additional leader that moves continuously. This leader is called a dart leader because of its high speed and lack of stepping. In most situations, the dart leader travels along the channel without branching. Without the branching, less charge is stored within the channel and the peak current is typically much less than that of the initial stroke. In some cases, the dart leader begins stepping as it nears the ground. This process is known as a dart-stepped leader. As the dart leader or dart-stepped leader moves close to the ground, the attachment process is largely the same as during the first-stroke process.

This dart-leader return stroke process can repeat numerous times. A typical lightning flash contains 3 to 5 strokes (Rakov and Uman 2003). The number of strokes within a flash is referred to as the multiplicity of the flash. Flash multiplicity ranges from 1 to as high as 26. The time between strokes is on the order of a millisecond. This short lapse time between strokes is what causes the lightning to appear as if it "flickers" to the human eye. For this study, the term "flash" or "lightning flash" represents the entire lightning event. The term "strike" may also be used in this sense. The term "stroke" is used to distinguish multiple discharges within the same flash.

1.2 Radar Meteorology

The term “radar” is actually acronym for radar detection and ranging. This term was originally suggested by S. M. Taylor and F. R. Furth of the United States Navy during World War II (see Chapter 1, Doviak and Zrnic (1993) or Chapter 1, Rinehart (2004) for a detailed description of the history of radar). The term “radio” is generally applied to electronic radiation with wavelengths approximately 20km to less than a mm. The major development phase of radar technology took place during World War II when detection of aircraft became very important. A radar works by sending out an electromagnetic wave via the antenna and then receiving the return signal after the electromagnetic wave has reflected off of an object. Early radars used a two antenna system where one antenna sent the electromagnetic signal continuously and the other listened for the return signal continuously. However, modern weather radars accomplish this task with only one antenna for transmitting and receiving. The signal is transmitted via the antenna using a short pulse of energy. The system then waits a specified time period before sending another pulse. During this waiting period, the antenna is receiving any return signal from the first pulse. Since the electromagnetic radiation travels at the speed of light, the wait time between pulses is short.

The return signal is then processed using complex electromagnetic theory to infer the size of the target. A derivation of the radar equation follows. The derivation starts by considering an isentropic antenna. The power radiated by an isentropic antenna moves away from the source in all directions at the speed of light, creating an expanding sphere of energy. Using the surface area of a sphere, the power per unit area, or power density, can be expressed

$$S = \frac{p_t}{4\pi r^2} \tag{1.1}$$

where S is the power density, p_t is the transmitted power, and r is the distance to the radiation source. Generally, weather radar systems do not use an isentropic antenna, but a directional antenna, therefore the antenna's gain must be considered. The gain of an antenna is the ratio of power that is actually received from the directional antenna to the power that would have been received from an isentropic antenna. Defined mathematically,

$$g = \frac{p_d}{p_i} \tag{1.2}$$

where g is the gain, p_d is the power from the directional antenna, and p_i is the power from an isentropic antenna. Considering a point target with cross-sectional area A_σ, the power intercepted by the target is

$$P_\sigma = S \cdot g \cdot A_\sigma \tag{1.3}$$

where P_σ is the power intercepted by the target, S is the power density, g is the antenna gain, and A_σ is the cross-sectional area of the target. Combining the power intercepted (Equation 1.3) with the power density (Equation 1.1) gives

$$P_\sigma = \frac{p_t \cdot g \cdot A_\sigma}{4\pi r^2} \tag{1.4}$$

where the variables are the same as defined previously. The target will then reradiate the energy it just received. Assuming the target radiates equally in all directions then the power density from the target will be

$$S_\sigma = \frac{P_\sigma}{4\pi r^2} \tag{1.5}$$

where S_σ is the power density from the target, P_σ is the power intercepted by the target, and r is the distance from the target. Therefore the power received by the antenna from the point target can then be defined

$$P_r = S_\sigma \cdot A_e = \frac{P_\sigma}{4\pi r^2} \cdot A_e \tag{1.6}$$

where P_r is the power received by the antenna and A_e is the effective area of the antenna. Using Equation 1.4 in Equation 1.6 yields

$$P_r = \frac{P_t \cdot g \cdot A_\sigma \cdot A_e}{4\pi r^2} \tag{1.7}$$

For a circular parabolic antenna, the most common antenna used for weather radar, the effective area is

$$A_e = \frac{g\lambda^2}{4\pi} \tag{1.8}$$

where λ is the wavelength. Combining Equation 1.7 with Equation 1.8 yields

$$P_r = \frac{P_t \cdot g^2 \cdot \lambda^2 \cdot A_\sigma}{64\pi^3 r^4} \tag{1.9}$$

The last step in obtaining the radar equation for point targets is to use the backscattering cross-sectional area,σ, of the target instead of its visual cross-sectional area A_σ. The visual cross-sectional area alone cannot be considered because of the complex scattering properties of targets due to their size, composition, and shape. Scattering properties are also a function of the wavelength which must be considered when calculating the return power. The calculation of the cross-sectional area is usually very complicated. However, for most radar systems, spherical Rayleigh scattering is assumed, which yields

$$\sigma = \frac{\pi^5 |K|^2 D^6}{\lambda^4} \tag{1.10}$$

where D is the diameter of a spherical target, and $|K|^2$ is the dielectric of the target. Targets are initially assumed to be water so the dielectric is usually taken to be 0.93. The final form of the radar equation for point targets is generally written

$$P_r = \frac{P_t \cdot g^2 \cdot \lambda^2 \cdot \sigma}{64\pi^3 r^4} \tag{1.11}$$

where all the terms are as previously defined. Equation 1.11 will work when considering only one spherical target. However, for weather radar there are many spherical targets (i.e. raindrops or hail) instead of just one. This complicates the calculation of the backscattering cross-sectional area. Therefore, the backscattering cross-sectional area is redefined to the total backscattering cross-section

$$\sigma_T = V \cdot \sum_{vol} \sigma_i \tag{1.12}$$

where σ_T is the total backscattering cross-section, V is the sample volume, and σ_i is the backscattering cross-sectional area per unit volume. The sample volume, V, is defined by

$$V = \pi \frac{r\theta}{2} \frac{r\phi}{2} \frac{h}{2} = \frac{\pi \cdot r^2 \cdot \theta \cdot \phi \cdot h}{8} \tag{1.13}$$

where θ and ϕ are related to the beamwidth, h is the transmitter pulse length, and r is the distance to the target. When the Guassian beam shape is accounted for Equation 1.13 becomes

$$V = \frac{\pi \cdot r^2 \cdot \theta \cdot \phi \cdot h}{16\ln(2)} \tag{1.14}$$

Replacing σ in Equation 1.10 with Equation 1.12 and combining with Equation 1.14 yields the radar equation for distributed targets:

$$p_r = \frac{p_t g^2 \lambda^2 \theta \phi h \sum \sigma_i}{1024 \ln(2) \pi^2 r^2} \tag{1.15}$$

Finally, a term called the radar reflectivity factor,

$$z = \sum_i D_i^6 \tag{1.16}$$

is combined with Equation 1.10 and placed into Equation 1.15 to yield:

$$p_r = \frac{\pi^3 p_t g^2 \theta \phi h |K|^2 z}{1024 \ln(2) \lambda^2 r^2} \tag{1.17}$$

Therefore, by measuring the strength of the returned signal, radar can estimate the mean diameter of a volume of drops. Radar reflectivity is normally expressed in logarithmic units, such that

$$Z = 10 \log_{10}(z) \tag{1.18}$$

where units are dBZ.

1.2.1 Weather Radar Systems

There are also many different types of radar systems including monostatic and bistatic, continuous wave and pulsed, Doppler, dual wavelength, and polarimetric. A discussion of most types is given in Rinehart (2004). For this project, the important radar system is the Doppler weather radar system known as the Weather Service Radar -1988 Doppler (WSR-88D). The WSR-88D network is maintained and operated by the National Weather Service (NWS).

Doppler radar uses the physical principles first described by Christian J. Doppler in 1853. Since the radar is stationary, any change in frequency of the transmitted signal must be due to the movement of its target. Doppler radar operates on the basic principle that if the target is moving towards the radar, its frequency will increase; if the target is moving away from the radar, its frequency with decrease. Therefore, Doppler radar

determines the speed of the target by the frequency shift between the transmitted signal and the return signal. As discussed in Section 1.2, weather radar measures a volume of hydrometeors. Therefore, the speed determined from the frequency shift is representative of a volume of rain drops or snow particles and can be thought of as a mean wind velocity. Also, since the return signal is a function of the diameter to the sixth power (Equation 1.16), the mean velocity is actually skewed towards the wind speeds of the larger particles. This study does not focus on the Doppler aspects of the WSR-88D so a derivation of the wind speed calculations will not be presented. See Chapter 6 of Rinehart (2004) for more information.

1.2.2 Radar-derived Products

Additional products besides the radar reflectivity factor can be derived from radar measurements. A few common products are vertically integrated liquid (VIL), rain rate, and total precipitation. The most important product for this study is VIL. VIL was first proposed and derived by Green and Clark (1972). VIL will be discussed in detail in this section as well as another product, called vertically integrated ice (VII). An understanding of how VIL and VII are obtained is important for this study since each of these products is used as a forecasting tool for lightning. Also of importance is the knowledge that these products, as all radar products, are based on remote sensing. Therefore, the products do not always accurately represent the environment. In most cases, these products only represent the storm environments well when assessed on large time scales greater than 5 minutes and spatial scales larger than 10 km. On smaller time and spatial scales the storm environment is very dynamic and cannot be accurately

represented by remote sensing snapshots (typically occurring every 5 to 10 min). With that in mind, a derivation of VIL and VII is provided.

1.2.2.1 Liquid Water Content and Vertically Integrated Liquid

An understanding of VIL starts with an understanding of liquid water content (LWC). LWC is defined by Wallace and Hobbs (2006) as the amount of liquid water per unit volume of air. The LWC of a cloud or storm system provides an estimation of the amount of liquid precipitation within it. A LWC measurement can be useful when attempting to locate heavy rain or hail within a storm. Determining LWC from radar measurements begins with an exponential drop-size distribution as proposed by Marshall and Palmer (1948),

$$N(D) = N_0 \exp(-\Lambda D) \tag{1.19}$$

where D is the drop diameter, $N(D)$ is the number of drops of diameter D, and Λ and N_0 are parameters of the distribution. The radar reflectivity factor, defined by Equation 1.16, can be also written

$$Z = \int_0^\infty N(D) D^6 dD. \tag{1.20}$$

Also, the liquid water content, M, can written in a similar form (derived in Doviak and Zrnic, 1993)

$$M = (\frac{\pi \rho_w}{6}) \int_0^\infty D^3 N(D) dD \tag{1.21}$$

where ρ_w is the density of water. Using the mathematical function

$$\int_0^\infty x^{\nu-1} e^{-\mu x} dx = (1/\mu^\nu)\Gamma(\nu) \tag{1.22}$$

where $\Gamma(\nu)$ represents the gamma function [$\Gamma(n)= (n-1)!$] and Equation 1.22 in Equations 1.20 and 1.21 yields

$$Z = \frac{720 N_0}{\Lambda^7} \tag{1.23}$$

and

$$M = \frac{N_0 \rho_w \pi}{\Lambda^4} \tag{1.24}$$

where Z has units $mm^6 m^{-3}$ and M has units $g\ m^{-6}\ mm^3$ (if ρ_w is in $g\ m^{-3}$). At this point in the derivation, two different paths could be taken. One could eliminate N_0 between each equation. The other is to eliminate Λ between each equation. The following derivation takes the latter option since both Green and Clark (1972) and Carey and Rutledge (2000) utilize this method. Eliminating Λ between the equations yields

$$M = \frac{N_o \rho_w \pi}{(720 N_0)^{4/7}} Z^{4/7} \tag{1.25}$$

where M and Z have units has defined above. Converting units of N_0 to m^{-4} yields the relation

$$M = \frac{N_o \rho_w \pi}{(720 \times 10^{18} N_0)^{4/7}} Z^{4/7} \tag{1.26}$$

where M is in $g \cdot m^{-3}$ and Z is in $mm^6 \cdot m^{-3}$. This relation is known as a *Z-M* relation. This relationship can also be determined empirically using the form

$$Z = aM^b \tag{1.27}$$

where both Z and M are determined from observations or measurements instead of theoretically with the Equation 1.25. Battan (1973) lists a number of empirically derived *Z-M* relations and demonstrates that Z is approximately proportional to M^2. This

information becomes a powerful tool in estimating the amount of liquid water in a specific cloud or storm. However, Z-M relations will be different for each cloud of each storm due to the difference in drop size distributions. Therefore, it becomes necessary to establish a standard relation so that results can be accurately studied and utilized.

Green and Clark (1972) standardized Equation (1.26) using assumed value of N_0 and ρ_w and applies the resulting equation to individual radar reflectivity measurements to estimate LWC, i.e, $N_0 = 8\times10^6\, m^{-4}$, and $\rho_w = 10^6\, g/m^3$ which yields

$$M = 3.44\times10^{-3} Z^{4/7}. \tag{1.28}$$

This value is then summed vertically, from reflectivity at the lowest level to the highest reflectivity at the highest level, resulting in VIL (or the amount of liquid water) for an individual atmospheric column. In equation form,

$$VIL = \int_{h_{base}}^{h_{top}} M\,dh = 3.44\times10^{-6} \int_{h_{base}}^{h_{top}} Z^{4/7}\,dh \tag{1.29}$$

where h is in meters and VIL has units of $kg\cdot m^{-2}$. As noted in Greene and Clark (1972), caution should be used when using this product. Equation 1.20 shows that the reflectivity, Z, is a function of the particle diameter to the sixth power. Therefore, the reflectivity will be dominated by large drops. A cloud with many small droplets may not be recognized by the radar, while a cloud with large drops will be recognized, even if the clouds have the same LWC. Also, since the radar assumes all drops are water, graupel, hail, and snow may give the impression of higher LWC than is actually present. Boudevillian and Andrieu (2003) assessed the accuracy of radar VIL measurements and concluded that the measurement errors are significant when related to meteorological conditions. According to their study, VIL is underestimated in convective situations

between 20% and 40% and the measurement error in stratiform situations ranged between +10% and -10%.

1.2.2.2 Vertically Integrated Ice

Vertically integrated ice (VII) is a term for the ice mass product used in this study. This and similar ice related products have gone by many names in the literature including ice cloud content (Sassen 1987), ice water content (Black 1990, Liu and Illingworth 2000; Peterson and Rutledge, 2001) and precipitation ice mass (Carey and Rutledge, 2000, Peterson et al. 2005, Gauthier et al. 2006, Deierling et al., 2008). In fact, the term vertically integrated ice has only been used recently (Motley 2006, McCaul 2008). In this study, the term is used because of its similar method of calculation to VIL. The calculation of VII for this study is equivalent to the calculation from Gauthier at al. (2006), where the product is called precipitation ice mass. Therefore, the VII values in this study are mathematically equivalent to the precipitation ice mass values in Gauthier at al. The Z-M relation used in this study to calculate VII was first proposed by Carey and Rutledge (2000) and is defined as

$$M = 1000\pi\rho_i N_0^{3/7}\left(\frac{5.28\times10^{-18}}{720}Z\right)^{4/7}(g\cdot m^{-3}) \tag{1.30}$$

where ρ_i is the density of ice (917 kg m^{-3}). VII is then calculated by

$$VII = 1000\pi\rho_i N_0^{3/7}\left(\frac{5.28\times10^{-18}}{720}\right)^{4/7}\int_{H_{-10}}^{H_{-40}} Z^{4/7}dH \tag{1.31}$$

where H_{-10} and H_{-40} indicate the heights of the -10 and -40°C environmental levels in meters, respectively. The region between -10 and -40°C is chosen because of its

relationship to charge separation in a storm. Climatologically these levels are located at 7 km and 11 km, respectively (Kalnay et al. 1996, Gauthier et al. 2006).

Equation 1.30 is used in numerous other studies (e.g. Peterson and Rutledge 2001, Peterson et al. 2005, Motley 2006, Gauthier et al. 2006) in addition to the Carey and Rutledge study. They developed this Z-M relation during the Maritime Continent Thunderstorm Experiment (MCTEX) because no appropriate relationship for deep, tropical convection existed. Therefore, the constants (ρ_i and N_0) Carey and Rutledge used could be significantly different from their values over Houston. Not only would these constants vary as a result of different locations but they will also vary throughout the life cycle of individual cells as a result of complex microphysical processes. Pruppacher and Klett (1997) observed that hail bulk particles densities range from 0.70 – $0.90 \times 10^6\, g\, m^{-3}$ and graupel densities range from $0.50 - 0.89 \times 10^6\, g\, m^{-3}$. Gilmore et al. (2004) observed the variability between hail and graupel intercept parameters with values ranging from 10^2 m^{-4} to 10^{10} m^{-4}. Motley (2006) performed VII sensitivity studies using these range of values for ρ_i and N_0. The results showed that the intercept parameter is the most likely source of error since the amount of variation needed for Z and ρ_i to produce the observed results seemed excessive. A combination of the three variables could be responsible, but without any in-situ measurements, it is impossible to know. Therefore, in this study, as well as in Peterson and Rutledge (2001), Motley (2006), and Gauthier et al. (2006), the values assumed by Carey and Rutledge (2000) for ρ_i and N_0 will be used. As a result, actual VII values should be used with caution as they could be unrepresentative of the actual environment. However, the relative trends in the values (e.g., low VII vs. high VII) will still be valid.

1.3 Previous Studies of Cloud Electrification with Radar

Studies of storm electrification via radar were performed shortly after weather radar was put into operation (Workman and Reynolds 1949). Their study concluded that significant storm electrification was concurrent with strong vertical development, which created an environment where precipitation ice, small ice crystals, and supercooled water droplets interacted near the -10 °C isotherm. Reynolds and Brook (1956) concluded that precipitation was necessary, but not sufficient, for significant cloud electrification. They observed precipitation echoes that did not produce lightning, but did not observe lightning without precipitation echoes. They also noted that rapid vertical development was needed for electrification and that the mean time lapse between the echo reaching the -10°C isotherm and a lightning discharge was 12 min. Shackford (1960) observed that lightning flash counts increased as the radar echo increased in height. Shackford also found that there is a relationship between lightning flash rate and reflectivity maxima above the 0°C level. He observed that the radar reflectivity vertical profiles exhibited a maximum at approximately 20,000 feet (-7 to -15 °C) for storms with high flash rates. He hypothesized that this was due to wet hail, and its presence was contributing to the charge generation and separation within the storm.

Larsen and Stansbury (1974) were the first to uses a specific dBZ value (43 dBZ) at a particular atmospheric level (7 km) as an indicator of lightning location. Their data show that there was no sferics (lightning signals determined by radio) from a storm if the 43 dBZ contour had not reached a height of 7 km (-30 °C). Following their work, Marshall and Radhakant (1978) used a similar procedure but lowered the height to 6 km and the reflectivity to 38 dBZ. “Larsen regions” were developed using these criteria and

Marshall and Radhakant concluded that "a weather-radar map of precipitation can be generated which can be read directly as a map of electrical activity."

Dye et al. (1986) observed an electrified storm in Montana. They found that the electric field within the cloud was less then 100 V m^{-1} until reflectivities of 35 dBZ were present. They also found that significant areas of a reflectivity near the -10 to -20 °C (approximately 7 km) level corresponded to areas of negative charge. Goodman et al. (1988) observed a microburst producing storm and found results that agreed with Dye et al. (1986). In both studies, the first lightning discharge was produced approximately 4-6 min after graupel particles were observed with radar. Dye et al. (1989) presented observations from a few storms in New Mexico. For one of the storms, precipitation detectable by radar was observed 25 min before even a weak enhancement of the electric field began and 30 min before the electric field began to rapidly intensify. The slow increase of the electric field was observed when 40 dBZ was observed at 6 km. In another storm, the electrification process moved much more quickly but lightning was not produced until 40 dBZ was observed at 6 km. Over all the cases they studied, the radar echo height needed to exceed 8 km for electrification to begin and needed to exceed 9.5 km for lightning production.

1.4 Previous Studies of Lightning Forecasting with Radar Reflectivity

All of the in-situ studies (Larsen and Stansbury 1974, Marshall and Radhakant 1978, Dye et al. 1986, Goodman et al. 1988, Dye et al. 1989) discussed previously used radar data to infer the presence of mixed phase particles, especially graupel, at different environmental heights and isotherms (0, -10, and -20 °C). The location of radar-inferred

graupel signaled the onset of cloud electrification. As a result, studies began to investigate the usefulness of using radar reflectivity to forecast lightning in storm cells.

Buechler and Goodman (1990) suggested a new algorithm for the WSR-88D to identify lightning producing storms as storms with 40 dBZ reflectivity observed above the -10°C level and an echo top at or above 9 km. In the 20 storms from Florida, Alabama, and New Mexico that they used for their study, their radar criteria had a probability of detection (POD) of 100% 4-33 min before the first flash occurs, a 7% false alarm rate (FAR) and a critical success index (CSI) of 93% (Section 2.9 contains a complete description of these statistical parameters). When only radar reflectivity of 40 dBZ at -10°C was considered, the POD was still 100% but the FAR increased to 20% and the CSI decreased to 80%. Michimoto (1991) used 30 dBZ reflectivity at the height of the -20°C isotherm and found that the first CG strike occurred 5 min after a storm met this criteria. Michimoto also observed that if a storm did not reach those criteria, it did not produce lightning.

Hondl and Eilts (1994) found that reflectivity of 10dBZ near the 0 °C level could be a definitive characteristic of a future thunderstorm. For a storm initialized along a gust front created by a dissipating complex of thunderstorms in a conditionally unstable environment, using 10 dBZ at the 0 °C isotherm level yielded a lead time of approximately 16 min. Using the same criterion on a storm initialized along a sea breeze boundary yield a lead time of only 8 min. Another sea breeze initiated cell they observed had reflectivities as high as 54 dBZ, but did not produce a CG flash. For the 23 cells they analyzed, using the 10 dBZ at the 0 °C yielded an average lead time of 15 min. However,

there were 5 cases where no lightning was produced. This results in a FAR of 18% and a CSI of 82 %.

Gremillion and Orville (1999) studied lightning initiation signatures (LISTs) of 37 thunderstorms near Kennedy Space Center to determine whether lightning could be reliably forecast by radar reflectivity. A LIST was defined as a value of maximum reflectivity that exists for at least two volume scans at a given isotherm level. The LIST criteria used were 35, 40, and 45 dBZ at the -10°C level; 25, 30, and 35 dBZ at the -15°C level; and 20, 25, and 30 dBZ at the -20°C level. Their statistical results are shown in Table 1.3. The table shows that the best LIST, statistically, was 40 dBZ at -10°C. Their study also showed that the best LIST in terms of lead time was 25 dBZ at the -15°C level.

Vincent et al. (2003) performed a similar study over central North Carolina for 50 thunderstorms. The criteria they used were 30 or 40 dBZ at the -10 or -15°C level for one or two volume scans yielding eight possible combinations. Their results are shown in Figure 1.7. The best criterion in their study was 40 dBZ at -10 °C for one volume scan. Their study also showed that requiring the criteria to be met for more than one volume scan actually reduces the forecast quality.

Wolf (2006) performed the most robust study to date. The study included more than 1,100 convective cells over 20 days in northern Florida and Georgia. Wolf used a similar criterion as the previous studies (40 dBZ at -10 °C level), but used the -10 °C level within the updraft instead of the ambient environment. 297 of the cells studied produced no lightning. Using this new criterion, Wolf found the results shown in Table 1.5. Those results show a significant increase in the probability of a CG strike when the 40 dBZ echo moved to within 1 km of the updraft -10 °C level. The environmental -10

°C level was usually 2,000 to 4,000 ft below the updraft -10 °C level, and, as such, had significantly less probability of producing a CG flash. Wolf also tried to forecast storms that will produce a high number of CG flashes based on the height of the echo above the -10 °C updraft level. These results are also shown in Table 1.6. The POD using 8 kft above the -10 °C updraft was 0.96 but FAR was 33% while using 4 kft above the -10 °C updraft level produced a POD of 1, but a FAR of 47%. One drawback is that the study does not mention the season during which the analysis takes place, nor does it provide an example case to clarify the methodology.

Most recently, Clements and Orville (2008) compared the warning times of CG flashes from radar and total (i.e., CG and intracloud) lightning observations. This study is also the only lightning forecasting study done over Houston, Texas. Other lightning studies over Houston have shown an enhancement in the amount of cloud-to-ground lightning in and surrounding the city (Orville et al. 2001). It was originally thought that the real-time detection of IC lightning could be used as a forecast tool for a CG strike since it normally occurs first (Goodman et al. 1988, Motley 2006). However, Clements and Orville (2008) showed otherwise. Using the criterion of 30 dBZ at the -10 °C level produced an average lead time of 16 min compared to an average of 3 min using the total lightning method. Detection errors within the total lightning network may have caused this result, but mores robust studies need to be preformed. As a result, they concluded that using total lightning detection alone in attempts to forecast CG flashes is ineffective.

1.5 Previous Studies of Lightning Forecasting with Other Radar-derived Products

VIL has also proven effective in assisting forecasts of lightning and severe weather. Greene and Clark (1972) hypothesized that the large radar returns due to hail and the associated VIL values could aid in hail prediction and the Houston Weather Forecast Office (WFO) of the NWS commonly uses VIL as an indicator of a storm's severity (Lance Wood, personal communication). A WFO will commonly set a VIL value they think corresponds to hail and set alarms to notify forecasters if that value is reached. Using VIL to predict hail size was determined by Edwards and Thompson (1998) to be ineffective but other products based on VIL, including VIL density (Amburn and Wolf 1997), are currently being developed and tested for hail size prediction.

VIL has also been correlated to CG flashes. Watson et al. (1995) observed the distribution of VIL and lightning for a storm on 9 June 1993. They found that many of the flashes within this particular storm were associated with a VIL between 1 – 15 kg m^{-2}, shown in Figure 1.8. However, as shown in Figure 1.9, higher VIL values were more likely to be associated with lightning. For example, a VIL between 40 kg m^{-2} and 45 kg m^{-2} produced lightning 65% of the time for this storm.

Relationships between VIL and lightning flash density have also been studied. MacGorman et al. (2007) compared the lightning flash rate and VIL values for 1200 cells. Their results show a lack of a clear relationship between VIL and maximum ground flash rates, but that the mean and mode values do increase with increasing flash rate. Yeung et al. (2007) used VIL in their lightning initiation and intensity nowcasting technique. VIL alone cannot be used to forecast lightning, as shown by the lightning distributions in Watson et al. (1995) and MacGorman et al. (2007). However, a using VIL in addition to

other parameters shows promise (Yeung et al. 2007), as does the development of other products based on VIL (i.e., VIL density, Amburn and Wolf 1997).

1.6 Thesis Objectives and Hypothesis

The objectives of this study are to i) extend the previous work done on lightning forecasting with weather radar to the area observed by the WSR-88D operated by the NWS at the Houston/Galveston (HGX) WFO using an extensive, multi-year radar and lightning dataset, ii) integrate an additional radar-derived product, VII, into the lightning forecasting process, and iii) determine the best lightning predictors for the study area in terms of statistics, by analyzing a forecast contingency table, and warning time, by maximizing POD, CSI, and warning time and minimizing FAR, for different synoptic settings.

Forecasts of cloud-to-ground (CG) lightning will be created based on various radar reflectivity levels at different environmental heights. Forecasts of CG lightning will also be created using cell-based values of the vertically integrated ice product. Based on these forecasts and the observed CG lightning from the National Lightning Detection Network (NLDN), the best predictors will be determined. Variations in the year and month will be considered, since the type of synoptic or mesoscale forcing of a particular storm can vary on these temporal scales, and may affect the predictors. Variations in the length a cell was tracked by the radar, as well as the cell's distance from the radar, are also considered. The length a cell was tracked is considered since using a radar-based cell tracking method allows for the detection of small, weak storms as well as strong,

long-lived storms. The distance from the radar is considered since the horizontal and vertical resolution of radar data degrades as the distance from the radar increases.

In contrast to previous studies, the work done within this study objectively analyzes a large number of cells in an attempt to provide high confidence statistics. Only one of the previous studies (Wolf 2006) analyzed more than 100 cells. This will be done with an automated method that allows for the analysis of many cells without the need of visual confirmation. A total of 85,604 radar volume scans are analyzed which produces a total of 475,593 identified cells.

Based on prior research, we hypothesize that the analysis of a large number of lightning producing storm cells will result in significant increases in the confidence of lightning forecasts as well as increase situational awareness for forecasters at WFO HGX.

2. DATA AND METHODOLOGY

2.1 Radar Data

Ten years (1997 – 2006) of archived (Level II) Houston (KHGX) radar data obtained from the National Climatic Data Center (NCDC) for daylight hours (14 – 00 UTC, 09 CDT – 19 CDT) for the summer months (June, July and August) was analyzed. These archived data files contained all the measurements (radar reflectivity, velocity, and spectrum width) from the entire volume scan started at the time listed on the file.

2.1.1 Weather Surveillance Radar – 1988 Doppler (WSR – 88D)

The KHGX WSR-88D is part of the Next Generation Radar (NEXRAD) network. This radar network consists of 155 radars within the contiguous United States, of which, the NWS operates 121 (OFCM 2008). The WSR-88D radar specifications are listed in Table 2.1. The WSR-88D system directly measures radar reflectivity, which is calculated from the strength of the return signal (as discussed in Section 1.1), and radial velocity, which is calculated from the signal frequency shift (as discussed in Section 1.2). Another base product, called the spectral width is calculated from the variability of the radial velocity data. These three products are then used to produce many other forecast products. For this study only radar reflectivity will be utilized.

Of great significance to this study is the fact that the radar does not scan only one level. Many radar systems, including the WSR-88D, have the ability to scan the environment at different elevation angles. An elevation angle is the angle between the horizontal plane, usually the base or platform on which the radar is located, and the line-

of-sight of the antenna. As the beam travels away from the radar it increases in height as shown in Figure 2.1. This is due to many factors including the curvature of the earth, the refractivity of the atmosphere, and the elevation angle of the radar beam. The height of the radar beam can be calculated, assuming standard refraction, by the equation

$$H = \sqrt{r^2 + R'^2 + 2rR'\sin\phi} - R' + H_0 \qquad (2.1)$$

where r is the range to the target, R` is 4/3 R (where R is earth's radius), H_0 is the height of the radar antenna above sea level, and ϕ is the elevation angle of the radar beam (Rinehart 2004). As a result of this increase in beam height, the elevation angles used to detect a storm are important. If a scan strategy utilizes mainly low elevation scans, the beam has more potential to miss the upper-levels of a storm. On the other hand, if a scan strategy utilizes mainly high elevation scans, the beam has the potential to miss important low-level features or overshoot the top of a storm. Figure 2.2 shows a graphical representation of how a scan strategy samples a storm.

The NWS uses various Volume Control Patterns (VCPs) to control the elevation angles used on the WSR-88D. There are a total of nine VCPs (OFCM 2008, Table 2.2). The VCP is controlled by the WFO in charge of the radar and can be changed if a forecaster feels it is necessary. Two precipitation mode VCPs are shown in Figures 2.3 and 2.4. VCP 11 (Fig. 2.3) consists of 14 elevation scans (0.5°, 1.5°, 2.4°, 3.4°, 4.3°, 5.3°, 6.2°, 7.5°, 8.7°, 10.0°, 12.0°, 14.0°, 16.7°, and 19.5°) and 16 azimuthal scans in 5 minutes. The best vertical sampling is provided by VCP 11, which is typically used for severe weather within 60 nautical miles of the radar (Gauthier et al. 2006; OFCM 2008). VCP 12 has the same number of elevation angles as VCP 11, but concentrates more angles at lower levels. VCP 21 (Fig. 2.4) consists of 9 elevation scans (0.5°, 1.5°, 2.4°,

3.4°, 4.3°, 6.0°, 9.9°, 14.6°, and 19.5°) and 11 azimuthal scans in 6 minutes and provides less vertical sampling than VCP 11 and 12.

Previous studies (Brown et al. 2000a and 2000b, Gauthier et al. 2006, Motley 2006) considered the VCP in their analysis. For example, Gauthier et al. (2006) excluded all non-VCP 11 data from their study. This study does not exclude any data based on the VCP used even though the other VCPs may result in poorer vertical sampling. However, since the events important to this study occur mainly as a result of convection, it is assumed that the VCP being used during the events provides sufficient vertical sampling. For example, during a day when there is no thunderstorm activity or none is expected, the radar may be run in "clear air" mode (VCP 31/32). Since there will be no lightning events during that day, the statistics provided in this study will not be effected by the poor vertical sampling of these VCPs. WFO HGX runs VCP 11 in most situations, but will run VCPs 211, 12, and 212 in some circumstances (Lance Wood, personal communication). VCP 211 and 212 use the same elevation angles as VCP 11 and 12, respectively, but improve the velocity data using an algorithm to reduce range ambiguity.

2.1.2 Constant Altitude Plan Projection Indicator (CAPPI) Data

Weather radar data can be viewed in multiple ways. The most common way is known as a plan position indicator (PPI) display. A PPI is a constant elevation display that normally places the radar location at the center of the map and the corresponding radar echoes on the map at their location relative to the radar. Topography, roads, coastlines, and many other objects can be overlaid on the PPI for increased understanding of the location of the radar echo.

It is also possible to display only the data from a specific altitude. This radar data format, known as a constant altitude plan projection indicator (CAPPI), uses an algorithm to calculate the height of radar echo from its original polar coordinates. The data used in this study is based on the CAPPI format.

As discussed in Section 2.1.1, the slight angle of the radar beam causes the beam to rise as it moves away from the radar. Therefore, when looking at a normal PPI display, the echo shown is at different altitudes. However, when looking at a CAPPI display, all the data displayed is at the same altitude. A CAPPI display requires the entire radar volume scan to be completed since multiple PPI scan are used to calculate the reflectivity at each height. A problem will arise on a CAPPI plot whenever the storm is not adequately sampled since, as a radar varies in elevation, gaps occur in the data. Therefore, to create a CAPPI plot, interpolation must be used to fill the possible gaps. This does not affect the data at lower elevations and close to the radar, but as the height or distance from the radar is increased the data can become a product of interpolation instead of actual measurements. Therefore, this study will analyze the results at varying distances from the radar and using different vertical resolutions to consider this effect.

2.1.3 Cartesian CAPPI Data

The KHGX radar data was converted from it native Level II format to Universal Format (UF)(Barnes 1980). The UF data was then interpolated onto a 150 x 150 x 20 Cartesian grid (or 300 x 300 x 20 km) using the National Center for Atmospheric Research REORDER software package (Mohr et al. 1986, Oye and Case 1995). REORDER takes a requested horizontal (x, y) resolution and vertical (z) resolution when

applying its interpolation scheme. A three-dimensional Cressman interpolation scheme was used. This scheme uses two parameters: the radius of influence, R, and the distance between the radar gate and the Cartesian grid point, r^2. The weight for a particular value is represented by

$$W = \frac{R^2 - r^2}{R^2 + r^2} \tag{2.2}$$

where R^2 is calculated using

$$R^2 = dX^2 + dY^2 + dZ^2 \tag{2.3}$$

where dX, dY, and dZ are the values set for the radius of influence of each spatial dimension. The interpolation is weighted so that the points located closer to a particular gate have more influence than those points further away. For this study the x, y, and z radii of influence were set 1.25, 1.25, and 1.75 km, respectively.

2.1.3.1 Vertical Resolution of CAPPI Data

A horizontal resolution of 2 km was found to be adequate for the radar data based on previous studies (Gauthier et al., 2006) and is a commonly used value in other radar studies based on objective statistical methods. However, an adequate vertical resolution was not as clear. Gauthier et al. (2006) found 1 km vertical resolution to be adequate for their study, but this study includes forecast statistics based on the reflectivity at given height while theirs did not. Thus, the vertical resolution of the radar data must be small enough to utilize available data but not introduce spurious features. If the vertical resolution is too large, little differentiation will occur between the height levels in the forecast statistics.

This problem was addressed by comparing data interpolated at a 1 km vertical resolution to data interpolated at a 0.5 km vertical resolution. The horizontal resolution was kept at 2 km for each of the data sets. August 2006 was chosen as the time period for the data comparison since the month exhibited the general storm characteristics expected during the summer months in Houston where precipitation was 0.43" below normal with a monthly total of 3.40" but 10 days reported precipitation totals greater than 0.01" and 6 of those days had precipitation totals greater than 0.30".

The contingency table statistics and forecast lead times of each of the different datasets are compared to determine if a 1.0 km vertical resolution is sufficient for reflectivity-based lightning forecasting. The desire to keep the data at a 1.0 km vertical resolution is motivated by Gauthier at al. (2006), where the vertical resolution is 1.0 km. Comparison between this study and their study is important and therefore consistency in the datasets was desired. Results of the analysis show that the 1.0 km resolution provided better results than the 0.5 km resolution. As a result, the radar data is interpolated to a vertical resolution of 1.0 km. A detailed analysis and comparison of the two datasets as well as relevant figures and tables is given in Appendix A.

2.2 National Lightning Detection Network (NLDN)

The CG lightning data used in this study was provided by the NLDN, which is owned by Vaisala, Inc. This network uses a combination of a magnetic direction finding (MDF) system and a time of arrival (TOA) system.

The MDF system was first developed by Krider et al. (1976) and was the first type of lightning system used in the United States (Orville, 2008). The MDF system

consists of two vertical and orthogonal loops. One of the loops is oriented north-south and the other is oriented east-west. The loops are oriented vertically since it is assumed that the lightning strike is vertical and will therefore produce an electric field that is oriented vertically. If the electric field is oriented vertically then, by Maxwell's equations, the magnetic field must be oriented horizontally. These loops then measure that magnetic field, and based on the amount of signal received by each loop, determine a direction. A minimum of two MDFs are needed for lightning location. This technique is shown in Figure 2.5.

The TOA system is based on measuring the time when the electromagnetic field signal reaches a detector. Using this time and the difference in time and distance the same signal arrived at a different sensor, all the possible locations of the strike may be placed on a hyperbola. If the same signal is measured at one more location, the position of the strike may be determined as the location where the two hyperbolas intersect. This is shown in Figure 2.6. For unambiguous CG location, a minimum of four TOA sensors is needed.

The MDF and TOA sensors were combined in 1994 to create the Improved Accuracy from Combined Technology (IMPACT) sensor. The MDF sensor is used to establish the bearing and the TOA sensor is used to establish the distance. The use of both the MDF and TOA data, combined with a least squares technique, provides a higher accuracy than either system alone (MacGorman and Rust 1998, Cummins et al 1998). The median location accuracy was increased to within 500 m and detection efficiency ranges from 80% to 90% for flashes with peak currents above 5 kA, with the majority of the US within 90% detection efficiency (Cummins et al., 1998).

An additional upgrade occurred in 2002-3 with the installation of an improved IMPACT sensor, IMPACT-ESP, and the addition of 8 new sensors (Cummins et al. 2006). This upgrade improved flash detection efficiency to 90-95% over the US. Biagi et al. (2007) participated in a field campaign which measured the performance of the NLDN over Arizona, Texas, and Oklahoma for 2003 and 2004. The results from 2003 and 2004 had an average flash detection efficiency of 92% and 86%, respectively. Biagi et al. also recommended that any positive flashes with peak current less than 15 kA be excluded. In their study, positive flashes with a peak current less than or equal to 10 kA were from ground flashes only 1.4% (6/420) of the time. Positive flashes with peak current between 10 kA and 15 kA were ground flashes only 3.7% (3/81) of the time. Thus, any flashes with positive peak current less than 15 kA were excluded from this study.

These sensors measure each individual stroke of a lightning flash. Therefore, the data was post processed by Vaisala Inc such that the individual strokes were combined into flashes for use in this study. This flash data was compared and correlated to individual storm cells for analysis. The correlation process is discussed in Section 2.5.

2.3 Sounding Data and Methodology

Sounding data was obtained from the NOAA/ESRL Radiosonde Database for the same time period as the radar data. Houston (HGX) does not launch a radiosonde, so data was averaged between Lake Charles (LCH), Corpus Christi (CRP), and Fort Worth (FWD) to create a HGX sounding. For the period of this study there were 1867 LCH soundings, 1873 CRP soundings, and 1860 FWD soundings. The HGX sounding was

created by using a weighted average. This has been done in previous studies (Vincent et al. 2003, Clements and Orville 2008) and was the suggestion of the Houston WFO (Lance Wood, personal communication). LCH, CRP, and FWD are located 194 km, 302 km, and 404 km away from HGX, respectively. Therefore, the average was weighted most heavily toward LCH, then CRP, and last FWD. If a sounding wasn't available for that day, the remaining two were weighted with respect to distance. If only one sounding was available, that sounding alone was used to create the HGX sounding. If no soundings were available for a given time or day, the next closest time or day with at least one sounding was chosen.

Including the FWD sounding was debated since it can be much drier than either LCH or CRP. However, the lack of baroclinic forcings creates a similar environment over much of the Southeast United States. Thus, it was decided to include the FWD sounding, but weight it half as much as CRP and a third as much of LCH. Using this averaging method in the winter, however, would not yield the desired results, especially if FWD is included. During the winter, cold fronts frequently create large temperature gradients across the Southeast and FWD will commonly have a very different atmospheric profile than the coastal sites.

Only the 00 UTC and 12 UTC soundings were used. Any special soundings at 06 UTC and 18 UTC were not included in the averaging. This resulted in a total of 1840 HGX soundings, or two for each day analyzed during this study. From of these soundings, the environmental temperature levels (-10, -15, -20, and -40 °C) and updraft temperature levels (-10 °C) were determined.

2.4 Cell Identification and Tracking with Radar

Since the lightning forecasts are on a cell-by-cell basis, the ability to identify, track, and forecast convective cell movement is vital. Weather radar is a valuable tool that can be used for this purpose. This study uses a modified version of the Storm Cell Identification and Tracking (SCIT, Johnson et al. 1998) algorithm. The original SCIT algorithm was designed to work only in polar format since that is the format native to radar data. However, as discussed above, the radar data used in this study was in Cartesian CAPPI form. Another cell tracking method, Thunderstorm Identification, Tracking, Analysis, and Nowcasting (TITAN, Dixon and Wiener 1993) works on Cartesian data, but uses a different tracking method than SCIT. Overall, SCIT provides better tracking of smaller cells within larger convective systems, which was desired by this study. The operational use of the SCIT algorithm within the NWS also motivated its use in this study. The SCIT algorithm contains four steps, shown in Figure 2.7: storm cell segments, storm centroids, storm tracking, and storm position forecast. In the variation of the SCIT algorithm used in this study, CAPPI-SCIT, there are a few differences. Those differences and the process involved in each step will be discussed below. All of the information regarding the SCIT algorithm came from either Johnson et al. (1998) or OFCM (2006).

2.4.1 Storm Cell Segments

Both the SCIT and CAPPI-SCIT algorithms begin by identifying one-dimensional (1D) segments within the reflectivity data. For the SCIT algorithm this happens along each radial, but for the CAPPI-SCIT algorithm this happens along the x-axis. The

CAPPI-SCIT algorithm begins in the lower left corner of the grid, at point (0,0), then moves across all the x values. When that is completed, it moves to the next y value and repeats the movement across all x values. This is continued until all the data at that level (i.e. 1.0km) has been put into segments. It then moves to the next height and repeats the process. This is continued until the analysis has been performed at every level.

Both algorithms use seven reflectivity thresholds (30, 35, 40, 45, 50, 55, and 60 dBZ) to group the data into segments. A segment consists of all the data within a certain reflectivity threshold along the search path. An example is shown in Figure 2.8. When a reflectivity value is found that is above the specified reflectivity threshold it is grouped with all the subsequent points with reflectivity values greater than the specified threshold. The CAPPI-SCIT algorithm uses the same technique as the SCIT algorithm when attempting to determine the end of a segment. If a reflectivity value is found that is less than the specified threshold, but the difference between the reflectivity at that point and the reflectivity threshold is less than a user-defined variable, the point is retained in the segment and a counter is incremented. This counter contains the amount of times a point has been retained based on the difference between its reflectivity and the specified reflectivity threshold. If the counter reaches a user-defined amount, the point is not included in the segment.

A 1D segment must have a user-defined length to be retained. The default for SCIT is 1.9 km (Johnson et al. 1998), but CAPPI-SCIT uses 4.0 km. This is equivalent to 2 consecutive points on the 2 km x 2 km (x, y) Cartesian grid. This process is then repeated for all reflectivity thresholds so that the data is divided into segments based on all the thresholds.

2.4.2 Storm Cell Centroids

The next step of both algorithms is combining the individual storm segments into two-dimensional (2D) components. It is during this step that the SCIT and CAPPI-SCIT algorithms differ the most.

The SCIT algorithm combines segments that are azimuthally adjacent and radially overlapping. User-defined azimuthal and overlap variables are used during this combination process and only segments defined by the same reflectivity thresholds are used. If a component based on a higher reflectivity threshold is found within an area of lower reflectivity, the component with the high reflectivity is retained while the other is discarded. This yields, at every level, the mass-weighted centroid of each 2D cell.

The CAPPI-SCIT algorithm also combines the segments into 2D components, but the method is different. The segment data is placed into an array. This array is the same size as the CAPPI grid (150 x 150 x 20) with an additional dimension that has the same number of elements as reflectivity threshold categories. This array contains the locations of all the reflectivity threshold segments. To create the 2D components, a contour function is run on the array for each of the reflectivity thresholds. This contour function returns the boundaries of the contours and these boundaries define each of the 2D components for each reflectivity threshold. As in the SCIT algorithm, if a component boundary of higher reflectivity is found within a component boundary of lower reflectivity, the component of lower reflectivity is ignored. However, there are no separation or overlap criteria as in the SCIT algorithm. Also, as in the SCIT algorithm, an area criterion is used to eliminate very small cells.

The next stage of this portion of the algorithms is vertical association of the 2D components to create three-dimensional (3D) storm cells. The differences between the two algorithms are still significant.

During this stage, the SCIT algorithm uses an iterative search process to associate the components. The process begins by searching within a 5 km radius (total area of 78.5 km^2) of the component centroid at each elevation angle. If a component is found, it is associated with the component at the lower level and a cell is created. If multiple components are found within range, the component with the largest mass, estimated by the liquid water content, is associated. If there are still unassociated components after 5 km search, the process is repeated at 7.5 km (total area of 177 km^2) and then at 10 km (total area of 314 km^2). Since only the highest reflectivity thresholds are used in the component creation, the association stage yields a 3D storm cell centroid.

When there are multiple cells identified within a close proximity, the SCIT algorithm attempts to merge them. Cell are only merged when: 1) the cells do not have components on the same elevation angle (i.e., there is a vertical gap in one or both of the cells), 2) the distance between the cells is less than a user-defined default, and 3) if the separation between the base of one cell and the top of the other is less than 4.0 km and an elevation angle of 3.0°. If cells in close proximity still remain, the weaker cell, determined by its LWC, will be deleted. If the distance between the centroids is less than a user-defined value and the difference in depth is less than a user-defined value, the weaker cell will be discarded.

The vertical association of 2D components is done differently in the CAPPI-SCIT algorithm. The 2D components are defined, as in the SCIT algorithm, with the highest

reflectivity threshold for that particular component. Only one vertical association range, 6 km, is used in the attempt to associate cells. This range is also not calculated from the individual component centroids, but from the boundaries of the components. If the search from the component boundary point yields another point in a component within 6 km at the next height, that component boundary point is kept. For example, if a component boundary point is located at (10, 10) on the horizontal grid at the lowest level, the next level is searched from (7, 7) to (13, 13) for a component boundary. If a component boundary is found within that search area, then the point (10, 10) is retained as a cell boundary. This method yields a total search area of 144 km^2, which is less than the SCIT methods. However, this method did not only search from the centroid, but from every point along the boundary of a cell.

After the vertical correlation is performed, cell attributes are calculated. The CAPPI-SCIT algorithm calculates the cell centroid, the cell depth, the maximum reflectivity at each level, the major and minor axis of an ellipse fit to the cell, the cell area, and a cell-based VIL and VII. The cell-based VIL and VII are calculated by integrating the maximum reflectivity values at each height. This is to account for possible tilted cells. An example of the difference between a cell-based calculation and a grid-based calculation is given in Figure 2.9. The output of this portion of the algorithm is used as input in both the storm cell tracking and the storm cell position forecast steps.

2.4.3 Storm Cell Tracking

The methodology between the tracking for the SCIT algorithm is only slightly different than that of the CAPPI-SCIT algorithm. For both algorithms, the first step is to

determine the time difference between the volume scans. If the difference is greater than a user-defined value (default = 10 min), time association is not utilized; all the cells are treated as if it was the first time they have been identified. This step is motivated by the unpredictable nature of the data. If there is a loss of communications or the radar has a problem, this results in a gap in the dataset. Even though two files may arrive in succession, they could be hours apart. Attempting to track cells on these files would be useless.

The next step is also the same in both algorithms. A first guess, based on the cell's previous centroid and movement, is generated. The cell's movement is determined by its average movement in the previous scans or a default motion vector if the cell was first detected on the previous volume scan. This default motion vector can be used-defined or based on the average motion vector of all the other detected cells.

After a first guess is generated for all of the cells, correlation between the first guesses and the current centroids is attempted. The distance between all current centroids and first guesses is calculated. For the both algorithms, if the difference between the current centroid and a first guess is within a certain threshold the cells are correlated. If more than one correlation is possible, the possibility with the smaller difference is considered to be best. This is the only correlation done by the SCIT algorithm, but the CAPPI-SCIT algorithm adds an additional step. The 30 dBZ boundary of cell on the previous volume scan is used as a search area for cells on the current scan. If a cell on the current scan is found within the 30 dBZ boundary of a cell on the previous scan, those cells are correlated in favor of a distance correlation. This is motivated by the fact that the cell centroids can be located in larger areas of reflectivity and will not move outside

of that area. This becomes useful if an intense cell develops within a large area of lighter reflectivity. If more than one cell is found within the 30dBZ boundary of a previous scan's cell, the distance correlation method is used for the corrected correlation. Cells that develop quickly and are not imbedded in large areas of reflectivity show little difference between SCIT and CAPPI-SCIT tracking since CAPPI-SCIT uses the SCIT method of correlation first. The boundary method is used as an additional tool for correct cell correlation.

2.4.4 Storm Cell Position Forecast

The storm cell position forecast is not used in this study, but has the potential to aid lightning forecasting on a cell-by-cell basis since it can be used to warn specific areas in the path of a lightning producing storm. The method is identical between the two algorithms. A new motion vector is created for each of the identified cells. If the cell has been tracked for at least two scans, this vector is calculated using a linear least squares fit based on the storm's current position as well as up to 10 previous locations. If the cell is new, its motion vector is calculated by averaging the motion of all the other cells, or, if no other cells are available, a user-defined default is used. Forecasts for the cell are made at various time steps (0, 15, 30, 45, or 60 min). The number of forecasts made is based on the error of previous forecasts. If a previous forecast's error is larger than a user-defined permissible range, that forecast time step is omitted in the current forecast. Basically, if the previous forecast for the cell was poor, the current forecast is made for a fewer number of time steps to reduce possible forecast errors.

During this step, a cell table, with all of the attributes of each cell, is created. This table contains the cell's attributes for up to 10 previous scans. The time series stored in the table provide a valuable tool in identifying the growth and decay of a cell.

2.5 Lightning Correlation

CG lightning strikes were correlated with the cells identified by the CAPPI-SCIT algorithm. This process started with identifying all the lightning strikes that occurred within 150 km of the KHGX radar between two minutes before the scan started to two minutes after the scan started. This time frame is chosen since most of the precipitation mode VCPs take approximately five minutes to complete. Therefore, it is the total amount of CG lightning that occurred within a five minute period within the KHGX domain. As discussed previously, the CG lightning data was provided by the NLDN and contained the latitude, longitude, date, multiplicity, and peak current of each CG strike.

Correlation of the strikes was first attempted within the 30 dBZ boundaries of the CAPPI-SCIT identified cells. If a strike was within the 30 dBZ boundary, it was correlated with that cell. Otherwise, the distance between the boundaries of the highest reflectivity threshold of each cell and the lightning strike was correlated. The strike was then correlated to the cell with the shortest distance. In this way, every CG strike is correlated to a cell, even if the correlation distance was large.

2.6 CG Lightning Forecasts

Numerous CG lightning forecast criteria were used in an attempt to establish the best criteria for Houston. Two different radar parameters were used, reflectivity and VII,

as well as three different environmental levels (-10, -15, and -20 °C) and one updraft level (-10 °C). The environmental levels are defined as the height for which a temperature is observed in the atmosphere. This data comes directly from a radiosonde. The average height of the -10, -15 and -20 °C isotherms for this dataset was 6494, 7381, and 8092 m, respectively. The updraft temperature level is calculated by using the sounding to calculate the temperature a parcel would be in a thunderstorm updraft. An example, plotted on a Skew-T/Log P diagram is shown in Figure 2.10**.** The environmental temperature levels were the same as in previous studies (Gremillion and Orville 1999, Vincent et al. 2003, Clements and Orville 2008) and the updraft level was used for comparison with Wolf (2006). The reflectivity values used are also from the same previous studies.

Forecasts were also made based on cell-based VII values. If the cell-based VII reached a certain values, then a forecast was made. The test values were determined by calculating the distribution of VII values throughout the entire dataset and using the resulting percentiles. Percentile values every 5% were used as forecast criteria (i.e., 5, 10, 15, 20, 25, …).

Lightning forecasts were made on a cell-by-cell basis. A forecast was a yes-no product on whether or not the cell was expected to produce CG lightning. A typical forecast was used using the following steps: 1) CAPPI-SCIT was run on a radar volume to identify and track cells, 2) environmental temperature levels were obtained from an area-averaged sounding, 3) for each cell, the reflectivity values were obtained at the environmental and updraft levels, 4) if the reflectivity values met the given thresholds, a

"yes" forecast was made, 5) cell-based VII was calculated and if the values met the given percentile, a "yes" forecast was made.

2.7 First Flash Forecasts and Lead Times

In additional to making a CG forecast, a first flash forecast was made with the same methodology as a normal CG forecast. A forecast was considered a first flash forecast if: 1) the cell had not produced any lightning during the time it has been tracked or, 2) the cell had not produced any lightning in ten minutes.

Since the lightning forecast is be based on radar data, the actual time the forecast is made needs to be considered. The time on the radar data files is the time the volume scan started. Gremillion and Orville (1999) and Clements and Orville (2008) used the difference between the time on the file and the time of the first CG strike to calculate the lead time. Vincent et al. (2003) found that using the time when the volume scan started produced an error in the lead time from 2.5 to 4.5 min since a typical WSR-88D volume scan lasts 4-6 min (Table 2.2). Therefore, they subtracted 3.50 minutes to account for this error. To maintain consistency with the previous study over Houston (Clements and Orville 2008), the lead time in this study will be the difference between the time when the scan began and when the strike occurred.

2.8 Automated Analysis Process

All of the data and methodologies discussed previously were combined into an automated process to calculate forecast statistics and lead times. This process proceeded as follows:

Step 1): Interpolate KHGX Level II radar data into CAPPI format with the dimensions 150 X 150 X 20 (x, y, z).

Step 2): Run CAPPI-SCIT algorithm on CAPPI radar data.

Step 3): Create the KHGX sounding

Step 4): Using the cell data from Step 2 and the sounding information from Step 3, create lightning forecasts based on various reflectivity values at various environmental and updraft temperature levels. Also make forecasts using cell-based VII values.

Step 5): Find the lightning data within five minutes from when the scan began and correlate to cells.

Step 6): Compare forecasts with lightning correlations to determine POD, FAR, CSI, and lead time values.

This automated process was performed on a total of 85, 603 radar volume scans, which resulted in 475,593 identified cells, 65,399 unique cells, and 1,028,510 correlated CG flashes.

2.9 Statistical Methods

The forecast statistics for this study used a simple 2 x 2 contingency table, shown in Table 2.3, to determine the forecast skill of each predictor. X represents the number of events for which a forecast was made and the event was observed (also called a hit). Y represents the number of events that were observed but no forecast was made (also called a miss). Z represents the number of events in which there was a forecast but the event was not observed (also called a false alarm). W represents the number of events for

which there was no forecast and the event was not observed. From the data in the table, three variables were used in computing the skill of the forecasts. The first was the probability of detection (POD), the second was the false alarm ratio (FAR), and the last was critical success index (CSI, Wilks 1995).

POD is defined as the percent of observed events that were forecast. Mathematically, this is represented by

$$POD = \frac{X}{X + Y}. \tag{3.1}$$

POD provides a general measure of how well a predictor can detect an event. For example, in this study, a low (i.e. less than ~0.4) POD was usually the result of too strict of a predictor. Therefore, the event would occur without ever being predicted. For this study, a high POD (i.e. greater then 0.8) was desired. As a result, any forecast criteria that resulted in a low POD was desired.

FAR is the ratio of non-successful forecasts to successful forecasts, mathematically represented as

$$FAR = \frac{Z}{(X + Z)}. \tag{3.2}$$

FAR provides a skill assessment on the accuracy of a predictor. A high (i.e., greater than ~0.60) FAR indicates that the predictor is predicting too many events and a more stringent predictor may be needed. Thus, a lower FAR is preferred.

CSI can be defined as an estimate of the conditional probability of an event provided that the event was observed, forecast, or both (Jolliffe and Stephenson 2003). CSI can also be defined more simply as the ratio of correct forecasts to the total number

of events plus the number of false alarms (Schaefer 1990). CSI is defined mathematically by

$$CSI = \frac{X}{(X + Y + Z)} \tag{3.3}$$

or

$$CSI = [(1 - FAR)^{-1} + (POD)^{-1} - 1]^{-1} \tag{3.4}$$

The no-forecast/no-event cases (W) were not considered in computing the skill scores used in this study. In fact, the CSI can be seen as the hit rate for a forecast event once the correct no-forecast/no-event cases are removed (Wilks 1995). Jolliffe and Stephenson (2003) note that CSI is often used on rare events since it is calculated without the use of correct rejections. However, as addressed by Schaefer (1990), CSI is proportional to the frequency of an event and assumes that cases for an event that is not expected or not observed are unimportant. Schaefer also showed how the CSI can be inflated by high frequency events and noted that CSI is a good indicator of the usefulness of different forecast techniques when applied to a consistent environment, including the effectiveness of various WSR-88D algorithms for a given WFO. Therefore, despite potential problems, CSI is used as the primary indicator of forecast skill in this study because of its continued widespread use in the forecasting community and to maintain consistency with previous lightning forecasting studies. However, caution should be used when comparing CSI between two different environments since it can be inflated by the frequency of events.

3. RESULTS

3.1 Radar Reflectivity Forecast Method

The ten-year WSR-88D and NLDN datasets were analyzed using the radar reflectivity forecast method; results are shown in Figures 3.1- 3.3 and listed in Tables 3.1-3.4. The results are broken down by the environmental level used, the range from the radar, the number of times the cell was identified by the CAPPI-SCIT algorithm, and the reflectivity value used in the forecast. The environmental levels are labeled such that E10, E15, and E20 represent the -10, -15, -20 °C isotherm levels, respectively, and U10 represents the updraft -10 °C level. The range was delineated by radial distance from the radar location (i.e., 75, 100, 125, and 150 km). The number of times the cell was identified by the CAPPI-SCIT algorithm, also called the track count, is the number of times the cell was *tracked* by the CAPPI-SCIT algorithm. Thus, 0 indicates 1 radar volume, 1 indicates 2 radar volumes, etc. The dBZ test values are the radar reflectivity values used in the forecast criteria. The results will be discussed considering the POD, FAR and CSI. The statistic of the greatest interest is the CSI because it combines both the POD and FAR, but an analysis of POD and FAR is also essential since it provides additional understanding on how a specific CSI value was obtained. For example, a situation with a high CSI (i.e. 0.6) can be obtained from a POD of 0.93 and a FAR of 0.37. In this case, the POD is high but so is the FAR suggesting that the forecast criteria were too easily met. Another example with a CSI of 0.6 is when the POD is 0.70 and the FAR is 0.2. This shows a different situation where the forecast criteria were hard to met, but were more accurate when met.

3.1.1 Environmental Level

When considering the four different isothermal criteria, E10, E15, and U10 has similar overall average CSIs (i.e., the average of each level's bars in Figure 3.1) of 0.53, 0.53, and 0.52, respectively. E20 had a slightly lower average CSI of 0.49. The best average POD of 0.86 was at E10, E15, E20, and U10 had average PODs of 0.77, 0.61, and 0.77, respectively. The best average FAR of 0.21 was found at the E15 and E20, E10 and U10 had average FARs of 0.32 and 0.33, respectively.

E10 and E15 have equivalent CSI values. However, the POD values suggest that E10 is the best detection level, which is expected since it is at a lower height. However, this increase in detection is countered by an increase in false alarms indicated by the higher FAR value. E15 is opposite in that it has a lower false alarm rate coupled with lower detection efficiency. Thus, there is the option to maximize detection or minimize false alarms when choosing isothermal levels for lightning forecasting purposes.

3.1.2 Range

The effect of the distance from the radar on the forecast statistics was examined since there is a degradation of radar resolution with range. Because the data in this study is interpolated to a Cartesian grid, the lower resolution data can sometimes yield significant errors, an issue that is discussed at length in Appendix A. At all environmental levels, there is a slight increase in the CSI as the range from the radar decreases (Figure 3.1). The average CSI values for 150, 125, 100 and 75 km were 0.48, 0.51, 0.53, and 0.56, respectively. Thus, including data out to 150 km versus 75 km decreases the CSI by 0.08.

The POD values show the same trend where the detection efficiency increases slightly with decreasing range (Figure 3.2). The average POD values for 150, 125, 100, and 75 km were 0.74, 0.74, 0.76, and 0.78, respectively. An average of 1.7 times more cells are identified for each range increment. For example, within 125 km from the radar, the number of cells with a track count of 2 is 15,872. This value decreases to 9,364 when the range is reduced to 100km. As with the average CSI values, only a small difference (0.04) is noted between the POD at 150 km and the POD at 75 km.

FAR values decrease with decreasing range (Figure 3.3). The average FAR values for 150, 125, 100, and 75 km were 0.36, 0.31, 0.30, and 0.29, respectively. An increase in FAR is expected with an increase in the number of identified cells as the range increases. The difference between the average FAR within 150 km and the average FAR within 75 km is 0.07, so changes in FAR contribute more strongly to the range-dependency of CSI than the changes in POD.

However, the range-dependency of each of the forecast statistics remains relatively low. As a result, confidence in lightning forecasts for cells close to the radar is similar to lightning forecasts for cells far from the radar. Monthly variability exists for various months within the dataset, but overall the distance from the radar appears to have only a small impact on the accuracy of the CG lightning forecasts.

3.1.3 Track Count

The number of times a cell was identified and tracked by the CAPPI-SCIT algorithm is represented by the count. A count of 0 represents cells that were identified by the CAPPI-SCIT algorithm for at least one scan. Likewise, a count of 1 represents cells that were identified and tracked for at least two consecutive scans. These categories include all of the identified cells within the specified range. The difference in the number of cells with a count of 0 and a count of 1 represents cells that were not identified in the previous or subsequent scans. A few situations could produce these types of cells. One possibility is that a cell develops ahead of a line or cluster of cells. This cell could be discrete enough to be classified as its own cell, but will quickly merge with the existing cluster. Summer convection in the Houston area is dominantly driven by mesoscale boundaries and therefore this is a likely possibility. It is theorized that this is the most common case of a cell being identified for only one cell, but more research will need to be done for confirmation. Another possibility is that a cell quickly strengthened so that the reflectivity and area criteria for identification are met for a single scan, but the cell then dissipates as quickly as it initialized, reducing its size and/or reflectivity values so that it is not classified during the next scan. These types of storms are also driven by mesoscale boundaries, but are usually more isolated and have a smaller areal extent. Cells of this nature are also very common over Houston, and more work will need to be done to determine whether this type of cell or the merging cell mentioned previously are more commonly identified on only one radar scan. One last possibility is that the storm is "created" as a result of the interpolation. At large distances from the radar, the interpolation scheme will have to smooth the data more to maintain the same resolution.

As a result, an area of reflectivity may be represented larger on the Cartesian grid than is actually observed. This could cause cells to be identified that do not actually meet the identification criteria. Cells identified in this manner are likely to disappear on the subsequent scan as different data is interpolated differently. In the discussion of the vertical resolution of the CAPPI data (Appendix A) some of these interpolation issues are addressed. For a range of 150 km, a total of 64,033 cells were identified while 37,094 were identified and tracked for at least two consecutive scans. As a result, there are 26,939 cells that were only identified for one scan. These cell are the least likely to produce lightning and therefore have low CSI values which brings down the average of the entire dataset with a minimum track count of 0.

As mentioned before, a count of 1 represents a cell that was *tracked* for at least 1 additional scan from its identification scan. Therefore, these cells have met the reflectivity and area requirements to be identified by the CAPPI-SCIT algorithm for at least 2 consecutive scans. At a range of 150 km, 37,094 cells were labeled with a track count of at least 1 while 25,776 cells were labeled with a track count of at least 2; thus 11,318 cells are only tracked for the subsequent scan following the identification scan. Many of the same possibilities mentioned for the cells that are only identified once are also probable here. However, the increased CSI values (Figure 3.1) show that lightning is more likely to occur in these cells than the cells that are only identified once.

A track count of 2 represents cells that were identified and then tracked for at least 2 subsequent scans. The scan time for each of the precipitation mode VCPs is approximately 5 min. This means that the cells in this category have been observed by the radar for at least 15 min. Cells meeting the CAPPI-SCIT algorithm for 3 consecutive

scans will be significant and will not be product of interpolation. Therefore, this category produces the best CSI and the main track count category of focus.

The average CSI of all identified cells is 0.44. Increasing the minimum track count to 1 yields an average CSI of 0.53 while increasing the minimum track count to 2 yields an average CSI of 0.60. Therefore, when the results are discussed in more detail, primarily cells with at least a track count of 2 will be primarily considered. However, a few cases with track counts of 1 will have important consequences.

FAR values decrease as the minimum track count increases (Figure 3.3). For all identified cells, the FAR is 0.39. The average FAR value decreases to 0.31 if only cells with a minimum track count of 1 are considered and to 0.25 if only cells with a minimum track count of 2 are considered. The difference is not as great as in the CSI values, but indicates an advantage in lightning forecasting using only cells with a minimum track count of 2.

POD values increase as the track count increases (Figure 3.2), just as the CSI. The average POD of all identified cells is 0.70. Increasing the minimum track count to 1 increases the average POD to 0.76 while increasing the minimum track count to 2 increases the average POD to 0.80. The difference between the average POD between maximum and minimum track counts is less than the differences for the CSI and FAR, which is encouraging. As mentioned previously, increasing the track count decreases the amount of identified cells. However, since the difference in POD is not large, this suggests that a number of cells being eliminated do not produce lightning, which was the desire of considering the track count. Increasing the track count past 2 could be considered. However, a track count of 2 was chosen as the maximum since, in most

cases, it provides enough time for storm electrification, charge separation, and lightning discharge.

3.1.4 Reflectivity Thresholds

The results are variable data when considering the different dBZ test values. Thirty and 35 dBZ had an average CSI of 0.55, while 40 dBZ had an average of 0.46. However, POD values decrease more dramatically as the reflectivity threshold increases. The average POD values when using 30, 35, and 40 dBZ are 0.90, 0.78, and 0.57, respectively – a decrease of 0.33 between 30 and 40 dBZ. The average FAR values decrease with increasing dBZ test value. The average FAR values when using 30, 35, and 40 dBZ are 0.40, 0.32, and 0.22, respectively. The difference between the average FAR when using the 30 and 40 dBZ test values, 0.18, is moderately significant. In terms of forecast value, FAR represents an opposite trend than the POD and CSI. Both POD and CSI suggest using the 30 dBZ test value, while the FAR suggests using the 40 dBZ test value.

3.1.5 Overall

Considering forecast criteria separately is essential for understanding of how each criteria affects the forecast; however, considering combinations of forecast criteria can yield more accurate results. Choosing the best overall predictor combination does not guarantee that it is the best combination in every situation, but it does provide a base from which the algorithm can be improved. For this point on, the best predictor will be determined by its CSI value. The POD and FAR will be considered to determine how the

CSI value was reached, but overall, the CSI will be the statistic that is maximized. Cases where the best overall combination does not perform well will be analyzed in Section 3.3.

Based on the CSI statistics in Figure 3.1 and Tables 3.1 – 3.4, *the best predictor combination for the entire dataset is 30 dBZ at the E20 level within 75 km of the radar with a track count of at least 2*. The CSI for this combination of forecast criteria is 0.71. It is interesting to note that E20 had the lowest overall CSI compared to the other environmental levels (Section 3.1.1), highlighting the importance of combining forecast criteria. However, 40 dBZ at E20 within 150 km and track count of 0 is the worst overall combination with a CSI of 0.28. Thus the specific choice of forecast criteria is critical. The average CSI using 30 dBZ at E20 is 0.60, while the average CSI using 40 dBZ at E20 is 0.33. Therefore, CSI seems to be the most sensitive to the reflectivity choice when combining a reflectivity threshold and an environmental height, with track count and range choices providing more moderate improvements in the lightning forecast.

Even though the best CSI value is 0.71, other predictors were close to this maximum value. The next best predictor combination (CSI = 0.69) was also found at the E20 level when using the 30 dBZ test value on cells within 100 km with a minimum track count of 2. At E10, the best predictor combination (CSI = 0.68) is the 35 dBZ test value used on cells within 75 km with a minimum track count of 2. At both the E15 and U10 levels, the best predictor combination use 30 dBZ on cells within 75 km with a minimum track count of 2 (CSI = 0.68 and 0.67, respectively). In all, 33 (or 22%) of the possible 144 predictor combinations had a CSI greater than or equal to 0.60. None of these combinations included a track count of 0. In only one instance (30 dBZ at E20) including cells out to 150 km yielded a CSI over 0.60. The greatest CSI using the 40 dBZ, 0.67,

was found at the E10 level when considering only cells within 75 km with a minimum track count of 2. Forty dBZ generally performs better at E10 because of low FAR values (whereas 30 dBZ at this height can sometimes have unacceptability high FAR values). Out of all the predictors, 144 total, 14 (or %10) have a CSI less than or equal to 0.400. All but one of these combinations uses 40 dBZ as a reflectivity threshold.

3.1.6 Comparison to Previous Studies

Results from previous studies are shown in Table 3.5 and are discussed in detail in Section 1.4. This section will focus on comparing results from previous studies with the results of this study. For example, Beuchler and Goodman (1990) found a POD of 1.00, a FAR of 0.20, and a CSI of 0.80 when using 40 dBZ at -10 °C isotherm while this study found an average CSI of 0.54 for the same criteria. It is likely that this discrepancy is a result of the number of cells analyzed. Their study only analyzed 20 cells while this study analyzed 65,339.

Results from Gremillion and Orville (1999) are compared to the results from this study in Table 3.6. Their criteria was slightly different than those used in this study since they required the criteria to be met for at least two consecutive scans, while this study only required for it to be met for one scan. Therefore, comparison between the two results should used cautiously, but the results are presented and compared here because of the study's prominence in lightning forecasting (Tim Oram, personal communication). All of the comparable CSI values are higher for the Gremillion and Orville study except when using 30 dBZ at -20 °C isotherm. POD is higher for this study in all except one case because Gremillion and Orville required the criteria to be met for at least two

consecutive scans. For the same reason, the FAR values are higher in this study. Gremillion and Orville found 40 dBZ at -10 °C to be the best predictor pair while this study found 30 dBZ at -20 °C to be the best. As with Buechler and Goodman (1990), the number of cells analyzed by Gremillion and Orville (1999) is much less than the number analyzed by this study (39 compared to 65,399), which also explains the differences between the two studies since, as seen in this study (Table 3.1-3.4), the statistics increase as the number of analyzed cells decreases.

Results from Vincent et al. (2003) are directly compared to the results of this study in Table 3.7. The CSI in Vincent et al. are higher than the values in this study in all cases. This appears to be a result of the higher POD values for their study, which is likely a result of the difference in dataset size. Many of the days analyzed for this study showed similar results as Vincent et al. suggesting that the lower results for this study are most likely a result of the large dataset.

Wolf (2006) analyzed 1,100 cells using 40 dBZ at the -10 °C updraft level and found a POD of 0.96, a FAR of 0.11, and a CSI of 0.83. This study found a POD of 0.59, a FAR of 0.23, and a CSI of 0.48. If only cells within 75 km will a minimum track count of 2 are considered the POD becomes 0.69, the FAR becomes 0.14, and the CSI becomes 0.60. The difference in these results is much greater than the difference in the results from the other studies. There are a few different explanations: 1) the convection in Florida, the main location of Wolf's study, could be more robust, therefore reaching the updraft -10 °C more frequently, 2) the subjective nature of using the -10 °C updraft level, and/or 3) the difference in the number of cells analyzed. The most likely explanation appears to be (1). Wolf's results showed a POD of 0.99 when using the 40 dBZ at the -6

°C updraft level, which is near the location of the -10 °C isotherm. The results from this study showed an average POD at this level of 0.74. This difference alone shows that the cells considered for Wolf's study were more robust, since almost all of them had 40 dBZ at approximately the -10 °C level. This may be also result from using a subjective method to identifying cells.

3.2 VII Forecast Method

The analysis of the entire dataset using the VII forecast method is shown in Figures 3.4 – 3.6. As described in Section 2.6, the VII forecast method compares the cell-based VII values to the probability distribution function percentile values to make a lightning forecast. As in the radar reflectivity method, the forecasts separated by range from the radar and how many times a cell was tracked by the CAPPI-SCIT algorithm. In Figures 3.4 – 3.6, only those cells with a minimum track count of 2 were considered since it was determined in Section 3.1 to provide the most accurate forecasts. Forecast variations by range from the radar and VII percentile value will be considered.

3.2.1 Percentile Value

The results in Figure 3.4 show an increase in the CSI values from the lowest VII percentile (i.e., > 0.0 kg m^{-2}) to the 20th VII percentile (i.e., > 0.740 kg m^{-2}) and then a decrease thereafter. The VII percentiles used are shown in Table 3.8. Thus, the best overall predictor is the 20th percentile, which was found at a value of 0.740 kg m^{-2}, with an average CSI of 0.64. The percentile predictors on either side of the 20th percentile, the 15th and 25th percentiles yielded average CSI values of 0.63. After the 35th percentile,

which has an average CSI of 0.61, the CSI values begin to drop off significantly, dropping below 0.50 at the 55th percentile, below 0.20 at the 80th percentile, and below 0.05 at the 95th percentile. The lower percentile (below 50 percent) forecasts show approximately the same skill as the radar reflectivity method forecasts, apparently resulting from high POD instead of low FAR.

POD values for the entire dataset are shown in Figure 3.5. POD at lower percentiles is high, remaining above 0.90 until the 25th percentile and then dropping approximately 0.05 every 5 percent. POD values drop below 0.50 at the 60th percentile, below 0.30 at the 75th percentile, and below 0.05 at the 95th percentile, following the same trend as the CSI values. FAR values, shown in Figure 3.6, show similar trends as the POD value. FAR is above 0.30 until the 25th percentile, above 0.20 until the 45th percentile, and above 0.10 until 75th percentile.

An interesting result is the moderate CSI, 0.600, for the lowest percentile value of 0.0 kg m^{-2}. As a result, a forecast is made whenever the VII is greater than 0 kg m^{-2}. Since VII is only calculated between 7km and 11km, this result shows that any time echo reaches 7 km within a tracked cell, there is a potential for CG strikes. The best CSI values were between the lowest and 25th percentile, where the VII is less than 1.0 kg m^{-2}. This information is very valuable when considering the ease of which a lighting forecast can be made. The environmental level does not need to be known, which is beneficial for sites like Houston that do not have a sounding. However, the CSI values never reach above 0.65. Therefore, VII alone may not be the best predictor, but combining VII values with the reflectivity threshold method shows promise and is discussed in Section 3.4. If maximization of CSI value is desired, the 20th percentile test value should be used.

If maximization of POD value is desired, only a test of whether the VII is greater than 0 should be used.

3.2.2 Range

As in the radar reflectivity method, VII-based CSI values indicate only a small range dependency, i.e., CSI increases slightly as the range decreases (Figure 3.4). At 150 km the average CSI is 0.42, which increases to 0.45 at 125 km, 0.47 at 100 km, and 0.50 at 75 km. This result suggests that while considering range is beneficial, it is a secondary consideration. If a maximization of the CSI is desired, only cells within 75 km should be analyzed.

3.2.3 Overall

The best VII predictor was found when using a test value of 0.734 kg m^{-2} (20^{th} percentile) in cells within 75 km of the radar, resulting in a CSI of 0.68. The best predictor combination using the radar reflectivity method had a CSI of 0.71, so the values are comparable. The highest POD value, 1.0, was found when using a VII of 0.0 kg m^{-2} on cells within 100 km. The lowest FAR, 0.01, was found when using a VII of 8.45 kg m^{-2} on cells within 75 km. The maximum in the CSI values seen at the 20^{th} percentile at every range represents the best optimization of the high POD values and the low FAR values. Using any VII above the 45^{th} or 50^{th} percentile lowers the FAR to below 0.20, but it also drops the POD to below 0.80, which yields a CSI of below 0.50. The best VII values, from 0^{th} to 25^{th} percentile, all have VII values lower than 1.0 kg m^{-2}. Therefore, incorporating a VII threshold into the radar reflectivity method may be beneficial.

3.3 Case Studies – Low CSI

As mentioned in Section 3.1.5, CSI averages from the multi-year data can differ significantly from daily or monthly averages. In this section, select case studies are analyzed to better understand of the types of situations that produce large variations in CSI values. The analysis will first look at cases with a low overall CSI; only the cells with a track count of at least 2 are considered.

An understanding of why some months have very low CSI values is important in the lightning forecasting algorithm development. For example, the lowest monthly CSI using the radar reflectivity method was found for June 2000 which had an average CSI of 0.38 based on all predictor combinations. A total of 707 cells were identified for the month compared to the monthly average of 859 for the entire dataset. So June 2000 is below average in the number of cells, but not significantly. Therefore, it is not immediately clear why June 2000 indicates such a low CSI value.

A total of 138 days in the ten years of summer data had a CSI less than 0.35. Of those days, five had a cell total of 100 or more and 27 had a cell total between 10 and 20. A day from each of those subsets will be examined in further detail to determine if there is a pattern for either situation.

3.3.1. Low CSI / High Cell Number - 11 June 2000

A total of 105 cells were identified on the 11 June 2000, and the average CSI based on all predictor combinations was 0.32. In addition, the average POD was 0.86 and the average FAR was 0.63. The high POD shows that the cells that produced lightning were correctly identified, but the high FAR shows that many of the tracked cells

meeting the reflectivity forecast criteria did not produce lightning. CSI averages for the day using the E10, E15, E20, and U10 level were 0.21, 0.29, 0.48, and 0.29, respectively, so all levels except E20 performed very poorly. This is in contrast to the June 2000 CSI averages of 0.35, 0.43, 0.38, and 0.38, where all environmental levels performed consistently. June 11th POD averages were 0.89, 0.89, 0.77, or 0.89 and FAR averages were 0.78, 0.69, 0.37, or 0.69 for the respective environmental levels, so it appears that the much lower FAR values at E20 contributed to the significantly better CSI value. It remains to be determined what synoptic, mesoscale, and/or convective variations caused the E20 level to be a significantly better predictor for this day.

The created KHGX soundings for 11 June 12Z and 12 June 00Z show a typical day over Houston with precipitable water values from 1.75 in (12Z) to 1.37 in (00Z) and modest CAPE from 599 J kg^{-1} (12Z) to 1462 J kg^{-1} (00Z). Radar images from June 11th at 1403, 1703, 2004, and 2304 Z are shown in Figure 3.7. This figure shows numerous cells developing north of the radar location. The cells begin developing within 75 km of the radar at 1403 Z and quickly increase in number and move northward until the majority of cells are between 100 and 150 km from the radar. The cells are all within close proximity to each other, but are still separate enough to be classified as individual cells by the CAPPI-SCIT algorithm (cell centroids are indicated by crosses). This type of situation causes difficulty for the automated forecasting and verification process utilized in this study since the small spatial extent of each cell causes many cells to be identified. Also, the closeness of the cells makes the correct lightning correlation difficult. The number of identified cells starts at 2 at 1403 Z, then increases to 30 at 1703 Z, then

decreases to 16 at 2004 Z, and 6 at 2304 Z. The maximum number of cells identified for one scan was 34 for the scans started at 1628 and 1633 Z.

A total of 715 flashes were observed within 150 km of KHGX and were correlated to 19 identified cells. Table 3.9 shows the number of flashes correlated to each cell ID. It is important to note that cell IDs are reused. Therefore, if two different flashes are correlated to cell ID 1 that does not necessarily mean that they are correlated to the same cell. A cell ID is kept until the cell that was identified by that ID number is no longer identified by the CAPPI-SCIT algorithm. However, strikes correlated to cells that retain the same cell ID for numerous sequential scan are most likely correlated to the same cell.

Cell 4 was identified and tracked from 1713 to 1858 Z (Figures 3.8 – 3.13) and 95 CG strikes were correlated to this cell during this period. At 1713 Z (Figure 3.8) the cell was just beginning to develop and had a maximum reflectivity of 43 dBZ, a VIL of 4.11 kg m^{-2}, a VII of 0.05 kg m^{-2}, and a maximum echo height of 12 km. At 1748 Z (Figure 3.9), before any strikes were correlated to this cell, the maximum reflectivity had increased to 55 dBZ, VIL had increased to 26.29 kg m^{-2}, and VII had increased to 3.28 kg m^{-2}. The next scan, (1753 Z; Figure 3.10) shows a dramatic increase in VIL and VII as well as 5 CG strikes which are correlated to the cell (indicated by Xs on the x-axis of the time series). At 1758 Z (Figure 3.11), VIL is slightly less than the previous scan, VII has increased, and 18 CG strike were correlated to the cell. The cell shows slight weakening in the next scans (1803 Z; Figure 3.12) but the number of CG strikes correlated to the cell increases to 26. The cell continues to weaken from 1803 Z until 1858 Z, when it is no longer identified by the CAPPI-SCIT algorithm. Figure 3.13 shows the cell at 1858 Z.

As can be seen, the maximum reflectivity, VIL, and VII values have dropped significantly from 1813Z until the current scan.

Cell 12 was identified and tracked from 1728 to 1838 Z and no CG strikes were correlated to the cell. The cell was first identified at 1728Z (Figure 3.14) and showed similar initial characteristics as Cell 4. Cell 12 had a maximum reflectivity of 44 dBZ, a VIL of 2.9 kg m^{-2}, and a VII of 0.03 kg m^{-2}. The next scan (1733 Z; Figure 3.15) shows some more vertical growth and an increase in all of the time series variables. The 1738 Z scan (Figure 3.16) shows a slight increase in the maximum reflectivity, but the VIL and VII both decreased suggesting limited vertical development. The 1758 Z scan (Figure 3.17) shows a gradual rise in maximum reflectivity and VIL while VII remained constant. The final scan this cell was identified (1833 Z; Figure 3.18) shows a gradual decrease in maximum reflectivity and VIL and constant VII.

The greatest difference between the radar measurements of these two cells appears in the VIL and VII values. The cells show very similar traits on their initial identification (Figure 3.8 and Figure 3.14). However, cell 4 continued to grow vertically, increasing both VIL and VII values rapidly, while cell 12 showed promise of vertical growth, but ultimately remained weak. Both cell 4 and cell 12 met the 30 dBZ at E10 forecast criteria immediately. Using E20 would have eliminated the false alarms created by cell 12. However, using E10 in conjunction with VIL or VII may also decrease FAR values in these types of cells.

3.3.2 Low CSI / Low Cell Number – 25 August 2000

There are a total of nine days in the ten-year dataset where the CSI was less than 0.35, the number of identified cells was between 10 and 20, and at least one cell was identified within 75 km. Out of these nine days, only three had a POD greater than 0.9, and only one of those three had over 50 flashes. That day, 25 August 2000, is analyzed in more detail to identify why the CSI value was so low.

The created KHGX sounding for 12 Z on 25 August 2000 and 00 Z on 26 August 2000 shows a moderately moist (precipitatable water values of 1.83 in at 12 Z and 1.58 in at 00 Z), and unstable (CAPE values of 552 J kg^{-1} at 12 Z and 4365 at 00 Z) J kg^{-1}. Figure 3.19 shows the radar images from 1617 Z, 1802 Z, 2012 Z, and 2247 Z. Figure 3.19 (2012 Z; top-left) shows 5 cells southwest of the radar with one cell at a distance of around 75 km from the radar while the others are 150 km from the radar. Figure 3.19 (top-right) shows a large cluster of cells between 100 and 150 km from the radar. At this point there are 3 identified cells, one of which was identified at 1617 Z. Figure 3.19 (2247 Z; bottom-left) shows that the large cluster of cells has dissipated and only small single cells remain and Figure 3.19 (bottom-right) shows the last identified cell for the day. The radar images show that despite ample convective energy, the lack of synoptic or mesoscale forcing limited the number of cells that developed. Also, the distance from the radar creates an issue. The images shown are CAPPI plots at 1 km altitude. As a result, much of the data shown on the plots is a result of interpolation. A radar beam with an elevation angle of 0.5° will be above 1.0 km in a normal atmospheric beginning at around 77 km. The beam height, given an elevation angle of 0.5°, at 100 km is approximately 1.4 km and at 150 km is approximately 2.5 km. As discussed in Section

2.1.3, the radius of influence for a point is 1.25 km in the x and y directions, and 1.75 km in the z direction. Therefore, the data shown in the figures is a result of the interpolation of the data at higher heights. This interpolation should not adversely affect the data since the same interpolation scheme is used on the entire dataset and there must be data present for interpolation to occur. The most likely explanation of the data at 1 km is that reflectivity values shown were measured at the lowest elevation scan. Figure 3.20 (an NCDC image at 1802 Z) shows the data from the lowest elevation angle in PPI format and confirms that the data shown in Figure 3.19 (top-right) is from the lowest elevation scan.

A total of 86 flashes were observed within 150 km of KHGX on 25 August 2000 and were correlated to four cells. Table 3.10 shows the number of flashes correlated to each cell ID. The majority of flashes (65) were correlated to cell ID 2, while 16 were correlated to cell ID 0, 4 were correlated to cell ID 5, and 1 was correlated to cell ID 3.

Cell 2 was identified for a total of three hours from 1617 to 1917 Z. Figure 3.21 shows the cell on the scan after is was identified (1622Z). Maximum reflectivity and VIL values are low, but the VII suggests that there are already hydrometeors being lifted above 7 km. Growth is seen on the next scan (1627 Z; Figure 3.22) as all of the values increase. Figure 3.23 shows cell 2 when the first strike was correlated (1657 Z). The time series show a spike at 1642 Z followed by a decrease in all measured values. However, while the VIL remains moderate at 14.8 kg m^{-2}, both the maximum reflectivity and VII suggest a stronger cell. Since VII begins its calculation at 7 km, the high VII values show that a large amount of precipitation mass is above this level. Figure 3.24 (1757 Z) shows the time series of the cell for the hour between 17 and 18 Z. Two

"jumps" are seen in the data with the first around 1727 Z and the second around 1737 Z. These "jumps" are followed by CG strikes. Figure 3.25 shows the final hour (17-18Z) of the cells lifetime. Jumps in the time series data is still noted, but CG strikes are occur throughout and do not follow the jumps as in the last hour. This suggests that the initial "jump" or first few "jumps" are the most important indicators in attempting to forecast the first flash, but do not indicate flash potential thereafter.

The lifetime of cell 1 is shown in Figure 3.26. No CG strikes were correlated to this cell. The maximum reflectivity and VIL values are comparable to those in cell 4, but the VII values are less. Also of note, are the quick increases ("jumps") in the reflectivity and VIL values, but only minor variations in VII. This is in contrast to the observations of cell 4, which had quick increases of maximum reflectivity, VIL, and VII and produced a high number of CG strikes. Also, the VII for this cell is less than 1 kg m^{-2} in all but one scan. This represents a lack of precipitation mass above 7 km, which is the most likely cause of the lack of CG lightning.

3.4 First Flash Forecast Time

In addition to testing the accuracy of the forecast, the lead time to the first flash was calculated for the reflectivity threshold and VII methods. Only the first flashes were considered because the forecast times would be greatly exaggerated otherwise. For example, if a cell is tracked for three hours, as was the case for cell 2 in Section 3.3.1.2, the forecast times would continue to increase since the first forecast is made early in the cell's lifetime. For the radar reflectivity method (Figure 3.26) the average forecast times were 16.9, 13.4, 10.0, and 14.2 min for E10, E15, E20, and U10, respectively. Averaging

all the forecast times for the VII method is not as straight forward since there were a large number of possible values (Figure 3.27). Thus, the 0-25th, 25-50th, 50th – 75th, and 75th-95th percentile ranges were averaged and yielded an average forecast time of 18.2, 12.0, 5.8, and 1.4 min, respectively. As seen in Figure 3.27 and represented by the forecast times, a large decrease from the 0th to 95th percentile is observed. This decrease is a result of the correlation between the forecast time and the POD. The largest forecast times follow the highest POD values. As shown by Figures 3.2 and 3.5, both the radar reflectivity and VII method forecast times follow the high POD values. This is to be expected since higher POD values signal that a predictor is easily met, which in turn creates a longer forecast time. The only difference is that the forecast time is maximized at larger distances while the POD is maximized within 75km. Since the differences are minor, a maximization of the POD can be used as a maximization of the forecast time.

The best POD for the radar reflectivity method (0.99) was found when using 30 dBZ at E10 on cells within 75 km with a minimum track count of 2. Using this predictor combination, the average forecast time is 17.5 min. For the VII method, the best POD (1.0) was found using 0.0 kg m^{-2} at 100km. Using this predictor combination, the forecast time is 19.4 min. In both methods, the best forecast times, 21.8 min for the reflectivity method and 23.1 min for the VII method, were found using the same thresholds but within 150 km. The average forecast time of using the VII method on the 0-25th percentile was higher than the average of using any of the environmental test levels for the radar reflectivity method. This matches the POD data. The average POD using the 0-25th percentiles was 0.94, while the POD averages at E10, E15, E20, and U10 were 0.90, 0.81, 0.66, and 0.811, respectively. As a result, the VII method provides better lead

times than the radar reflectivity method. This is encouraging because, as mentioned earlier, the VII forecast method is simpler than the radar reflectivity method. In fact, the best lead times for the VII forecast method were found when using 0.0 kg m^{-2} as the threshold value. This means that for the highest lead times the only test that is needed is whether any precipitation-size echo is above 7 km. The average FAR when using 0.0 kg m^{-2} as the test value is 0.40, which is not unacceptably high. Therefore, the VII method provides an easy and reliable tool that can be used to maximize forecast time. If the radar reflectivity method is still desired, the best environmental level for the maximization of the forecast time is E10, which has an average forecast time of 16.8 min and an average FAR of 0.32. The best reflectivity value is 30 dBZ, which has an average forecast time of 17.6 min and an average FAR of 0.33. The results do vary slightly by range, therefore increasing the maximum range to 150 km improves the forecast times at the expense of the FAR.

3.5 Lightning Forecasting Algorithm (LFA) Development

Using the two days discussed in Section 3.3, various predictor combinations are tested to determine the optimal lightning forecasting algorithm (LFA), with emphasis on optimizing CSI and forecast time. As discussed in Section 3.1, if using the radar reflectivity method and maximization of the CSI is desired with only one predictor, the E10 level, using only cells with a minimum track count of 2, and 30 dBZ are the predictors of choice. However, the best overall predictor combination was 30 dBZ at E20 for cells within 75 km of the radar with a minimum track count of 2. The best predictor using the VII method was testing if VII was greater than 0. Combining these two

methods may provide better results than either one individually. Since the emphasis of this study is improving CG forecasting skill and lead time, the basis of the algorithm will use 30 dBZ at E20 since it provides the greatest CSI.

3.5.1 Development of a VII Threshold

Recall that for 11 June 2000 the average CSI was 0.32, the average POD was 0.86, and the average FAR was 0.63. Using 30 dBZ at E20 level on cells with a minimum track count of 2 and a range of 75 km results in a CSI of 0.07, a POD of 1.0, and a FAR of 0.93. Using 0.0 kg m^{-2} for the VII method on cells within 75 km yields a CSI of 0.06, a POD of 1.0, and a FAR of 0.93. Thus, both optimized forecast methods yield similar results for this day, in part because all the lightning producing cells had VII greater than zero. This is likely the case for many days. Therefore, the LFA needs to be strengthened.

The best predictor combination for this day using the radar reflectivity method is 40 dBZ at E20 resulting in a CSI of 1.00. The easiest change to make is to have the CSI maximizing LFA switch to using 40 dBZ at E20 instead of 30 dBZ, when the cell numbers increase above 100. However, there are two problems with that strategy: (1) it does not work in a real-time setting because the previous 99 cells would be forecast using the previous method and (2) only 48 of 626 cases have a larger CSI when using 40 dBZ at E20 instead of 30 dBZ when only cells within 75km are considered. Therefore, increasing the VII test value provides an easier way to strengthen the algorithm without have to change the environmental height or reflectivity thresholds.

As mentioned in Section 3.3.1.1, there were 715 flash correlated to cells on June 11th. The average VII value for those cells was 2.64 kg m^{-2}, which is near the 60th percentile for the entire dataset. This percentile is likely a result of a large number of the flashes (115) being correlated to a single cell. If cells with VII less than 2.56 kg m^{-2} (60th percentile) are excluded, the values become those listed in Tables 3.11-3.14. These values show significant improvement from the values using either the radar reflectivity or the VII forecast method alone. The CSI using 30 dBZ at E20 increased from 0.07 to 1.00 for cells within 75km. When using the 40 dBZ test at the same level, the CSI stayed a 1.00. The CSI values increased for each different criterion for this day.

Taking a slightly lower percentile (30th) that corresponds to a VII of 1.089 kg m^{-2}, produces the results shown in Tables 3.15-3.18, which indicate a minimal increase in the forecast statistics. Tests were also run on the 50th and 75th percentile, a VII of 1.984 and 3.816 kg m^{-2}, respectively. Using the 50th percentile produced an average CSI of 0.51, while using the 75th percentile produced an average CSI of 0.52. Therefore, using the 60th percentile provides the best maximization of CSI for this day.

Recall that for 25 August 2000 the average CSI was 0.33, the average POD was 0.94, and the average FAR was 0.64. The result of using 30 dBZ at E20 on cells with a maximum track count of 2 and a maximum distance of 75 km is a CSI of 0.00 because no flashes were detected in the cells within 75 km, which leads to a FAR of 1. Increasing the distance to 150 km yields an average CSI 0.36, an average POD of 1.00, and an average FAR of 0.64. Thus, the reflectivity-only LFA did not improve the CSI values.

As mentioned in Section 3.3.1.2, there were 86 flashes correlated to cells for this day. The average VII for those cells was 1.71 kg m^{-2}, which is near the 45th percentile. If

cells with a VII less than this value are excluded, the average CSI increases to 0.56. Increasing the test value to the 60th percentile increases the average CSI to 0.60, while increasing the test value to the 75th percentile value decreases the CSI to 0.17. The data show that for both of the days, using the 60th percentile VII value produces a maximum in CSI.

To test combined reflectivity/VII LFA more thoroughly, analysis was performed on the months of June, July, and August of 2006. There were a total of 691 cells identified in June, 1466 identified in July, and 962 identified in August compared to the average monthly total of 891 for the entire 10-year dataset. The three-month average CSI using the reflectivity-only LFA is 0.56. When the combined LFA is used on the dataset the statistics reveal some problems. In particular, the average CSI decreases to 0.39. Therefore, while the 60th percentile test value increased the CSI for the two days previously analyzed, it leads to a lower CSI when executed on a monthly scale. This is most likely the result of the types of days chosen. Since each of these days had cells that produced a high number of lightning strikes per cell, it is probable that the cells had higher VII values, which is increased the average VII values for those days. This agrees with Motley (2006), who showed that VII is positively correlated to flash rate. Therefore, the higher percentiles may be useful in predicting which cells will produce a high number of flashes, but more research will need to be done in this area.

As a result of the failure of the 60th percentile VII threshold, tests using the 10th, 20th, 30th, 40th, and 50th percentile values were performed in attempt to determine the optimal value. The results are shown in Table 3.19 and indicate that the best percentile threshold was the 20th, but that the average CSI is slightly less than that based on the

reflectivity-only LFA. However, the average is higher for June and July using the 20th percentile VII value than just the radar reflectivity method alone. *The 20th percentile value is the same value that showed a maximum CSI for the entire dataset. As a result, this value is chosen as the additional parameter added to the LFA to maximize CSI.*

4. CONCLUSIONS

Previous research has shown the potential of forecasting cloud-to-ground (CG) lightning using radar reflectivity thresholds at various isothermal heights. This study extends those results to Houston, Texas by objectively analyzing a multi-year summertime dataset that includes a factor of 500 more cells in the analysis than in any previous publication. This study also incorporates a new radar-derived parameter, vertically integrated ice (VII), into the radar-based lightning forecasting method. The main results are as follows:

1) *Using 30 dBZ at the -20 °C isotherm on cells within 75 km of the radar and with a minimum track count of 2 is the best predictor combination for the Houston area, producing an average CSI of 0.71*.

The results of this study suggest different criteria than Gremillion and Orville (1999) and Vincent et al. (2003), which both recommend 40 dBZ at the -10 °C isotherm as the best predictor combination. Using those criteria produced an average CSI of 0.54 for this study. For most predictor combinations in this study, 40 dBZ had significantly lower CSI than either 30 or 35 dBZ, while the CSI values when using 30 and 35 dBZ were close. This difference suggests: 1) cells reaching 40 dBZ occur less frequently over Houston than either Florida (the location of Gremillion and Orville 1999) or North Carolina (the location of Vincent et al. 2003) and/or 2) the objective algorithm of this study resulted in more weak cells compared to the subjective cell identification in the other studies. The optimal environmental level in this study (-20 °C isotherm) likely better represents the depth mixed-phase hydrometeors need sufficient cloud

electrification. Thirty dBZ at -10 °C (beginning of the "charging zone") is not as likely to produce ample cloud electrification as 30 dBZ at -20 °C. A test analyzing instability at the -10 °C level may be more appropriate to show the likelihood of continued convection if -10 °C is the desired forecast level.

2) *Limiting the analysis to include only cells that had been tracked for at least two scans improved the forecast statistics more than varying the range from the radar or the reflectivity threshold.*

When considering the individual predictors, including only cells tracked for at least two scans improved the forecasts statistics the most, with the CSI average increasing from 0.44 when considering all identified cells to 0.60 when considering only cells with a minimum track count of 2. In addition, the best CSI values at every level were found when considering only cells with a minimum track count of 2. Strong, long-lived cells are more likely to have time to loft the amount of hydrometeors needed for ample cloud electrification.

3) *Using cell-based VII values to forecast cloud-to-ground (CG) lightning shows promise.*

VII-based CSI values were often comparable to the reflectivity threshold method and, the ease of the VII forecast method provides the NWS an easy to implement and effective method of forecasting CG lightning. Forecasts made using the predictor of VII greater than zero produced an average CSI of 0.60. The best forecast value for this study was using the 20^{th} percentile, VII of 0.74 kg/m^2,

which produced an average CSI of 0.64. The CSI values stay above 0.60 until after the 35th percentile VII value. Since VII only considers reflectivity above 7 km, any time VII is greater than zero, precipitation mass (i.e., rain, snow, graupel, and/or hail) has reached a height needed for cloud electrification, while any increase of VII over 0.74 kg m^{-2} is shown to represent a sufficient amount of precipitation mass for cloud electrification.

4) *The best first flash forecast time was 21.8 min when using the 30 dBZ test value at -10 °C on all cells within 150 km with a minimum track count of 2.*

This forecast time was greater than in previous study. If the number of times a cell is tracked is not considered, the forecast time is 16.9 min. This result is consistent with the forecast time of 16.1 min found by Clements and Orville (2008). The average forecast time when using the 0-25th percentile VII values was 18.2 min.

5) *A combination of the radar reflectivity forecast method and the VII forecast method can be used to provide better results.*

When testing the combined lightning forecasting algorithm on summer months from 2006, June and July showed improvement in their average CSI values when including the 20th percentile VII value, while the August had a slightly reduced CSI. Thus, VII values can be added to the radar reflectivity test method to improve forecasts. In the cases when there is a reduction, it is small. In two case

studies, where there was a large amount of lightning, incorporating the VII value significantly improved the lightning forecasts.

6) *The data from this study was used to create a lightning forecasting algorithm that runs in real-time and produces a categorical risk for lightning on a cell-by-cell basis.*

While this study provides the most thorough and objective analysis of using radar reflectivity at an isothermal level to date, more work will still need to be done to find the best predictors at different locations. This study was designed to be easily reproducible so that other WFOs could perform their own analysis and find the criteria which work best for their area. Additional research also needs to be done with VII, including correlation of VII with various atmospheric parameters such as convective available potential energy (CAPE), lifted index, and wind shear as well as cloud-to-ground flashes rates. More work also needs to be done with rapid changes in VII. This study showed VII "jumps" often precede cloud-to-ground flashes. There is also a possibility that rapid changes in VII could signal lightning cessation.

In addition, the lightning forecasting algorthim could potentially benefit from the addition of total lightning data. Clements and Orville (2008) showed that the radar reflectivity method alone is better than using total lightning to predict CG lightning, but the combination of the two methods has not been studied. The additional research with VII and total lightning has the potential to create an even more robust algorithm that

could be very effective and easily implemented at various WFOs across the United States.

REFERENCES

Amburn, A. A., and P. L. Wolf, 1997: VIL density as a hail indicator, *Wea. Forecasting*, **12**, 473 – 478.

Baker, B., M. B. Baker, E. R. Jayaratne, J. Latham, and C. P. R. Saunders, 1987: The influence of diffusional growth rate on the charge transfer accompanying rebounding collisions between ice crystals and hailstones. *Quart. J. Roy. Meteor. Soc.*, **113**, 1193-1215.

Barnes, S. L., 1980: Report on a meeting to establish a common Doppler radar data exchange format, *Bull. Am. Meteorol. Soc.*, **61**, 1401 – 1404.

Battan, L. J., 1973: *Radar Observation of the Atmosphere*. University of Chicago Press, 324 pp.

Biagi, C. J., K. L. Cummins, K. E. Kehoe, and E. P. Krider, 2007: National Lightning Detection Network (NLDN) performance in southern Arizona, Texas, and Oklahoma in 2003 – 2004. *J. Geophys. Res.*, **112**, D05208, doi: 10.1029/2006JD007341.

Berger, K., R. B. Anderson, and H. Kroninger, 1975: Parameters of lightning flashes. *Electra,* **80**, 223-237.

Black, R. A., 1990: Radar reflectivity – ice water content relationships for use above the melting level in hurricanes. *J. Appl. Meteor.*, **29**, 955-961.

Boudevillian B., and H. Andrieu. 2003: Assessment of vertical integrated liquid (VIL) water content radar measurements. *J. Atmos. Oceanic Tech.*, **20**, 807 – 819.

Brooks, I. M., C. P. R. Saunders, R. P. Mitzeva, and S. L. Peck, 1997: The effect on thunderstorm charging of the rate of rime accretion by graupel. *Atmos. Res.,* **43**, 277-295.

Brown, R. A., V. T. Wood, and D. Sirmans, 2000a: Improved WSR-88D scanning strategies for convective storms. *Weather and Forecasting*, **15**, 208-220.

Brown, R. A., J. M. Janish, and V. T. Wood, 2000b: Impact of WSR-88D scanning strategies on severe storm algorithms. *Weather and Forecasting*, **15**, 90-102.

Buechler, D. E. and S. J. Goodman, 1990: Echo size and asymmetry – impact on NEXRAD storm identification. *J. Appl. Meteor.*, **29**, 962-969.

Carey, L. D., and S. A. Rutledge, 1996: A multiparameter radar case study of the microphysical and kinematic evolution of a lightning producing storm. *Meteorology and Atmospheric Physics,* **59**, 33-64.

_____, and _____, 2000: The relationship between precipitation and lightning in tropical island convection: A C-band polarimetric study. *Mon. Wea. Rev.,* **128**, 2687-2710.

Clements, N. C. and R. E. Orville, 2008: The warning time for cloud-to-ground lightning in isolated, ordinary thunderstorms over Houston, Texas. *3rd Conf. on Meteorological Applications of Lightning Data*, New Orleans, LA, Amer. Meteor. Soc.

Cummins, K. L., M. J. Murphy, E. A. Bardo, W. L. Hiscox, R. B. Pyle, and A. E. Pifer, 1998: A combined TOA/MDF technology upgrade of the U.S. National Lightning Detection Network. *J. Geophys. Res.*, **103**, 9035 – 9044.

_____, J. A. Cramer, C. J. Biagi, E. P. Krider, J. Jerauld, M. A. Uman, and V. A. Rakov, 2006: The U.S. National Lightning Detection Network: Post-upgrade status. *2nd Conf. on Meteorological Applications of Lightning Data*, Atlanta, GA, Amer. Meteor. Soc., CD preprints.

Curran, E.B., R. L. Holle, and R. E. Lopez, 2000: Lightning casualties and damages in the United States from 1959 to 1994. *J. Climate*, **13**, 3448-3464.

Deierling, W., W. A. Peterson, J. Latham, S. Ellis, and H. J. Christian, 2008: The relationship between lightning activity and ice fluxes in thunderstorms. *J. Geophys. Res.*, **113**, D15210, doi:10.1029/2007JD009700.

Doviak, R. J. and D. S. Zrnic, 1993: *Doppler Radar and Weather Observations*. Dover Publications, 562 pp.

Dye, J. E., J. J. Jones, W. P. Winn, T. A. Cerni, B. Gardiner, D. Lamb, R. L. Pitter, J. Hallett, and C. P. R. Saunders, 1986: Early electrification and precipitation development and precipitation development in a small, isolated Montana cumulonimbus. *J. Geophys. Res.,* **91**, 1231-1247.

_____, W. P. Winn, J. J. Jones, and D. W. Breed, 1989: The electrification of New Mexico thunderstorms, 1. Relationship between precipitation development and the onset of electrification. *J. Geophys. Res.*, **94**, 8643-8656.

Edwards, R. and R. L. Thompson, 1998: Nationwide comparison of hail size with WSR-88D vertical integrated liquid water and derived thermodynamic sounding data. *Wea. Forecasting*, **13**, 277 – 285.

Gaskell, W. and A. J. Illingworth, 1980: Charge transfer accompanying individual collisions between ice particles and its role in thunderstorm electrification. *Quart. J. Roy. Meteor. Soc.*, **106**, 841-854.

Gauthier, M. L., W. A. Peterson, L. D. Carey, and H. J. Christian Jr., 2006: Relationship between cloud-to-ground lightning and precipitation ice mass: A radar study over Houston, *Geophys. Res. Lett.*, **33**, L20803, doi:10.1029/2006GL027244.

Gilmore, M. S., J. M. Straka, and E. N. Rasmussen, 2004: Precipitation uncertainty due to variations in precipitation particle parameters within a simple microphysics scheme. *Mon. Wea. Rev.,* **132**, 2610-2627.

Glickman, T. S., Ed., 2000: *Glossary of Meteorology*. 2nd ed. Amer. Meteor. Soc., 855 pp.

Goodman, S. J., D. E. Buechler, P.D. Wright, and W. D. Rust, 1988: Lightning and precipiation history of a microburst-producing storm. *Geophys. Res. Lett.*, **15**, 1185-1188.

Green, D. R. and R.A. Clark, 1972: Vertically integrated water – a new analysis tool. *Mon. Wea. Rev.*, **100**, 548 – 552.

Gremillion, M. S. and R. E. Orville, 1999: Thunderstorm characteristics of cloud-to-ground lightning at the Kennedy Space Center, Florida: A study of lightning initiation signatures as indicated by the WSR-88D. *Wea. and Forecasting*, **14**, 640-649.

Hondl, K. D. and M. D. Eilts, 1994: Doppler radar signatures of developing thunderstorms and their potential to indicate the onset of cloud-to-ground lightning. *Mon. Wea. Rev.*, **122**, 1818-1836.

Jayaratne, E. R., C. P. R. Saunders, and J. Hallett, 1983: Laboratory studies of the charging of soft hail during ice crystal interactions. *Quart. J. Roy. Meteor. Soc.*, **109**, 609-630.

_____, and _____, 1985: Thunderstorm electrification: The effect of cloud droplets. *J. Geophys. Res.*, **90**, 13,063-13,066.

Kalnay, E., M. Kanamitsu, R. Kistler, W. Collins, D. Deavenand et al., 1996: The NCEP/NCAR 40-year reanalysis project. *Bull. Am. Meteorol. Soc.*, **77**, 437-471.

Keith, W. D., and C. P. R. Saunders, 1990: Further laboratory studies of the charging of graupel during ice crystal interactions. *Atmos. Res.*, **25**, 445-464.

Krehbiel, P. R., 1986: The electrical structure of thunderstorms. In *The Earth's Electrical Environment*, eds. E. P. Krider and R. G. Roble, National Academy Press, pp. 90-113.

Krider, E. P., R. C. Noggle, and M. A. Uman, 1976: A gated wideband magnetic direction finder for lightning return strokes. *J. Appl. Meteor.*, **15**, 301-306.

Larsen, H. R., and E. J. Stansbury, 1974: Association of lightning flashes with precipitation cores extending to height 7 km. *J. Atmo. Terr. Phys.*, **36**, 1547-1533.

Liu, C. L. and A. J. Illingworth, 2000: Toward more accurate retrievals of ice water content from radar measurements of clouds. *J. Appl. Meteor.,* **39**, 1130-1146.

MacGorman, D. R., and W. D. Rust, 1998: *The Electrical Nature of Storms*. Oxford University Press, 422 pp.

_____, T. Filiaggi, R. L. Holle, and R. A. Brown, 2007: Negative cloud-to-ground lightning flash rates relative to VIL, maximum reflectivity, cell height, and cell isolation. *J. Lightning Res.,* **1**, 132 – 147.

Marshall, J. S. and W. McK. Palmer, 1948: The distribution of raindrops with size. *J. Atmos. Sci.*, **5**, 165-166.

_____, and S. Radhakant, 1978: Radar precipitation maps as lightning indicators. *J. Appl. Meteor.,* **17**, 206-212.

Marshall, T. C., W. D. Rust,W. P. Winn, and K. E. Gilbert, 1989: Electrical structure in two thunderstorm anvil clouds. *J. Geophys. Res.,* **94**, 22,297-306.

McCaul Jr., E. W., 2008: Use of vertically integrated liquid in WRF-based forecasts of lightning threat. *24th Conference on Severe Local Storms.* Savannah, GA. Amer. Meteor. Soc.

Michimoto, K, 1990: A study of radar echos and their relation to lightning discharge of thunderclouds in the Hokuriku district. Part I: Observations and analysis of thunderclouds in summer and winter. *J. Meteor. Soc. Japan*, **69**, 327-335.

Mohr, C. G., L. J. Miller, R. L. Vaughn, and H. W. Frank, 1986: On the merger of mesoscale data sets into a common Cartesian format for efficient and systematic analysis. *J. Atmos. Oceanic Technol.*, **3**, 143 – 161.

Motley, S. M., 2006: Total lightning characteristics of ordinary convection. M.S. thesis, Texas A&M University, 165 pp.

NOAA/ERSL Radiosonde Database Access. U.S Department of Commerce, National Oceanic and Atmospheric Administration, Earth Sytem Research Laborotory, Boulder, Co; [updated 2009 Feb 11; cited 2009 Jun 15]. Available from: http://raob.fsl.noaa.gov/.

OFMC, 2006: *Federal Meteorological Handbook No. 11 Doppler Radar Meteorological Observations Part C: WSR-88D Products and Algorithms.* FCM-H11C-2006, 390 pp. [Available from Office of Federal Coordinator for Meteorology.]

OFCM, 2008: *Federal Meteorological Handbook No. 11 Doppler Radar Meteorological Observations Part A: System Concepts, Responsibilities, and Procedures*. FCM-H11A-2008, 53 pp. [Available from Office of Federal Coordinator for Meteorology.]

Orville, R. E., and G. R. Huffines, 2001: Cloud-to-ground lightning in the United States: NLDN results in the first decade, 1989-98. *Mon. Wea. Rev.*, **129**, 1179-1193.

_____, _____, J. Nielsen-Gammon, R. Zhang, B. Ely, S. Steiger, S. Phillips, S. Allen, and W. Read, 2001: Enhancement of cloud-to-ground lightning over Houston, Texas. *Geophys. Res. Lett*., **28**, No. 13, 2597-2600.

_____., 2008: Development of the National Lightning Detection Network. *Bull. Amer. Meteor. Soc.*, **89**, 180 – 190.

Oye, D., M. Cases, 1995: *REORDER: A Program for Gridding Radar Data. Installation and Use Manual for the UNIX Version*. NCAR Atmospheric Technology Division, Boulder CO, 19pp.

Peterson, W. A., and S. A. Rutledge, 2001: Regional variability in tropical convection: Observations from TRMM. *J. Climate,* **14**, 3566-3586.

_____, H. J. Christian, and S. A. Rutledge, 2005: TRMM observations of the global relationship between ice water content and lightning. *Geophys. Res. Lett.,* **32**, L14819, doi:10.1029/2005GL023236.

Pruppacher, H. R., and J. D. Klett, 1997: *Microphysics of Clouds and Precipitation*. 2nd rev. and enl. ed. Atmospheric and Oceanographic Sciences Library; v. 18, Kluwer Academic Publishers, 954 p.

Radar Resources [Internet]. Ashville, NC: National Climatic Data Center; [updated 2009 Jan 29; cited 2009 May 23]. Available from: http://www.ncdc.noaa.gov/oa/radar/radarresources.html

Rakov, V. A., and M. A. Uman, 2006: *Lightning: Physics and Effects.* 3rd ed. Cambridge University Press, 679 pp.

Reynolds, S. E., M. Brook, and M. F. Gourley, 1957: Thunderstorm charge separation. *J. Meteor.*, **14**, 426-436.

_____, and _____, 1956: Correlation of the initial electric fields and the radar echo in thunderstorms. *J. Meteor.*, **13**, 376-380.

Rinehart, R. E., 2004: *Radar for Meteorologists*. 4th ed. Rinehart Publications. 482 p.

Sassen, K., 1987: Ice cloud content from radar reflectivity. *J. Appl. Meteor.*, **26**, 1050-1053.

Saunders, C. P. R., W. D. Keith, and R. P. Mitzeva, 1991: The effect of high liquid water content on thunderstorm charging. *J. Geophys. Res.*, **96**, 11,007-11,017.

_____, and I. M. Brooks, 1992: The effect of high liquid water content on thunderstorm charging. *J. Geophys. Res.*, **97**, 14,671-14,676.

Shackford, C. R., 1960: Radar indications of a precipitation-lightning relationship in New England thunderstorms. *J. Atmos. Sci.*, **17**, 15-19.

Simpson, G. and F. J. Scrase,1937: The distribution of electricity in thunderclouds. *Proc. Roy. Soc. London A*, **161**, 309-352.

_____, and G. D. Robinson, 1941: The distribution of electricity in thunderclouds. *Proc. Roy. Soc. London A*, **171**, 281-329.

Takahashi, T., 1978: Riming electrification as a charge generation mechanism in thunderstorms. *J. Atmos. Sci.*, **35**, 1536-1548.

Uman, M. A., 1986: *All About Lightning*. General Publishing Company. 192 pp.

_____, M. A., 1987: *The Lightning Discharge*. International Geophysics Series, Vol. 39, Academic Press, 377 pp.

Vincent, B. R., L. D. Carey, D. Schneider, K. Keeter, and R. Gonski, 2004: Using WSR-88D reflectivity for the prediction of cloud-to-ground lightning: A Central North Carolina study. *Natl. Wea. Dig.*, **27**, 35 – 44.

Wallace, J. M. and P. V. Hobbs, 2006: *Atmospheric Science*. 2nd Edition. Academic Press, 483 pp.

Watson, A. I., R. L. Holle, and R. E. Lopez, 1995: Lightning from two national detection networks related to vertically integrated liquid and echo-top information from WSR-88D radar. *Wea. Forecasting*, **10**, 592 – 605.

Williams, 2001: The electrification of severe storms. *Severe Convective Storms, Meteor. Monogr.*, No. 50, Amer. Meteor. Soc., 527-561.

Wilson, C. T. R., 1916: On some determinations of the sign and magnitude of electric discharges in lightning flashes. *Proceedings of the R. Soc. London, Ser A.*, **92**, 555-574.

_____, 1920: Investigations on lightning discharges and on the electric field of the Earth, *Philos. Trans. R. Soc. London, Ser. A*, **221**, 73-115.

_____, 1929: Some thundercloud problems, *J.Franklin Inst.,* **208**, 1-12.

Wolf, P., 2006: Anticipating the initiation, cessation, and frequency of cloud-to-ground lightning, utilizing WSR-88D reflectivity data. *NWA Electronic Journal of Operational Meteorology*, December 2006.

Workman, E. J., and S.E. Reynolds, 1949: Electrical activity as related to thunderstorm cell growth. *Physical Review,* **74**, 1231-1232.

Wormell, T. W., 1930: Vertical electric currents below thunderstorms and showers. *Proc. Roy. Soc. A*, **127**, 567-590

_____, 1939: The effect of thunderstorms and lightning discharges on the Earth's electric field. *Phil. Trans. Roy. Soc. A*, **328**, 249-303.

Yeung, L. H. Y., E. S. T. Lai, and S. K. S. Chiu, 2007: Lightning initiation and intensity nowcasting based on isothermal radar reflectivity – A conceptual model. *33rd International Conference on Radar Meterology*, Cairns, Australia, Amer. Meteor. Soc.

Ziegler, C. L. and D. R. MacGorman, 1994: Observed lightning morphology relative to modeled space charge and electric field distributions in a tornadic storm. *J. Atmos. Sci.*, **51**, 833-851.

APPENDIX A

A – Vertical Resolution of CAPPI Data

The volume scan strategy and distance from the radar determine the maximum vertical resolution to which polar radar data can be interpolated without introducing artifacts (as would be the case with too fine a vertical resolution) or sacrificing data (as would be the case with too coarse a vertical resolution). Radar data is often interpolated to a 1 km vertical resolution, which is a reasonable choice when considering a reasonably dense volume scan strategy (such as VCP 11) and observations out to 150 km from the radar (i.e., you lose some data close to the radar and are potentially over resolving echo features 150 km away from the radar, but the bulk of the radar observations are well resolved with 1 km vertical resolution). However, this study is heavily dependent on high resolution reflectivity observations in the vertical, so as already discussed in Section 2.1.3.1, August 2006 forecast statistics using vertical resolutions of 0.5 km and 1 km were compared to determine if a 1 km vertical resolution is sufficient to calculate robust radar forecast statistics or if a finer resolution should be used.

A.1 – Cell Identification Comparison

Using radar data interpolated to 0.5 km vertical resolution, the CAPPI-SCIT algorithm identified significantly more cells than using 1 km vertical resolution, especially cells with a track count of 0 (cf. Tables A.5-8 and Tables A.1-4). For example, 2351 cells met the 30 dBZ at E10 within 150 km criteria for 1.0 km, while 4110 cells met the same criteria for 0.5 km. Since vertical association is required for a cell to be identified, an increase in the vertical resolution will increase the likelihood that a cell is

represented at different levels. Recall that vertical association only needs to be two consecutive height levels. Therefore, the CAPPI-SCIT algorithm used on the 0.5 km resolution data will identify cells with a minimum depth of 1 km, while the algorithm run on data with a 1 km resolution will identify cells with a minimum depth of 2 km. As a result, the 0.5 km resolution produces almost double the amount of cells that are identified for only one volume scan. However, the difference in the number of cells tracked for more than one volume scan decreases significantly the longer a cell is tracked. This suggests that the cells identified using the increased vertical resolution are weak and/or small in vertical extent.

The CAPPI-SCIT algorithm produced more cells for the 0.5 km vertical resolution except when the cell was within 100 or 75 km and tracked for at least 1 or 2 scans. For these cases, it appears that the increased resolution reduced interpolation issues and allowed the data to be more accurately represented. The raw radar data will have better horizontal and vertical resolution closer to the radar. If this data is interpolated over a large distance, it has the potential of making storms larger than they actually were. Since the horizontal resolution is the same for each case, the interpolated 1 km resolution data will have a greater potential to create larger storms, which was an initial reservation of using the 1 km resolution data. However, it appears that this was only the case within 100 km of the radar.

A.2 – Comparison of POD Statistics

Interestingly, the forecast statistics (Tables A.1-8) favored the 1.0 km vertical resolution in many of the predictor combinations. Figure A.1 illustrates the POD

comparison (i.e., $POD_{1.0km}$ - $POD_{0.5k\ m}$). $POD_{1.0km}$ was greater (and thus better) in almost all cases except at E10 within 150 km of the radar and other isolated 40 dBZ at E10 combinations. This is probably a result of the interpolation creating storms with greater vertical extent. As a result, the interpolation is allowing the forecast criteria to be met for the data with the 1.0 km resolution while the 0.5 km resolution data remain below the desired levels. However, if the data interpolated to 1.0 km is creating too many artifacts, an increase in the FAR will result. If FAR is increases as POD increases, no forecast skill is gained.

A.3 – Comparison of FAR Statistics

Figure A.2 shows mixed results when comparing $FAR_{1.0m}$ and $FAR_{0.5km}$. At E10, $FAR_{1.0km}$ is generally less than $FAR_{0.5km}$ indicating better false alarm rates for the 1.0 resolution, especially when a cell has a track count of 0. The average $FAR_{1.0km}$ at E10 is 0.43, while the average $FAR_{0.5km}$ is 0.48. If the cases when the cell is only identified for one scan are omitted, the $FAR_{1.0km}$ becomes 0.39 and $FAR_{0.5km}$ becomes 0.41, thus indicating little difference between vertical resolution choices.

Increased vertical resolution benefits FAR at E15 most (i.e., $FAR_{0.5km}$ is generally less than $FAR_{1.0km}$). This could be a result of interpolation but most likely results from the additional comparison levels available for the 0.5 km data. For example, if the -15 °C level was at 7.6 km (a reasonable climatological value for Houston in the summer), analysis based on the 1.0 km vertical resolution data would have to use the reflectivity values at 8.0 km since no closer heights are available. However, analysis based on the 0.5 km vertical resolution data could use the reflectivity values at 7.5 km. This lack of

comparable levels was one of the main reasons an additional vertical resolution was considered. It appears that this lack of comparison levels had the greatest influence on the environmental -15 °C level statistics because E10 and E20 round more closely to climatological values of 7 and 8 km, respectively.

$FAR_{1.0km}$ - $FAR_{0.5km}$ values at E20 and U10 are consistently negative for cells identified only once, similar to the previous two environmental levels. This is likely a result of the high number of cells detected by the CAPPI-SCIT algorithm when using the data with 0.5 km vertical resolution. Excluding cases when a cell was only identified once, the 0.5 km dataset generally has lower false alarm rates, providing the largest improvement at ranges less than 100 km.

A.4 – Comparison of CSI Statistics

Figure A.3 shows that $CSI_{1.0km}$ - $CSI_{0.5km}$ values generally favor the 1.0 km resolution dataset. At E10, $CSI_{1.0km}$ is about 0.1 greater than $CSI_{0.5km}$ when a cell is only identified for one scan, but the difference is close to zero when cells are tracked at least once. $CSI_{1.0km}$ - $CSI_{0.5km}$ values are more variable at E15 and U10, although the use of 40 dBZ strongly favors the 1.0 km resolution dataset at both environmental levels. $CSI_{1.0km}$ shows the most consistent improvement over $CSI_{0.5km}$ at E20, with most differences ranging from 0.05-0.15.

A.5 – Comparison of Forecast Lead Times

The forecast lead times show trends similar to CSI. The longest lead times were found using the 1.0 km vertical resolution dataset for all predictor combinations except

40 dBZ at E10. The largest difference in lead times was observed at E15. As discussed in Section A.3, the environmental -15 °C level is commonly near 7.5 km. The 1.0 km dataset has to use values that are at greater distances from the actual height compared to the 0.5 km dataset. Consider an example case when the environmental -15 °C level is at 7.4 km. The 1.0 km resolution dataset compares its closest reflectivity value, which is at 7.0 km, while the 0.5 km resolution dataset compares its closest reflectivity value, which is at 7.5 km. The chances of a forecast being correct at the 7.0 km level are higher and therefore the forecast is made sooner. The case could also be the opposite. For example, if the environmental -15 °C level is at 7.6 km, as in the example used in Section A.3, the 1.0 km resolution dataset would have to compare at 8.0 km. This case would lead to a decreased lead time for the 1.0 km resolution dataset. However, the data suggest that the first example is true more often. The KHGX sounding average heights for August 2006 for the environmental -10, -15, and -20 °C levels were 6.6, 7.4, and 8.1 km, respectively. The best average lead time of 15.8 min was found using 1.0 km resolution dataset and 30 dBZ at E10. If the cases with only scan can are excluded, the forecast lead time increases to 17.0 min. For the 0.5 km resolution dataset and the same predictor combinations, the average forecast lead times were 15.5 and 17.0 min.

A.6 – Conclusions Regarding Vertical Resolution

Based on the above comparisons, it was determined that using the 1.0 km vertical resolution dataset is the best choice for producing KHGX radar-derived lightning forecasts. The forecast statistics favored the 1.0 km resolution dataset for most predictor combinations. While the 0.5 km resolution dataset identified more cells, the additional

cells identified were usually weak and/or small. In addition, the dataset is identical to the dataset used by Gauthier et al. (2006), with the addition of three more years (2004 - 2006), thus facilitating comparison of results.

APPENDIX B

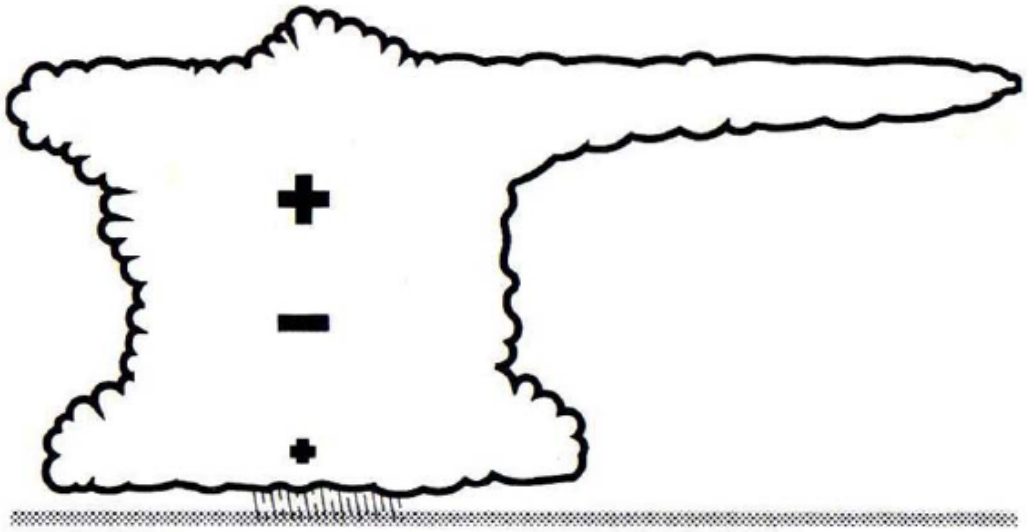

Figure 1.1. Dipole/tripole structure of a thunderstorm with an upper and level positive (+) charge regions and a main negative (-) charge region (from MacGorman and Rust 1998).

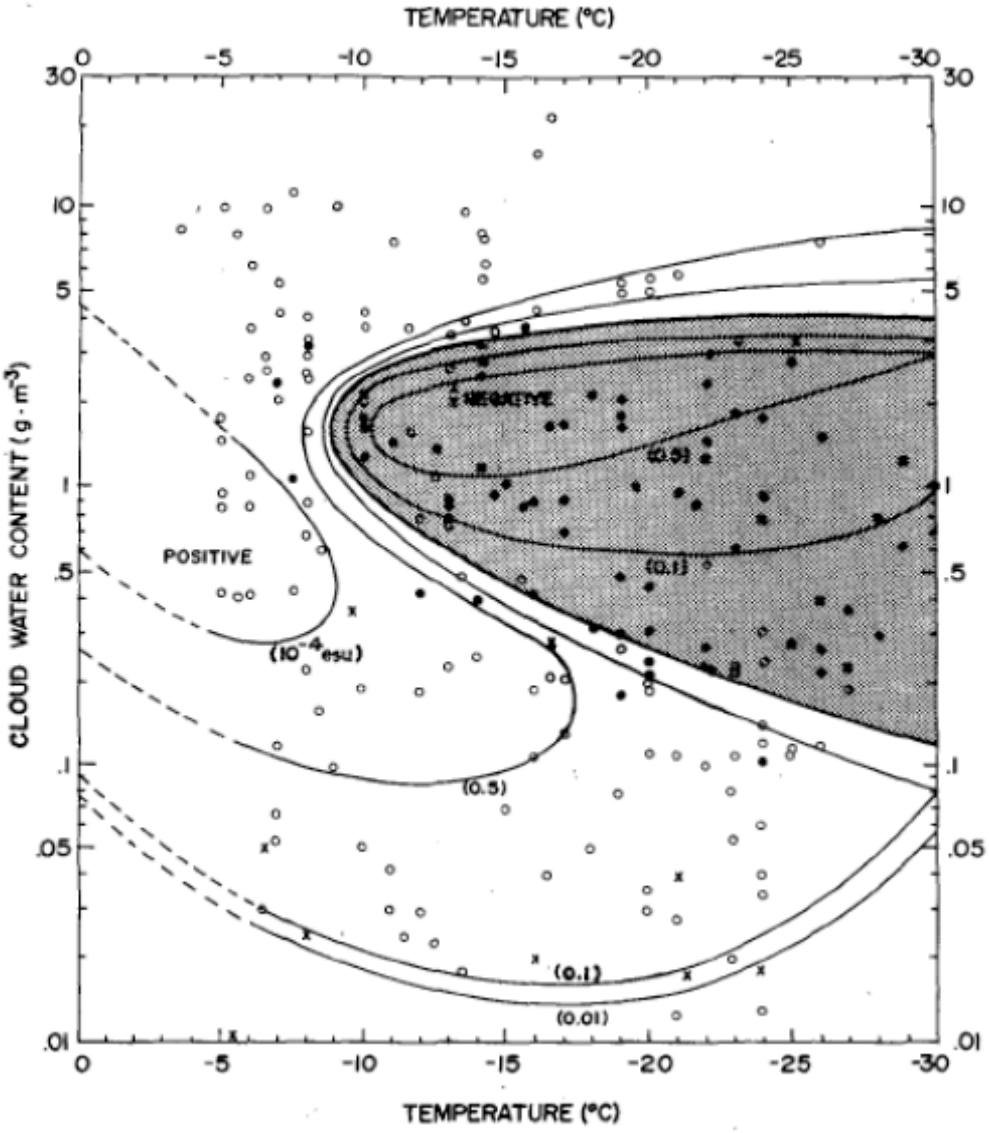

Figure 1.2. Open circles represent a positive charge, solid circles negative charge, and crosses represent uncharged cases (from Takahashi 1978).

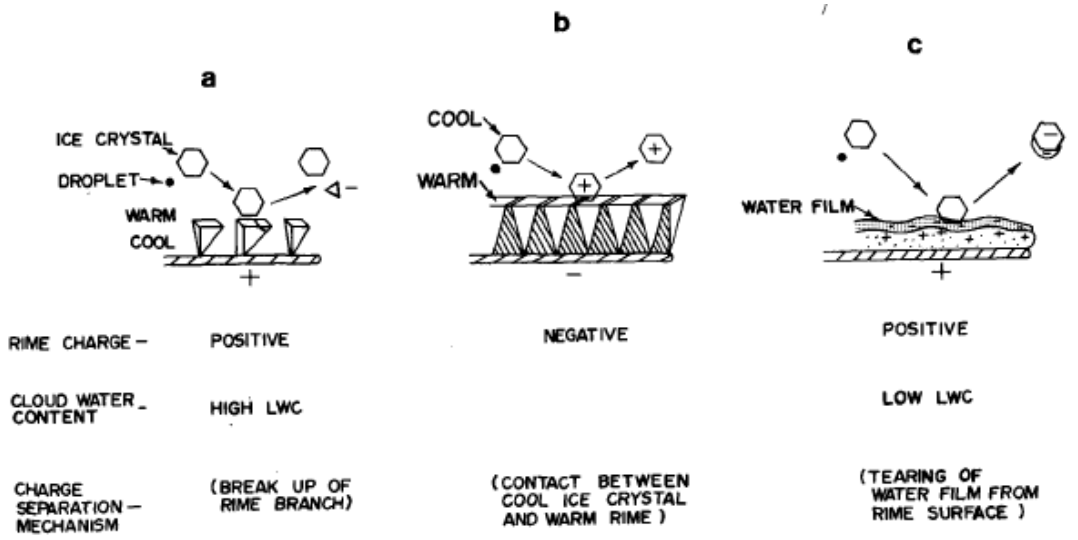

Figure 1.3. Proposed methods of charge separation: (a) positive rime electrification by the breaking of riming branches, (b) negative rime electrification by ice crystal contact and break at the riming surface, and (c) positive rime electrification cause by an ice crystal tearing the water film from rim surface (from Takahashi 1978).

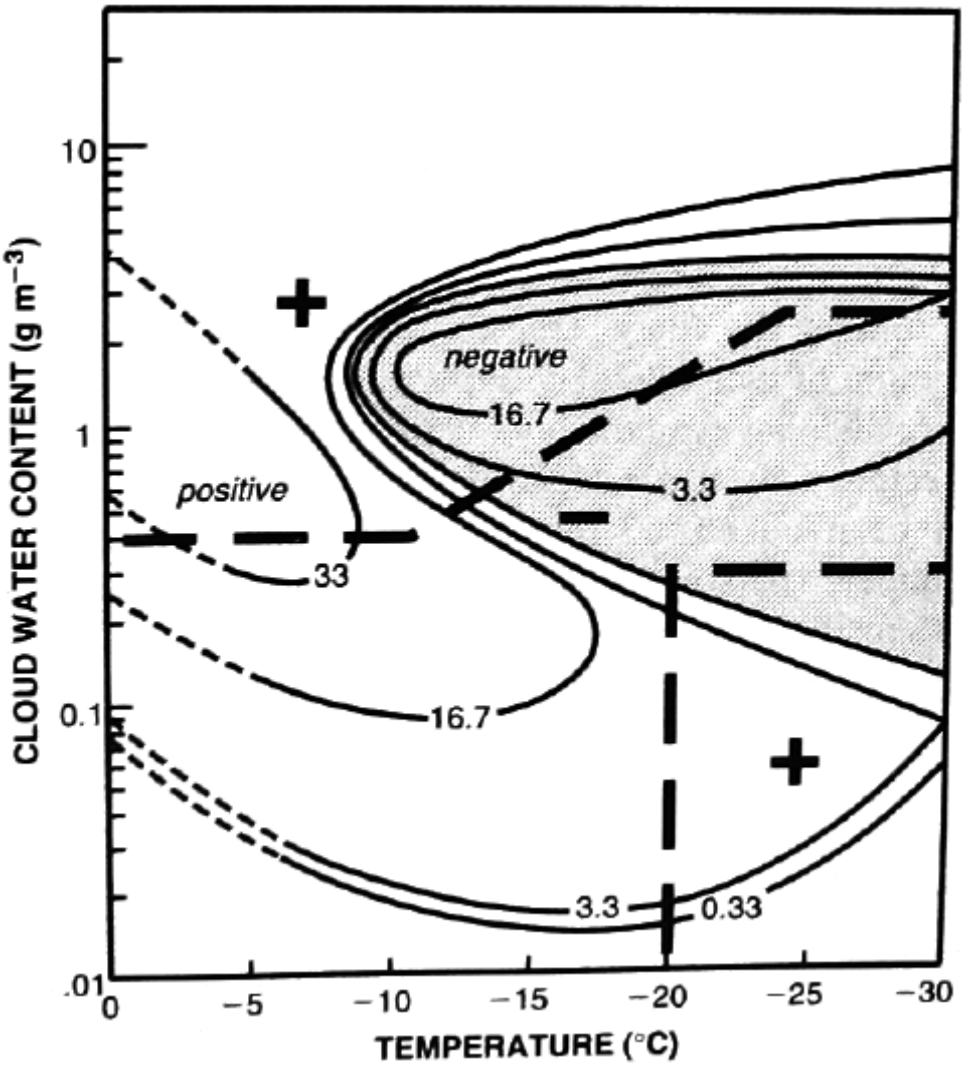

Figure 1.4. The polarity of charged gained by graupel as a function of temperature and liquid water content (LWC) for the experiments of Takahashi (1978) and Saunders et al. (1991). The bold dashed lines separate the values of temperature and CWC at which the charge on graupel changed polarity as measured by Saunders et al. Curved lines show the charged gained (in fC) by graupel as a function of LWC and temperature by Takahashi (1978). (From MacGorman and Rust 1998, p.67).

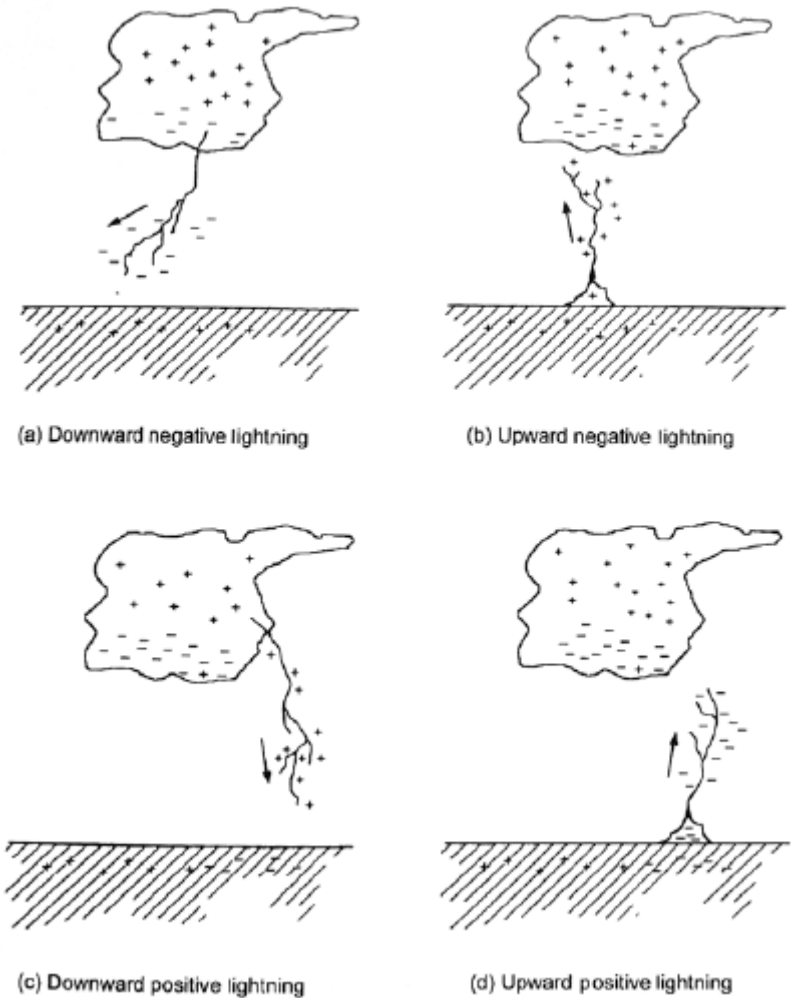

Fig. 1.5. Four types of lightning effectively transferring cloud charge to ground. Only the initial leader is shown for each type. The direction of propagation and polarity of cloud charge effectively lowered to ground is indicated (from Rakov and Uman 2006, p.5).

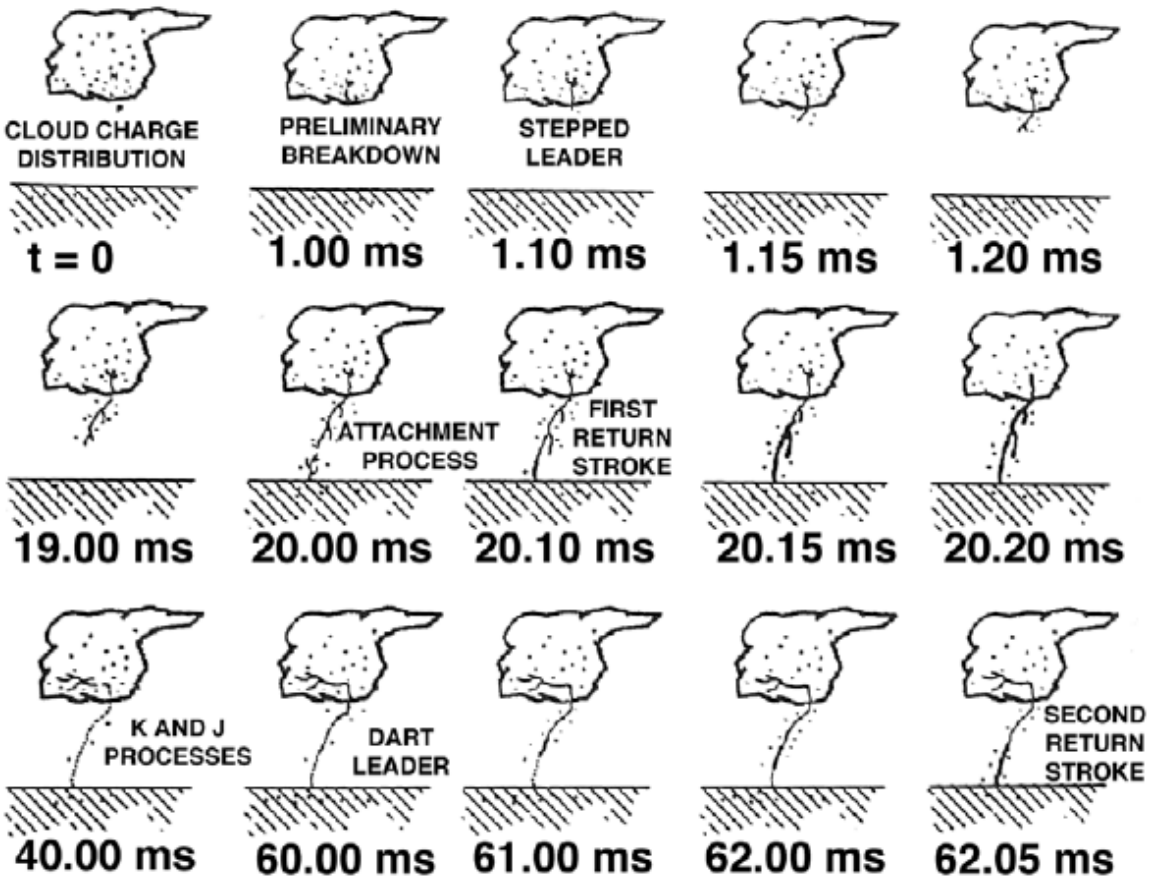

Figure 1.6. Illustration of the processes involved in a typical cloud-to-ground lightning strike (from Uman 1987).

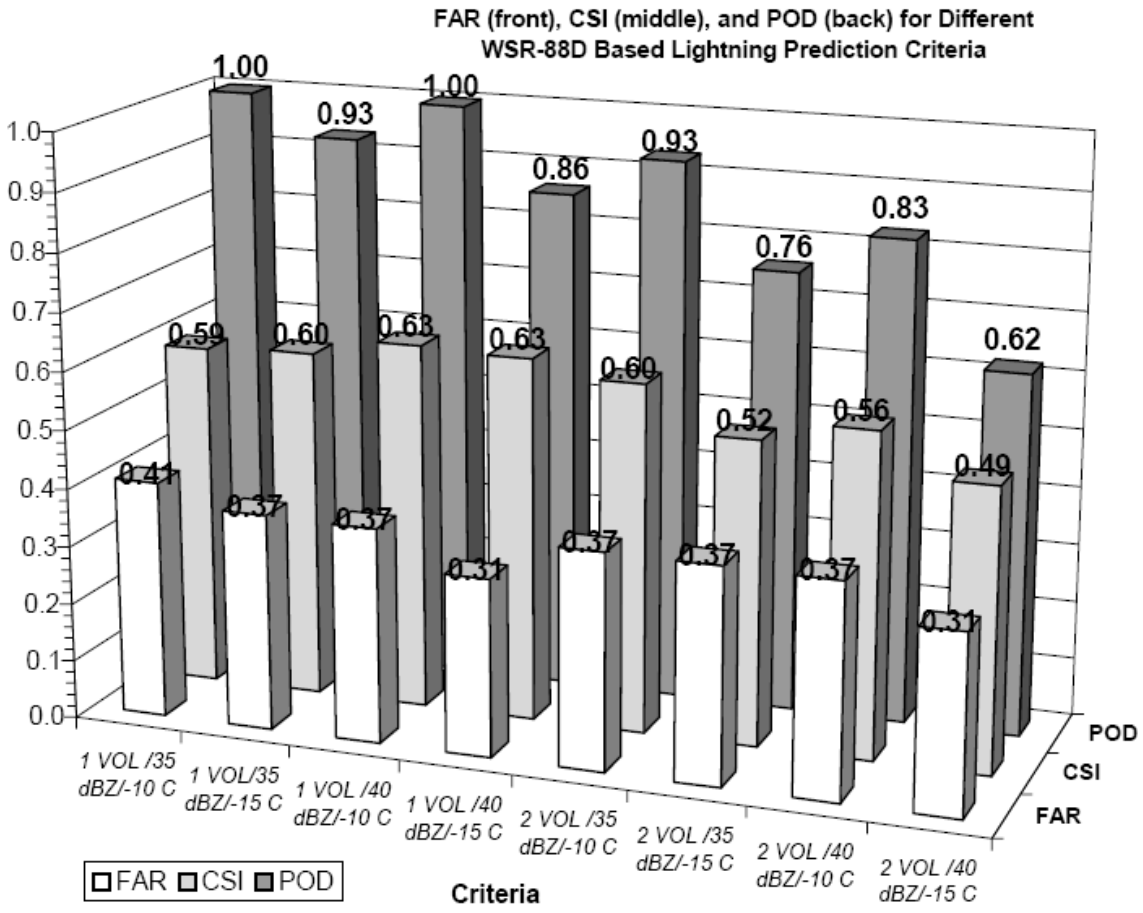

Figure 1.7. FAR, CSI, and POD for different lightning prediction criteria (from Vincent et al. 2003).

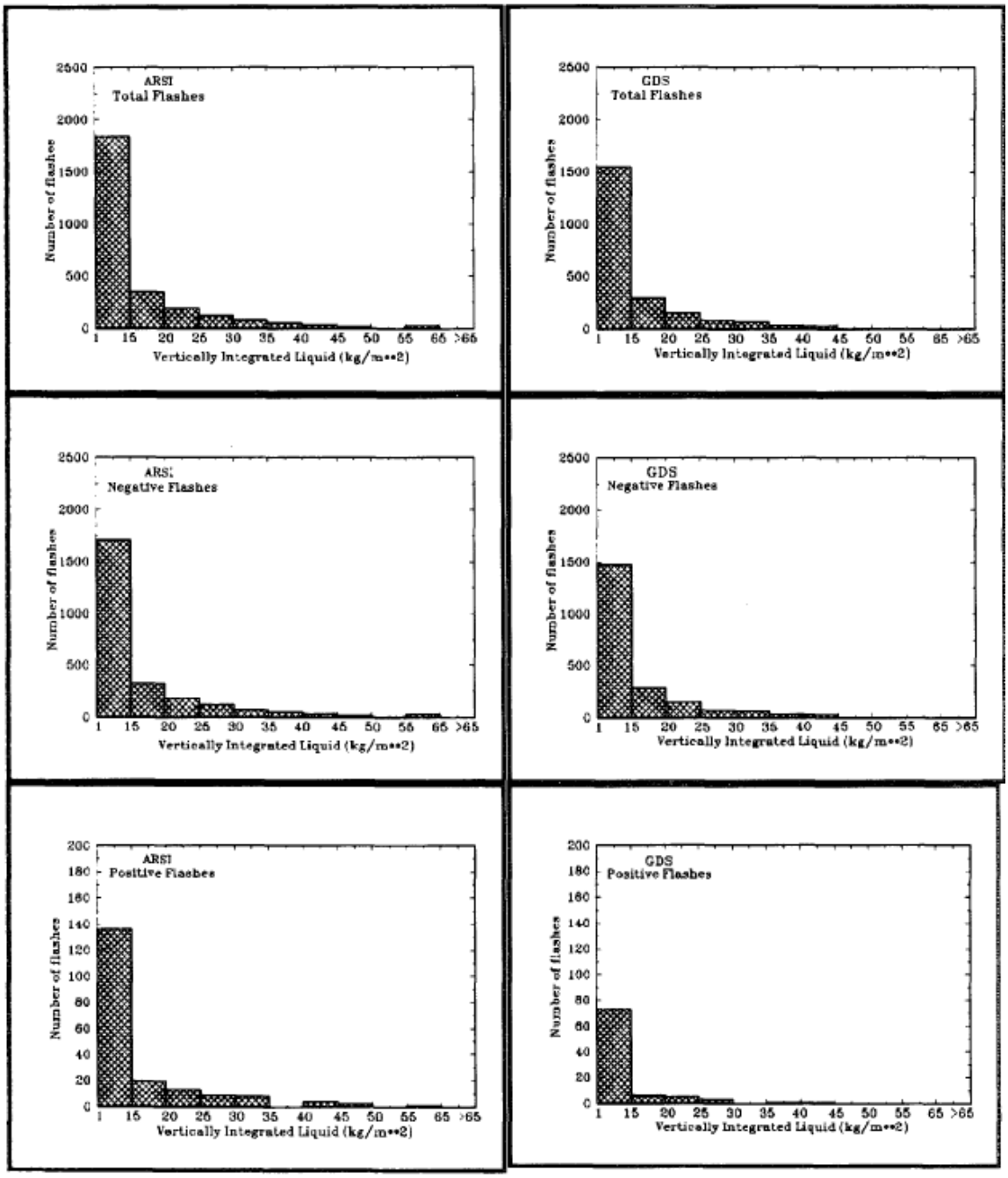

Figure 1.8. Number of flashes from two different lightning detection networks compared to vertically integrated liquid for storms on 9 June 1993: all flashes (top), negative flashes (middle), and positive flashes (bottom; from Watson et al. 1995).

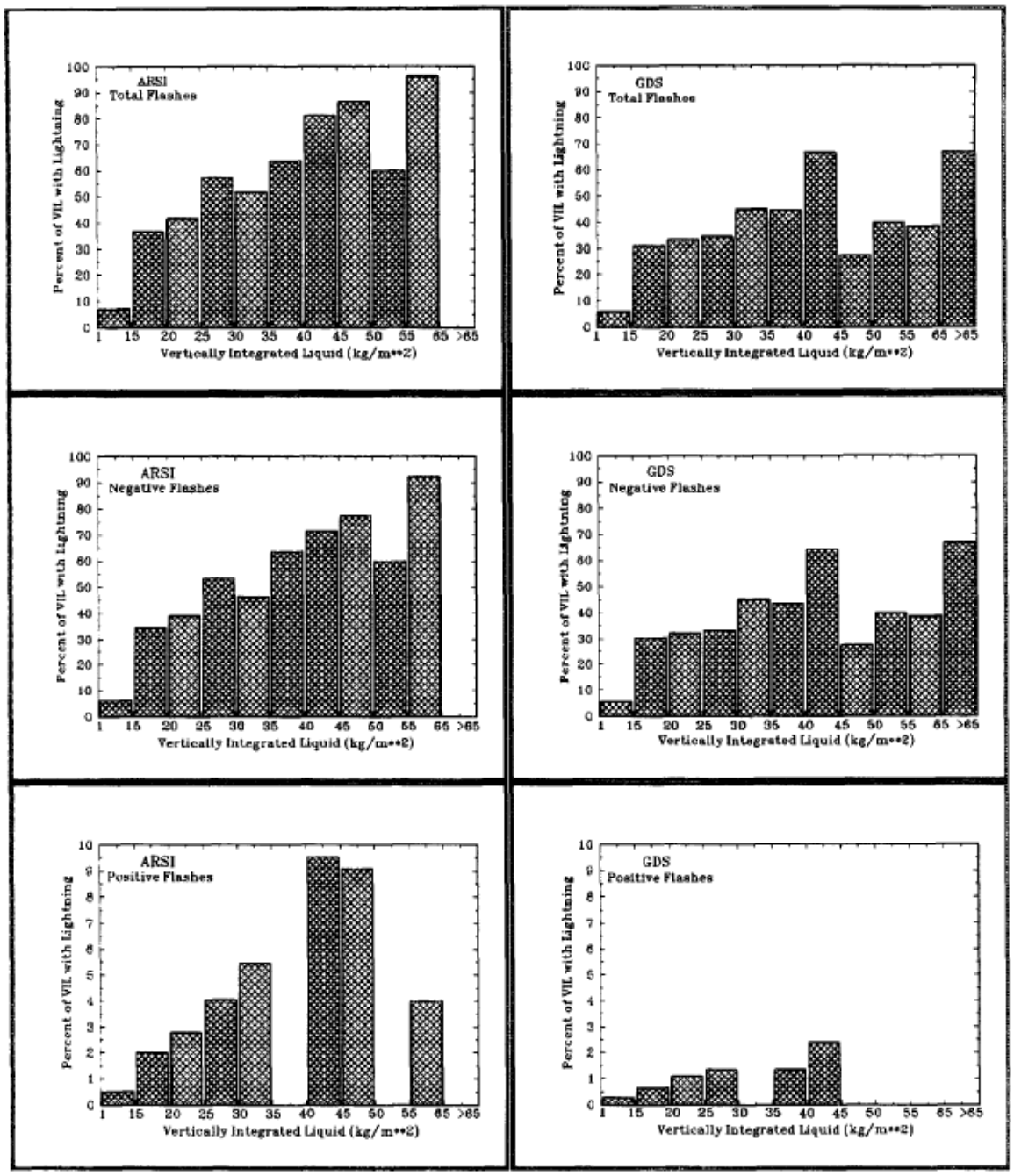

Figure 1.9. Percentage of vertically integrated liquid value with CG lightning flashes from two different lightning detection networks from storms on 9 June 1993: all flashes (top), negative flashes (middle), and positive flashes (bottom; from Watson et al. 1995).

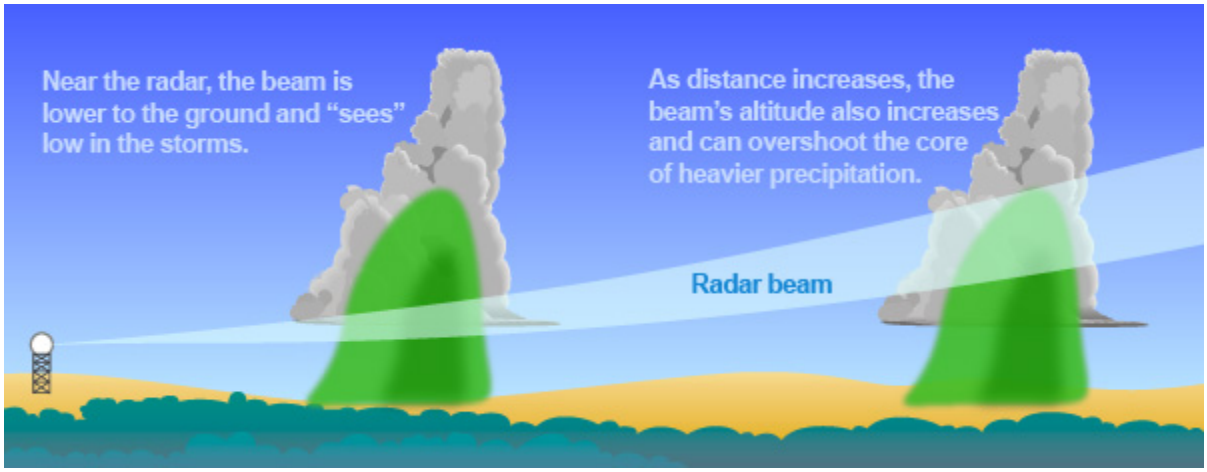

Figure 2.1. Illustration of how a radar beam increases with height as the distance increases (from http://www.srh.noaa.gov/srh/jetstream/doppler/baserefl.htm).

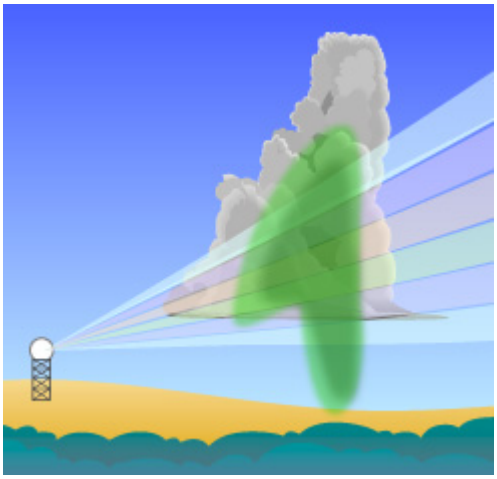

Figure 2.2. Illustrations showing how a scan strategy samples a storm (from http://www.srh.noaa.gov/srh/jetstream/doppler/comprefl.htm).

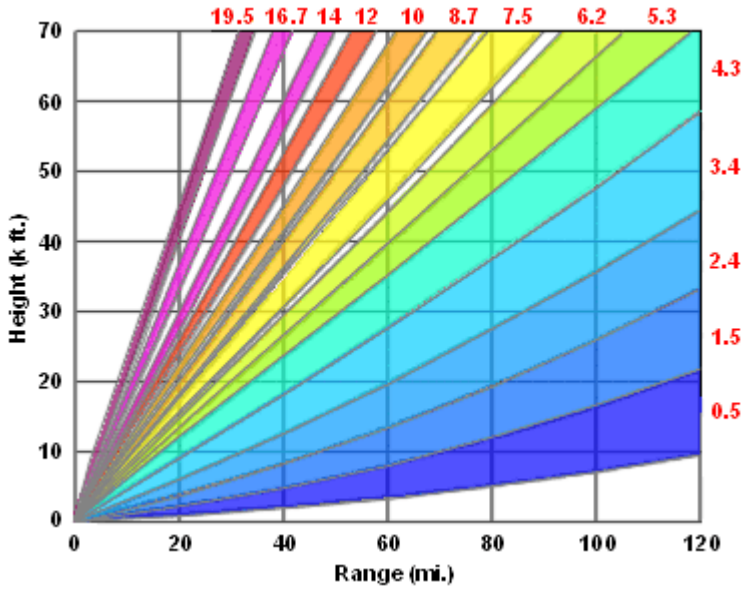

Figure 2.3. Graphical representation of VCP – 11. The numbers along the top and right axes represent the elevation angle (from Radar Resources 2009).

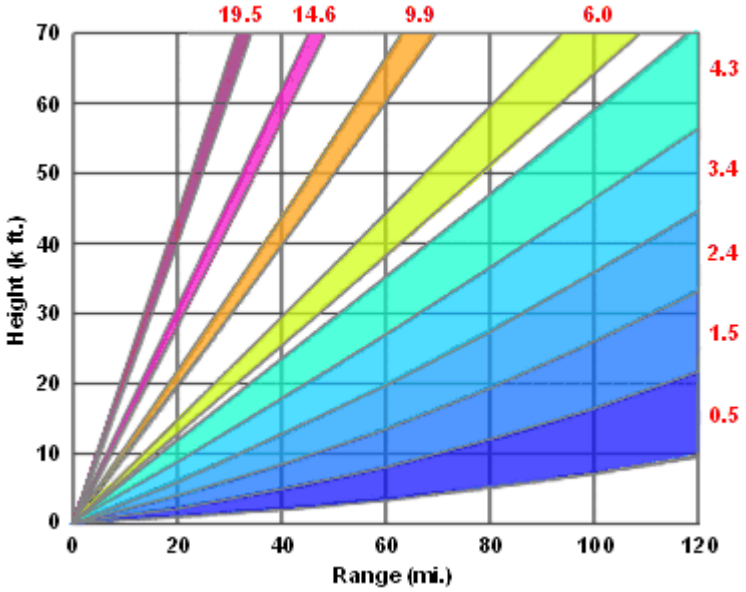

Figure 2.4. Graphical representation of VCP – 21. The numbers along the top and right axes represent the elevation angle (from Radar Resources 2009).

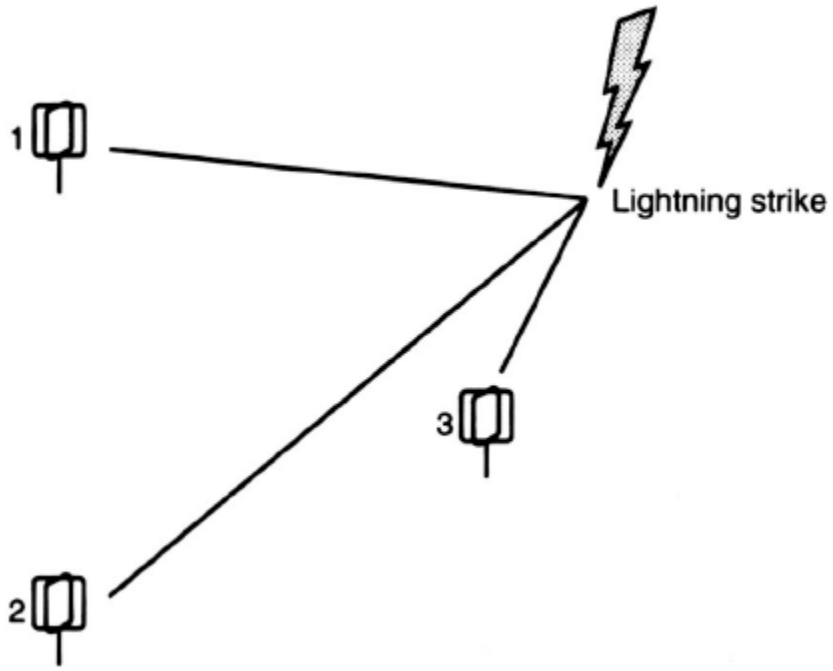

Figure 2.5. Method of determining the location of lightning strike using the magnetic direction finding lightning locating system (from MacGorman and Rust 1998).

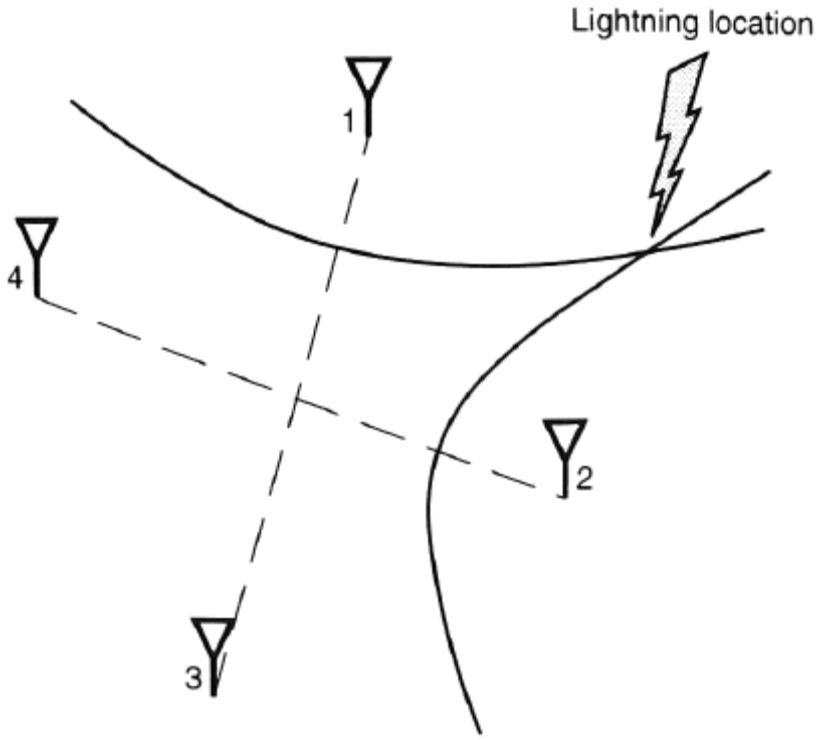

Figure 2.6. Method of determining the location of a lightning strike using the time-of-arrival lightning locating system (from MacGorman and Rust 1998).

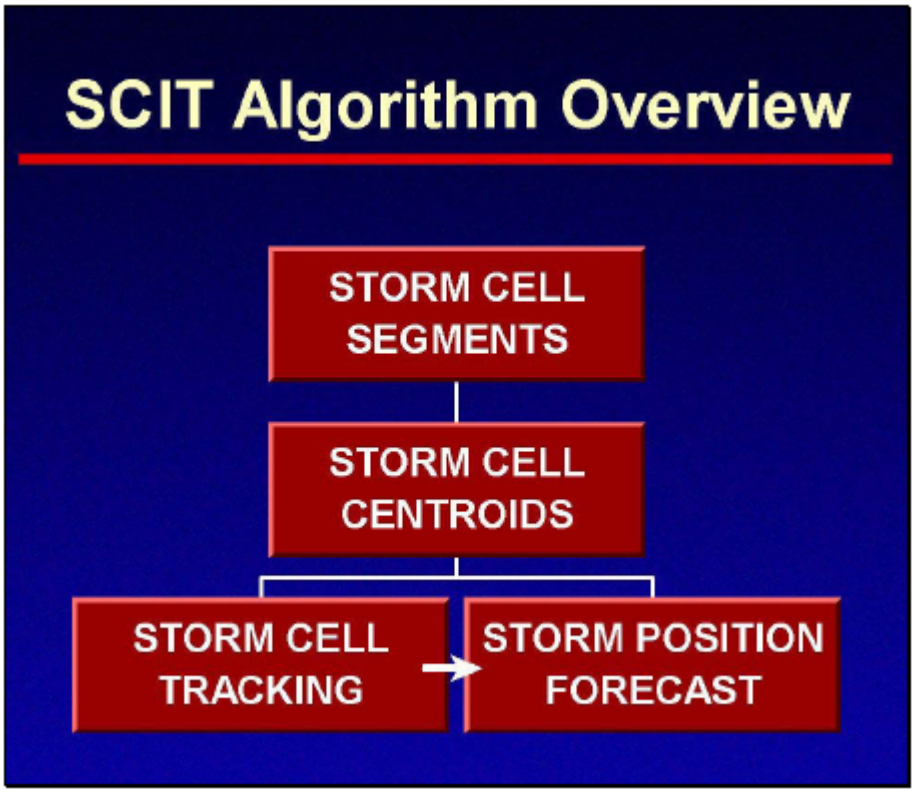

Figure 2.7. Storm Cell Identification and Tracking (SCIT) algorithm overview (from OFCM 2006).

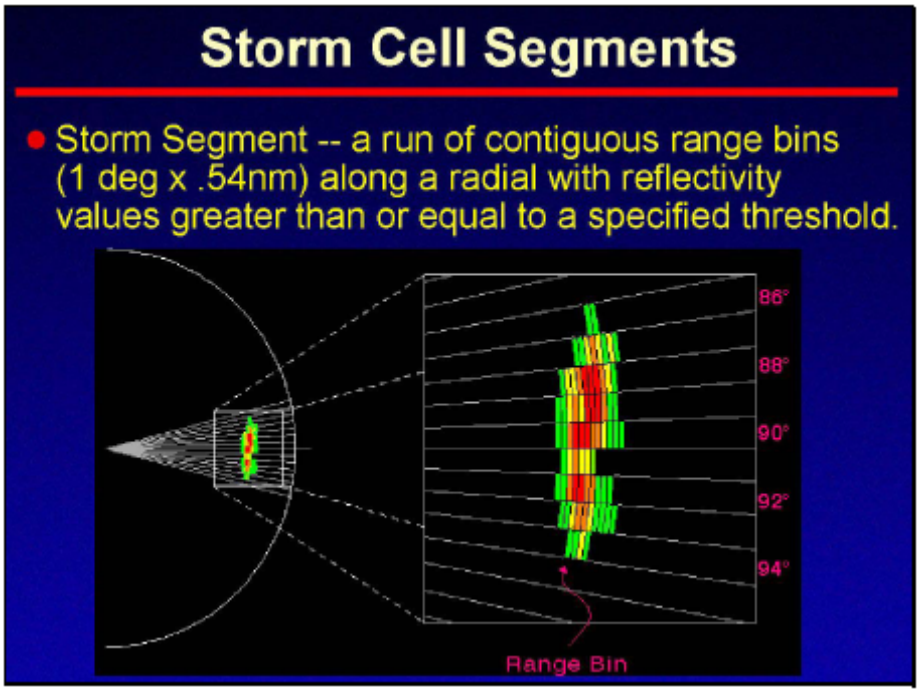

Figure 2.8. Example of storm segments as identified by the SCIT algorithm (from OFCM 2006).

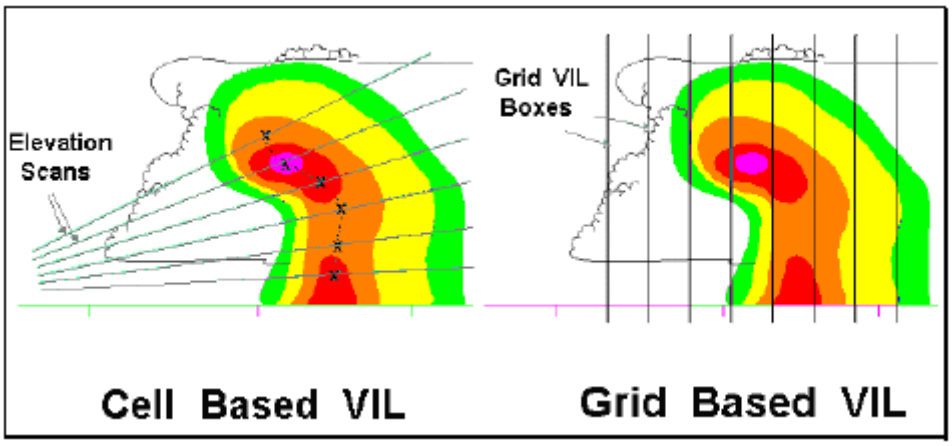

Figure 2.9. Illustration of the differences between a cell-based VIL and a grid-based VIL (from OFCM 2006).

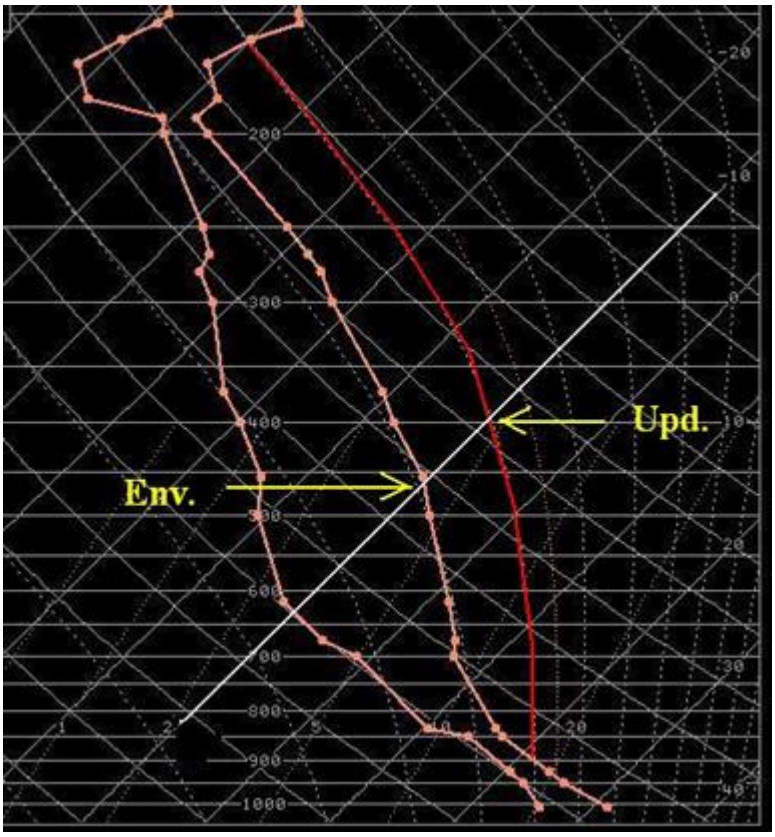

Figure 2.10. Illustration of the difference in the environmental temperature and the updraft temperature (from Wolf 2006).

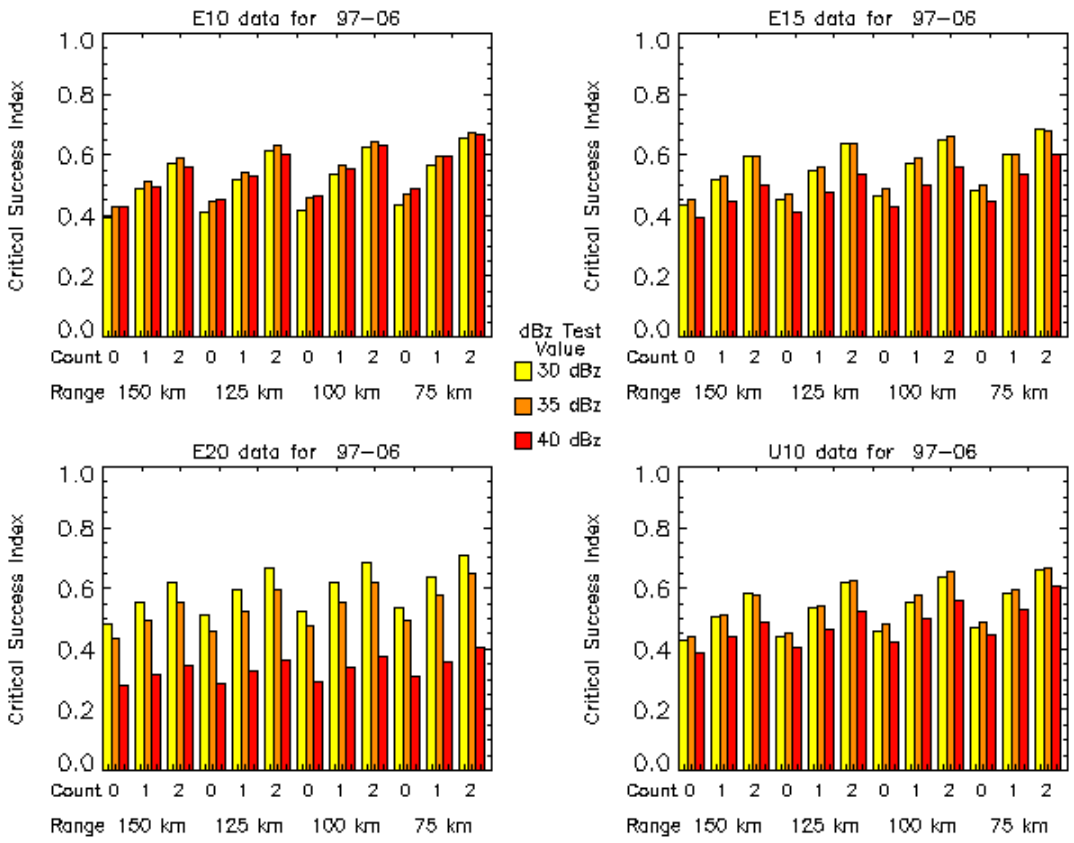

Figure 3.1. CSI values as a result of the analysis of the entire dataset, from 1997 through 2006. Count represents the minimum number of times a cell must be tracked to be considered. Range represents the range a cell must be within to be considered.

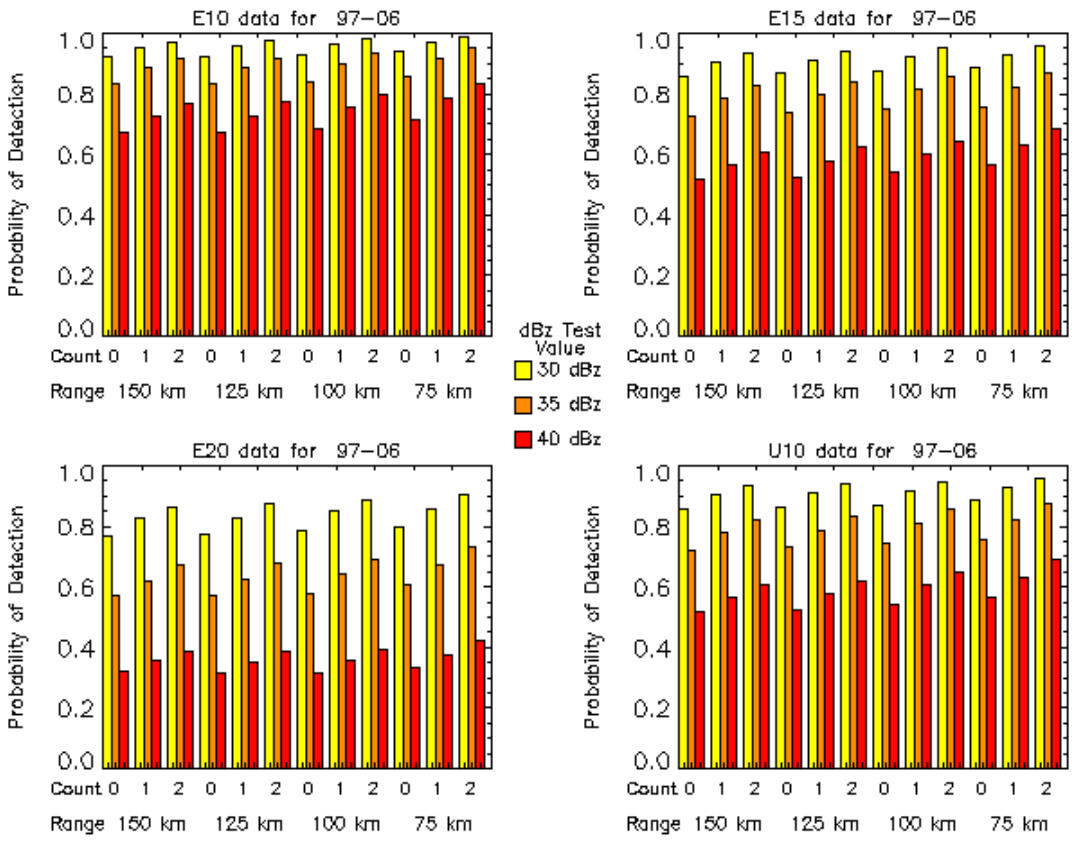

Figure 3.2. Same as Figure 3.1 for the POD values.

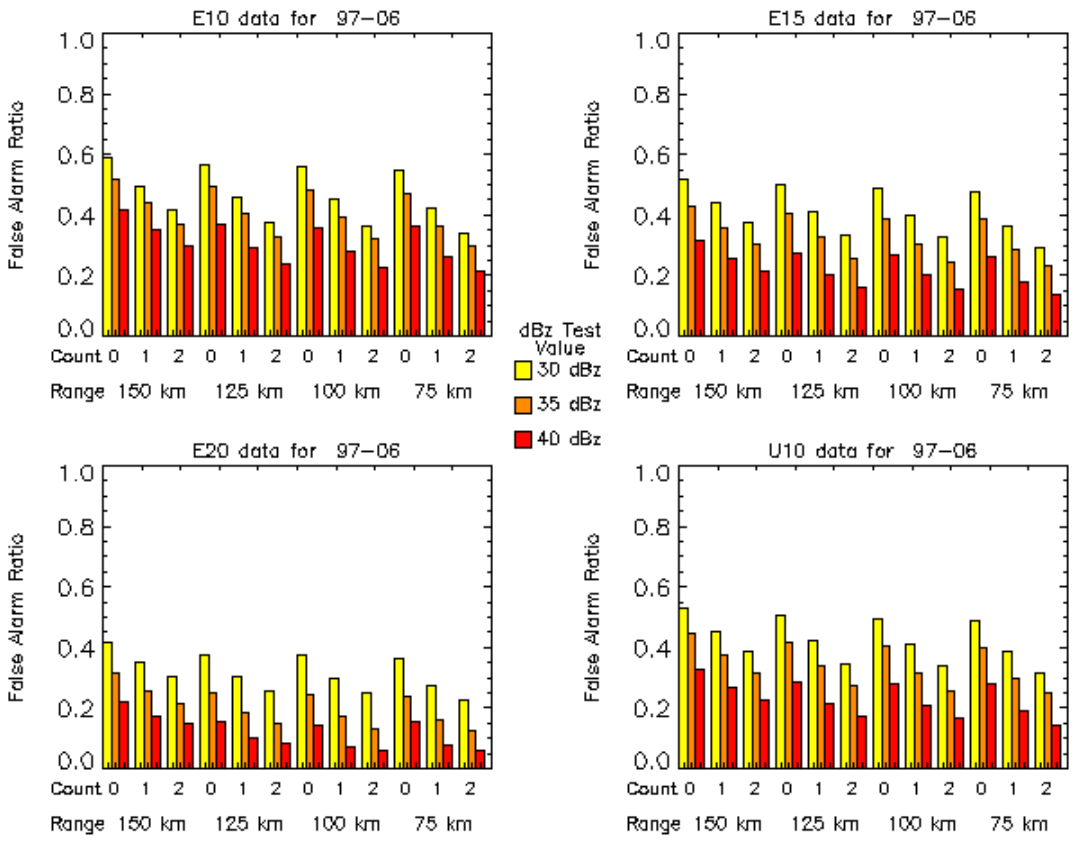

Figure 3.3. Same as Figure 3.1 for the FAR values.

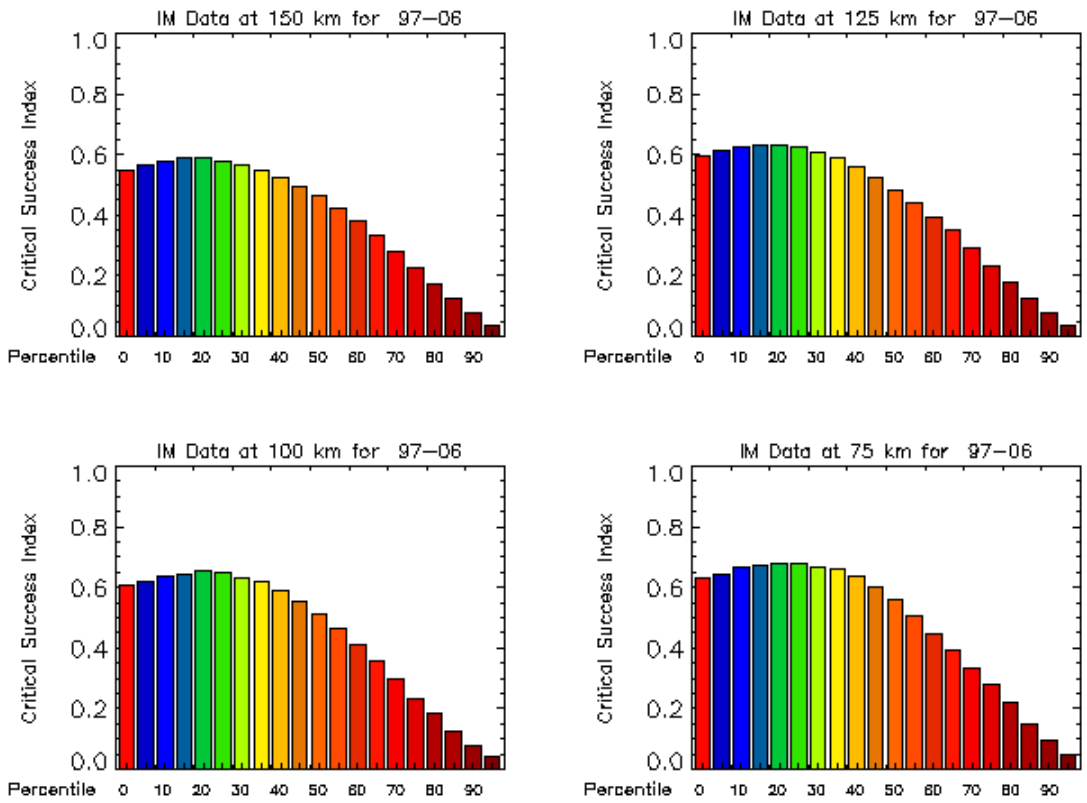

Figure 3.4. CSI values using the vertically integrated ice (VII) percentile values for the entire dataset (1997-2006) when considering only cells with a minimum track count of 2.

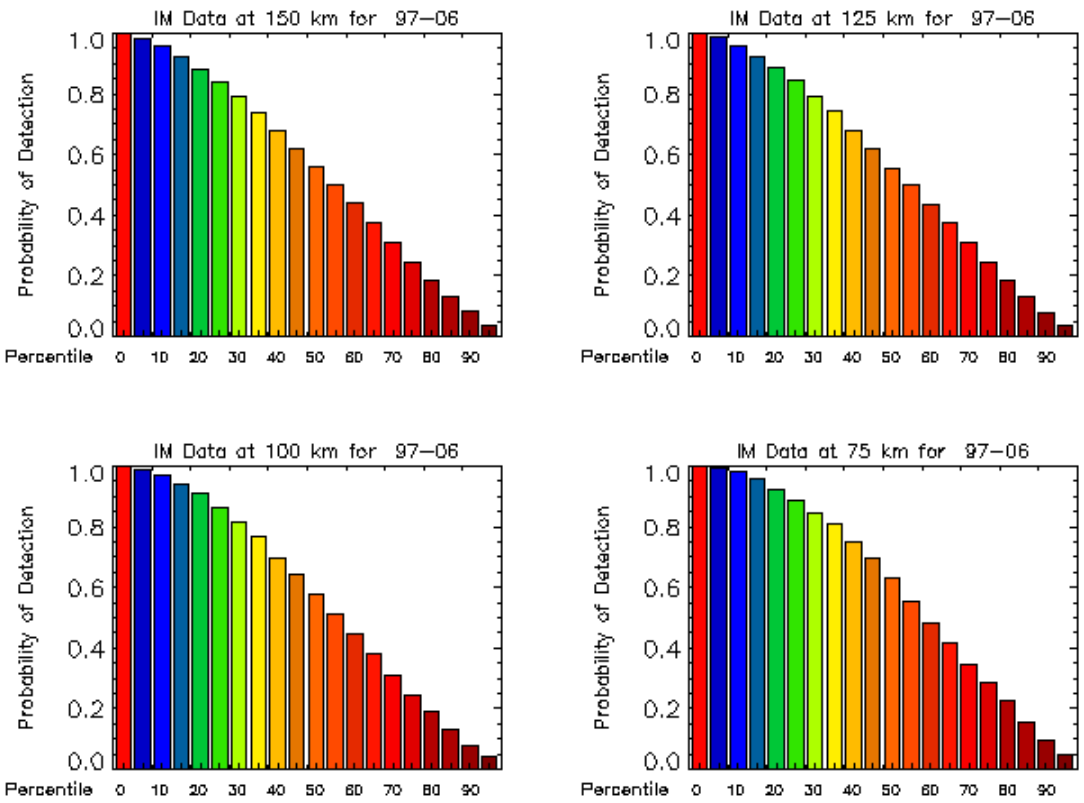

Figure 3.5. Same as Figure 3.4 for the POD values.

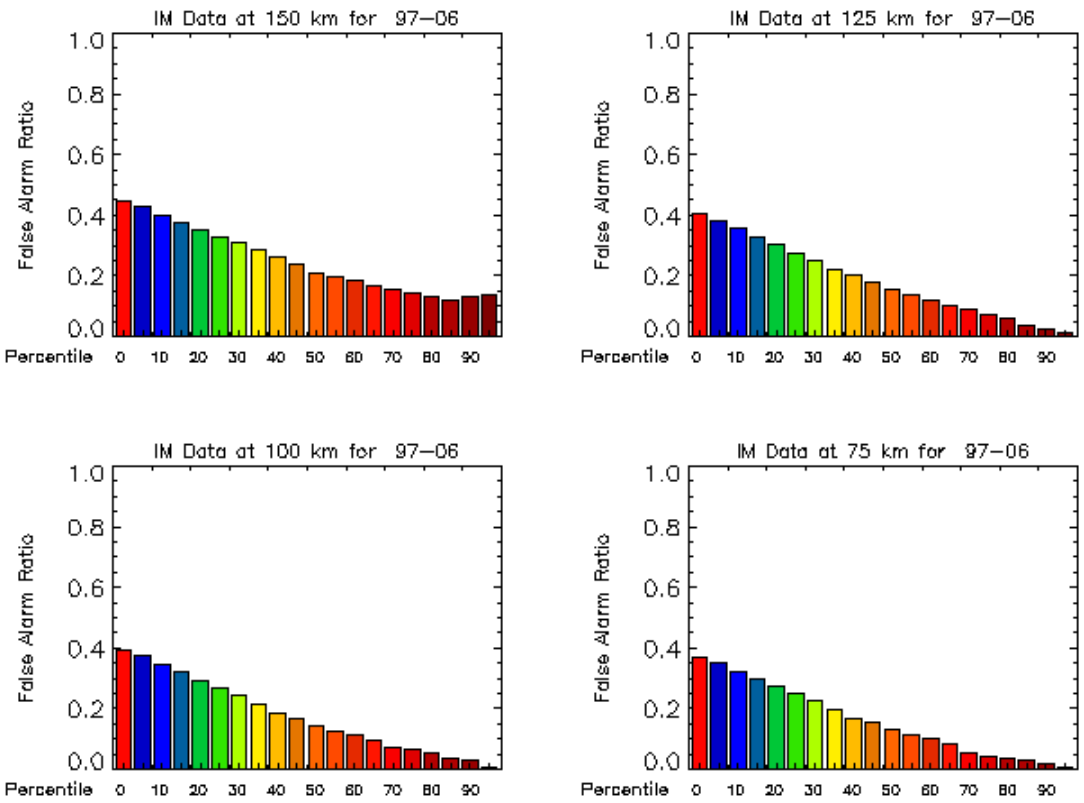

Figure 3.6. Same as Figure 3.4 for the FAR values.

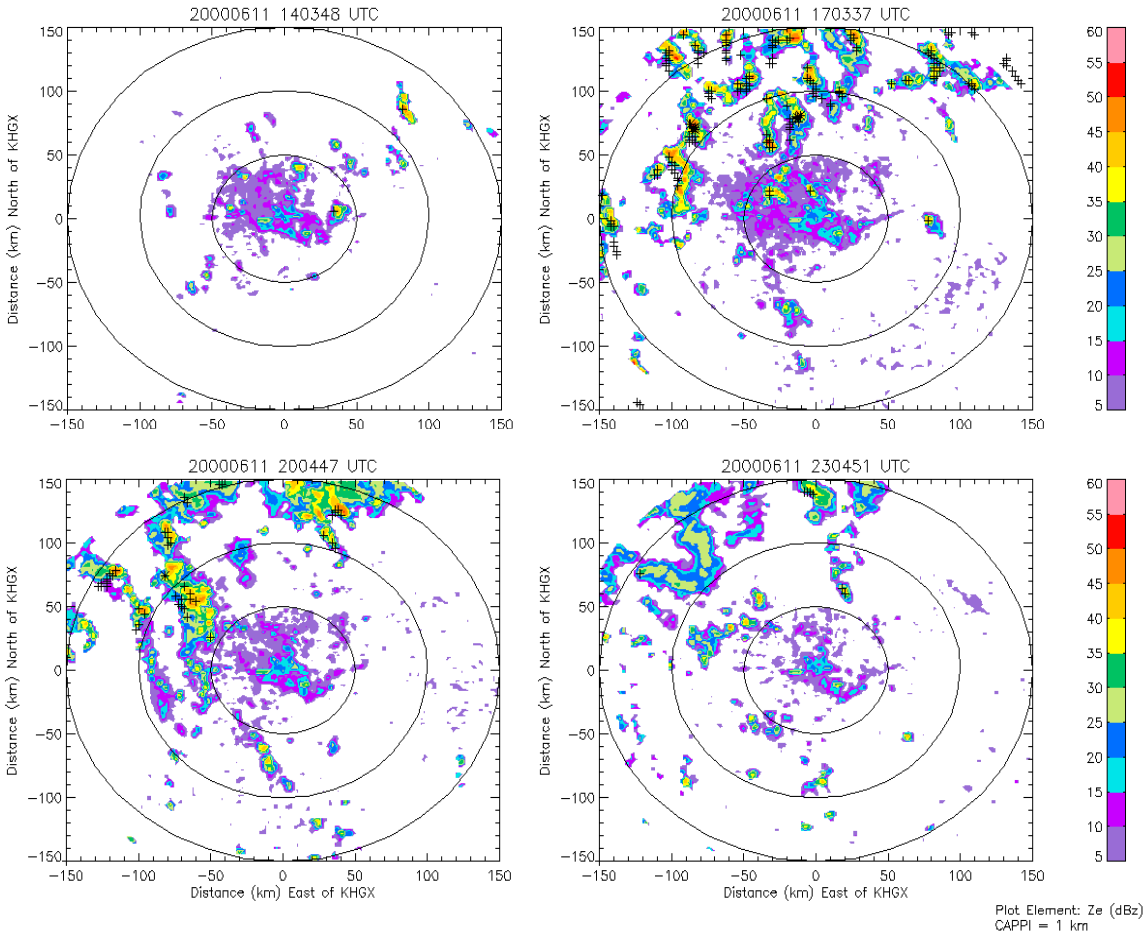

Figure 3.7. Radar images from 11 June 2000 at 1403Z (top-left), 1703Z (top-right), 2004Z (bottom-left), and 2304Z (bottom-right). Rings represent 50, 100, and 150 km from the radar. The grid is centered on the location of the Houston, TX (KHGX) WSR-88D. The data is plotted in constant altitude plan projection indicator (CAPPI) format, which is discussed in Section 2.1.2. The + symbols show centroid locations as determined by the CAPPI-SCIT algorithm and * represent CG lightning locations.

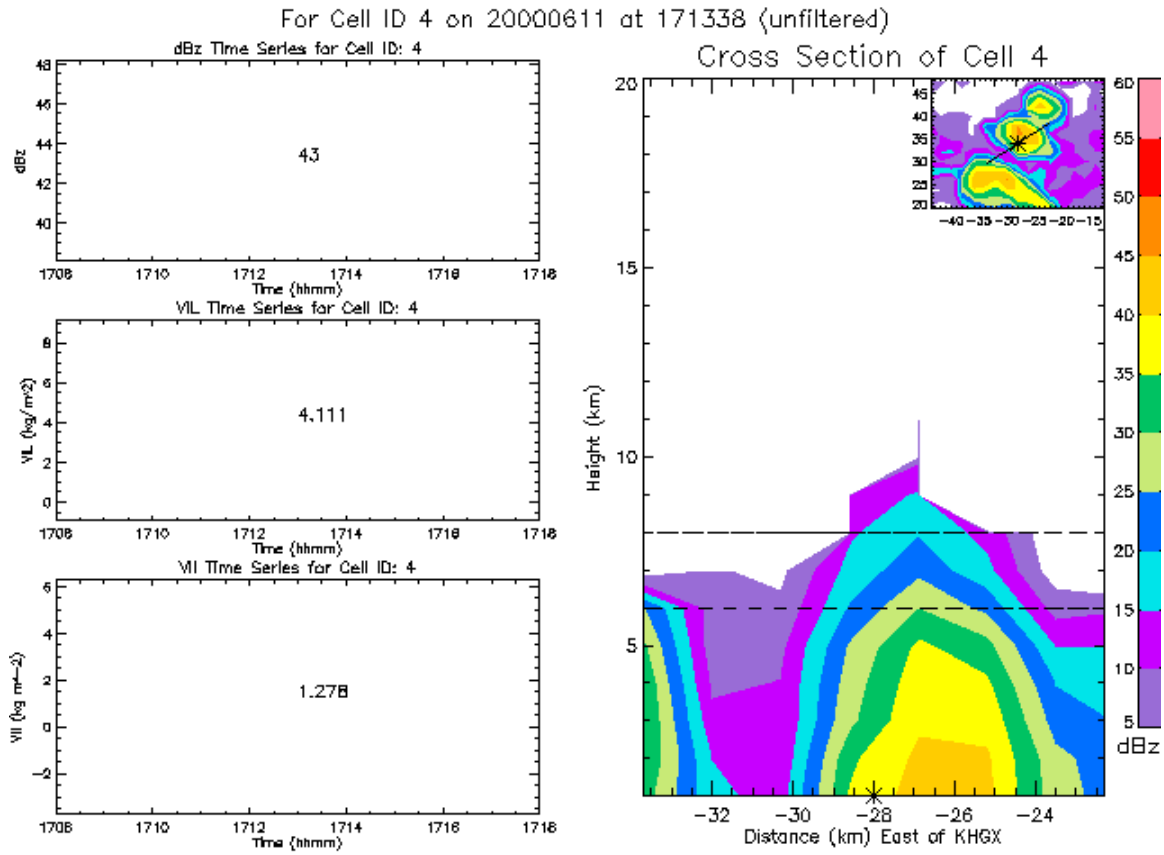

Figure 3.8. For cell 4 ending at 1713Z: Left: time series of maximum reflectivity in dBZ (top), cell-based VIL in kg m^{-2} (middle), and cell-based VII in kg m^{-2} (bottom). Right: cross-section through the CAPPI-SCIT identified cell centroid (* represents the centroid location). Top Right: Plan view showing the location of the cross-section.

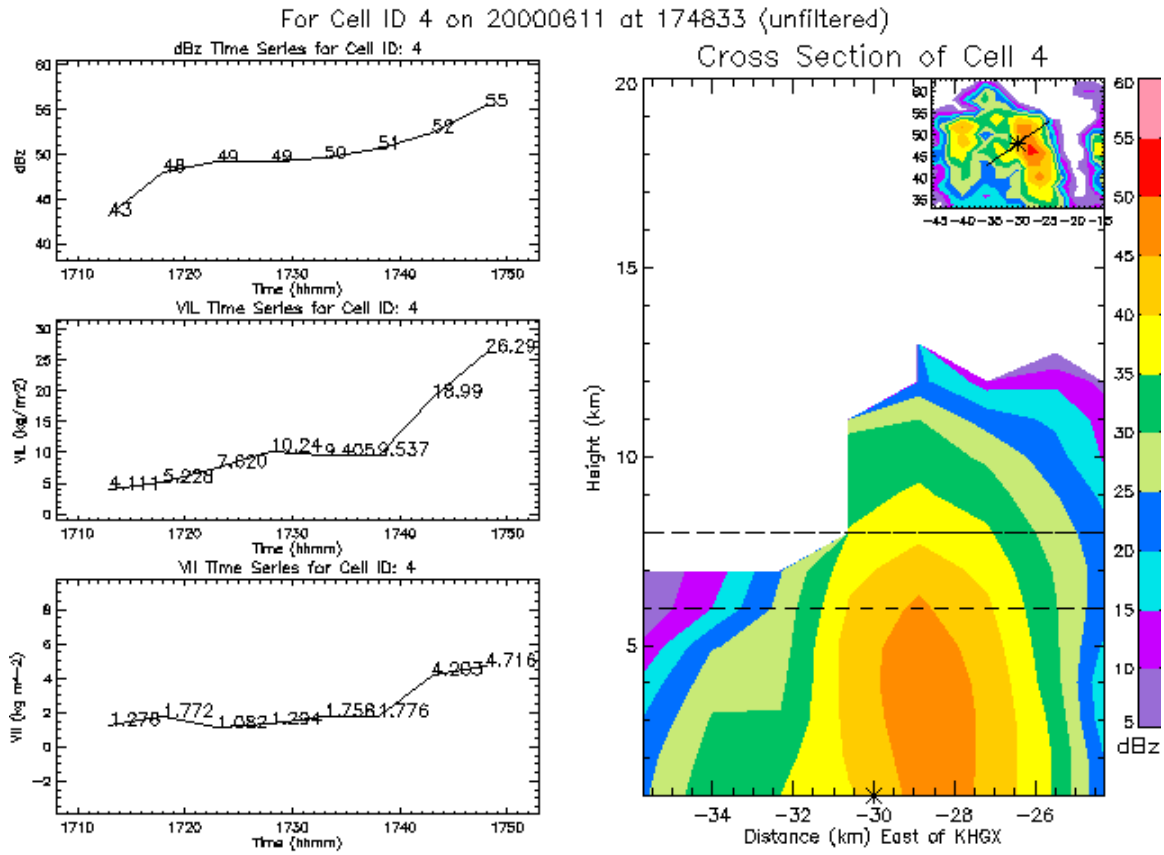

Figure 3.9. Same as Figure 3.8 for cell 4 ending at 1748Z.

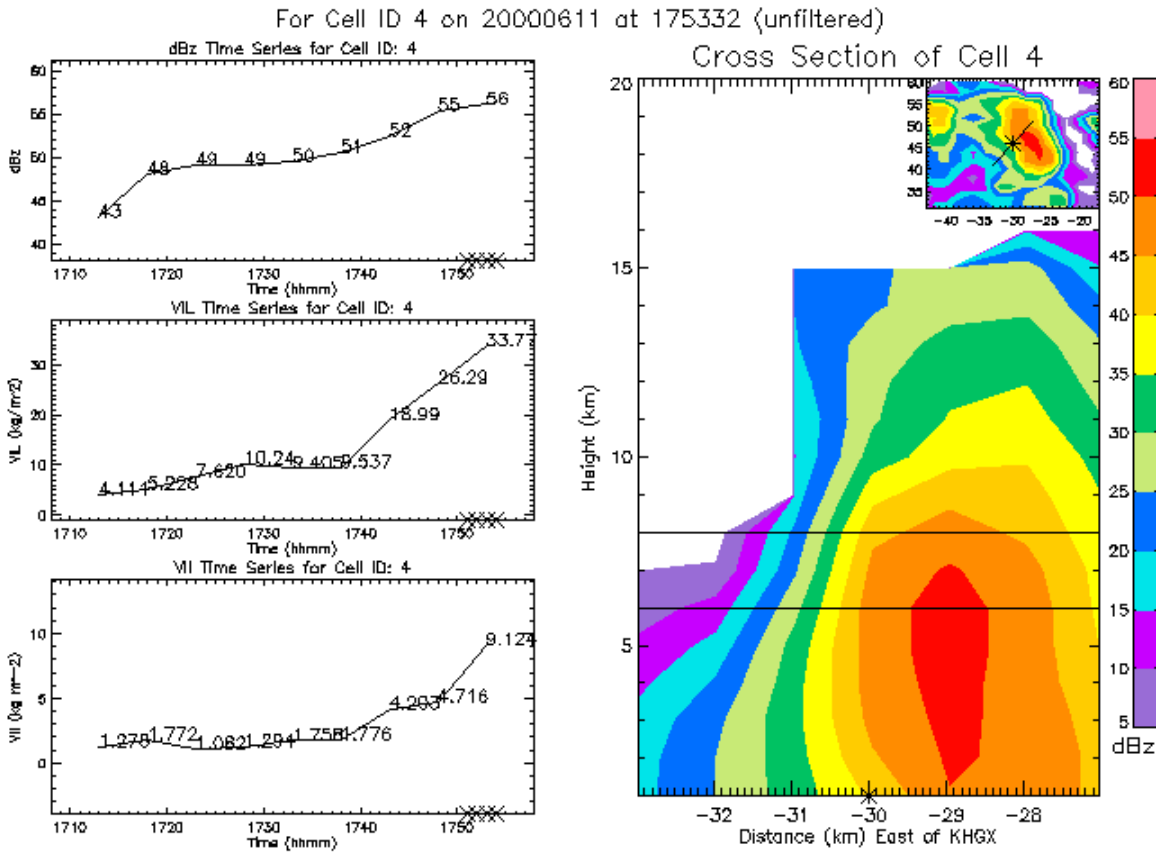

Figure 3.10. Same as Figure 3.8 for cell 4 ending at 1753Z. The X on the x-axis of the time series on the left side represent the time of CG strikes correlated to the cell.

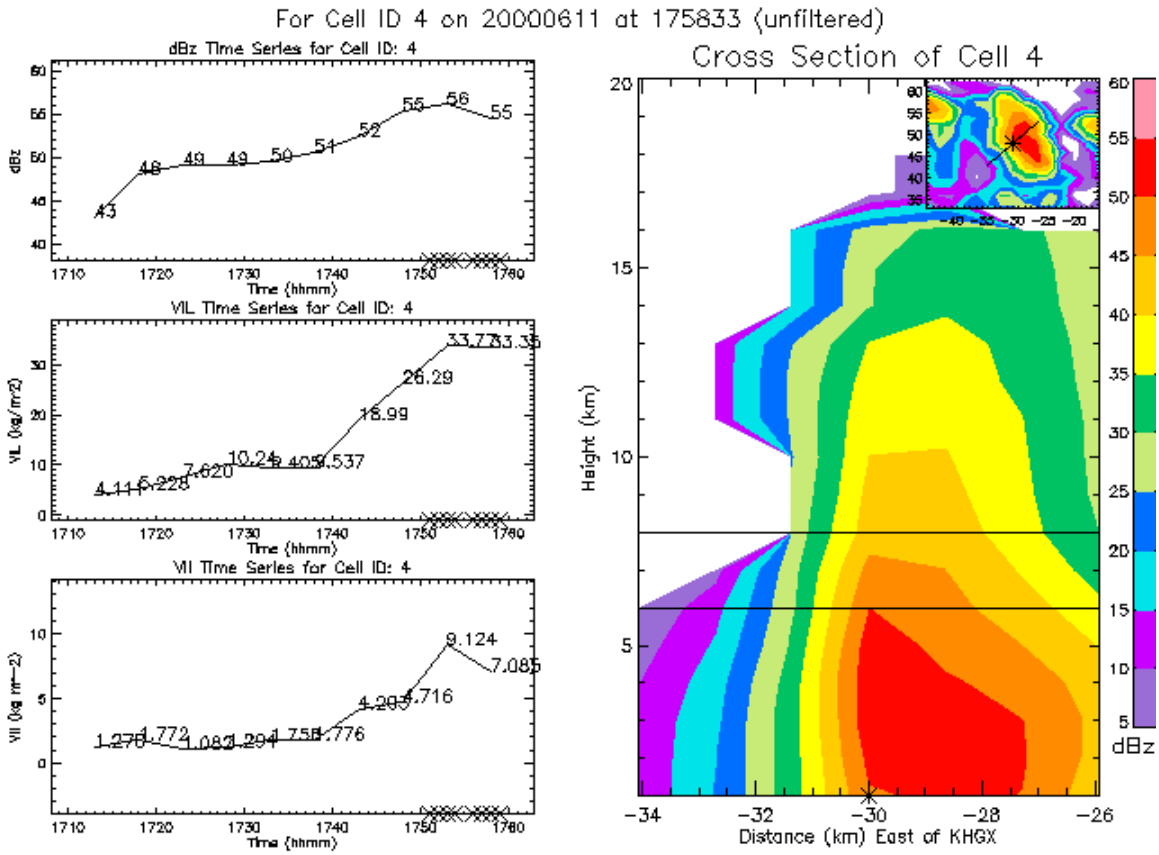

Figure 3.11. Same as Figure 3.10 for cell 4 ending at 1758Z.

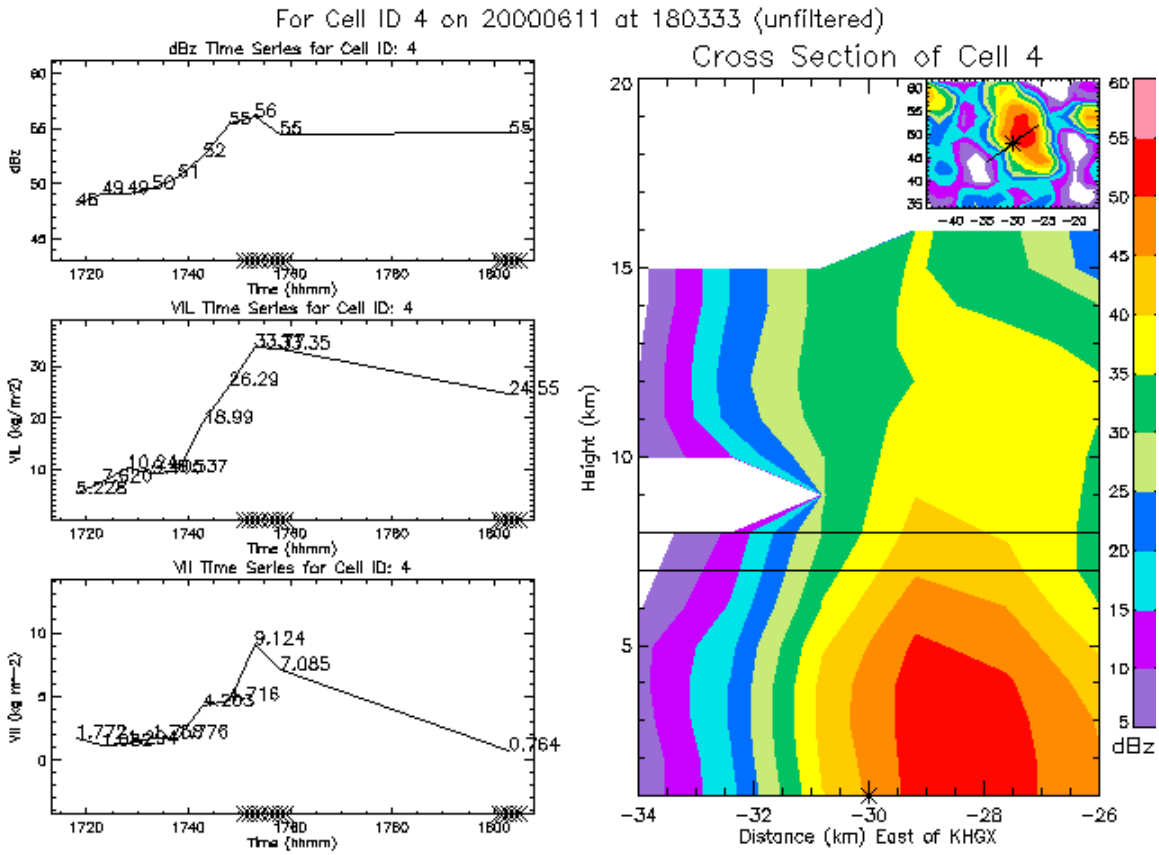

Figure 3.12. Same as Figure 3.10 for cell 4 ending at 1803Z. NOTE: the extended line is a result of a plotting error, not a long time period.

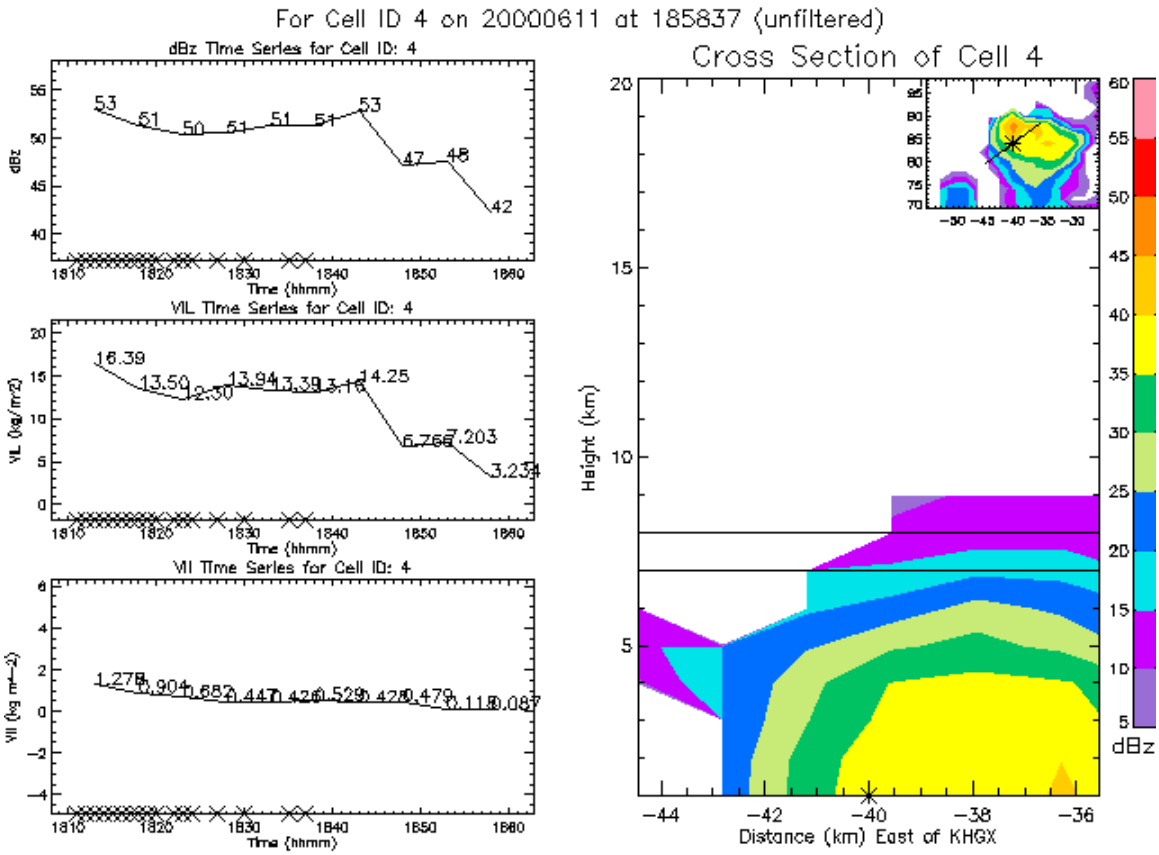

Figure 3.13. Same as Figure 3.10 for cell 4 ending at 1858Z.

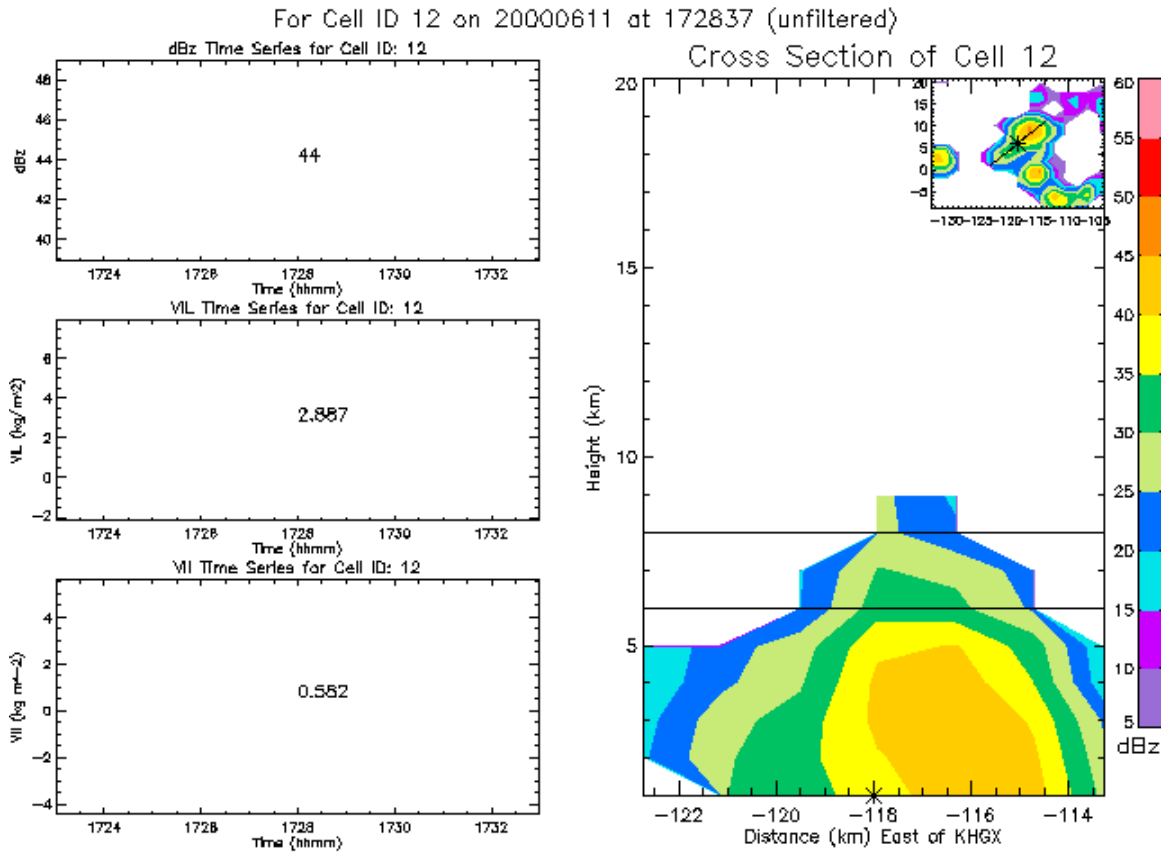

Figure 3.14. Same as Figure 3.10 for cell 12 ending at 1728Z.

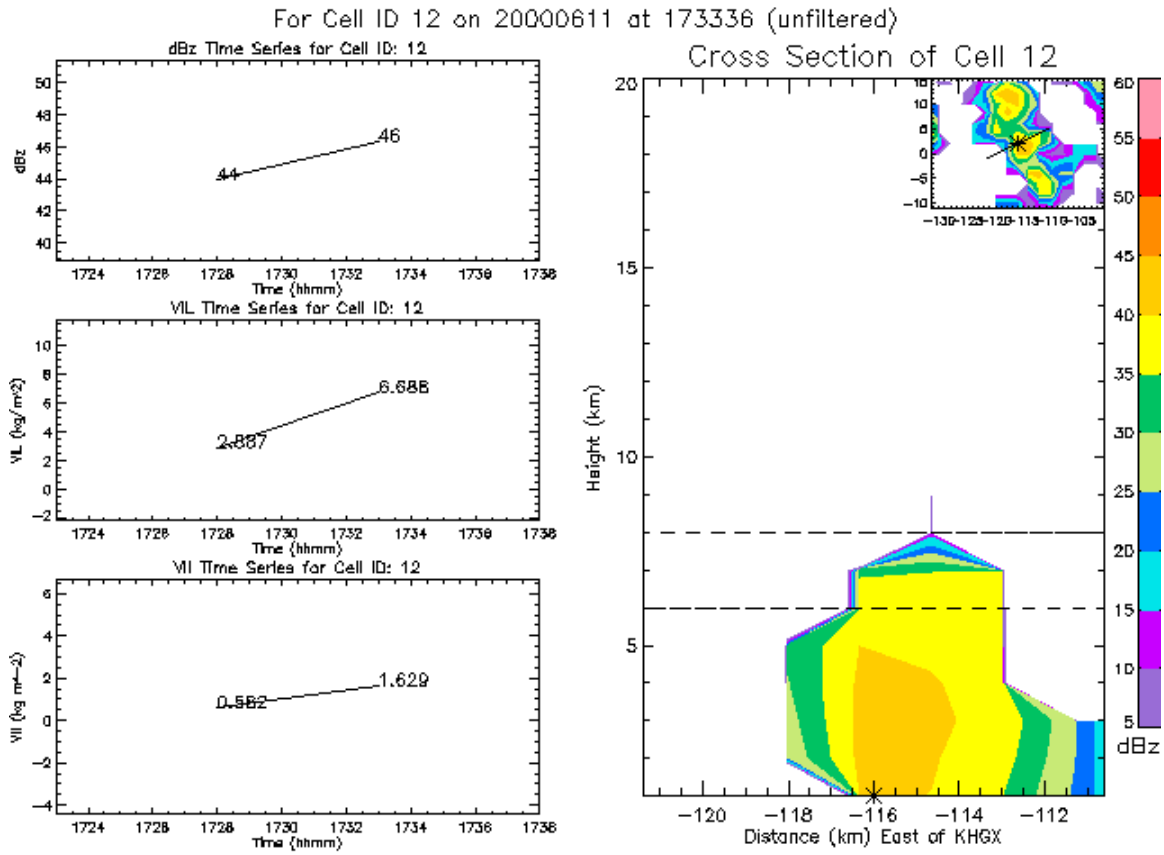

Figure 3.15. Same as Figure 3.10 for cell 12 ending at 1733Z.

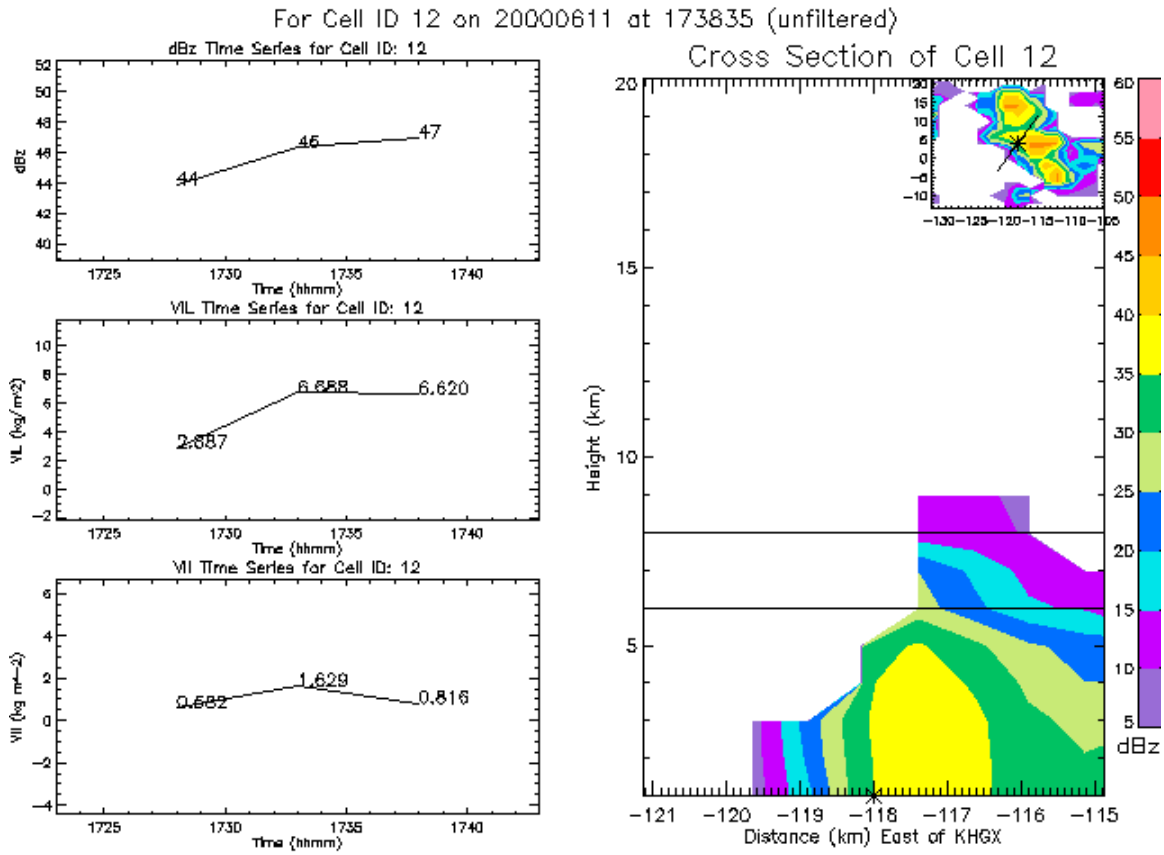

Figure 3.16. Same as Figure 3.10 for cell 12 ending at 1738Z.

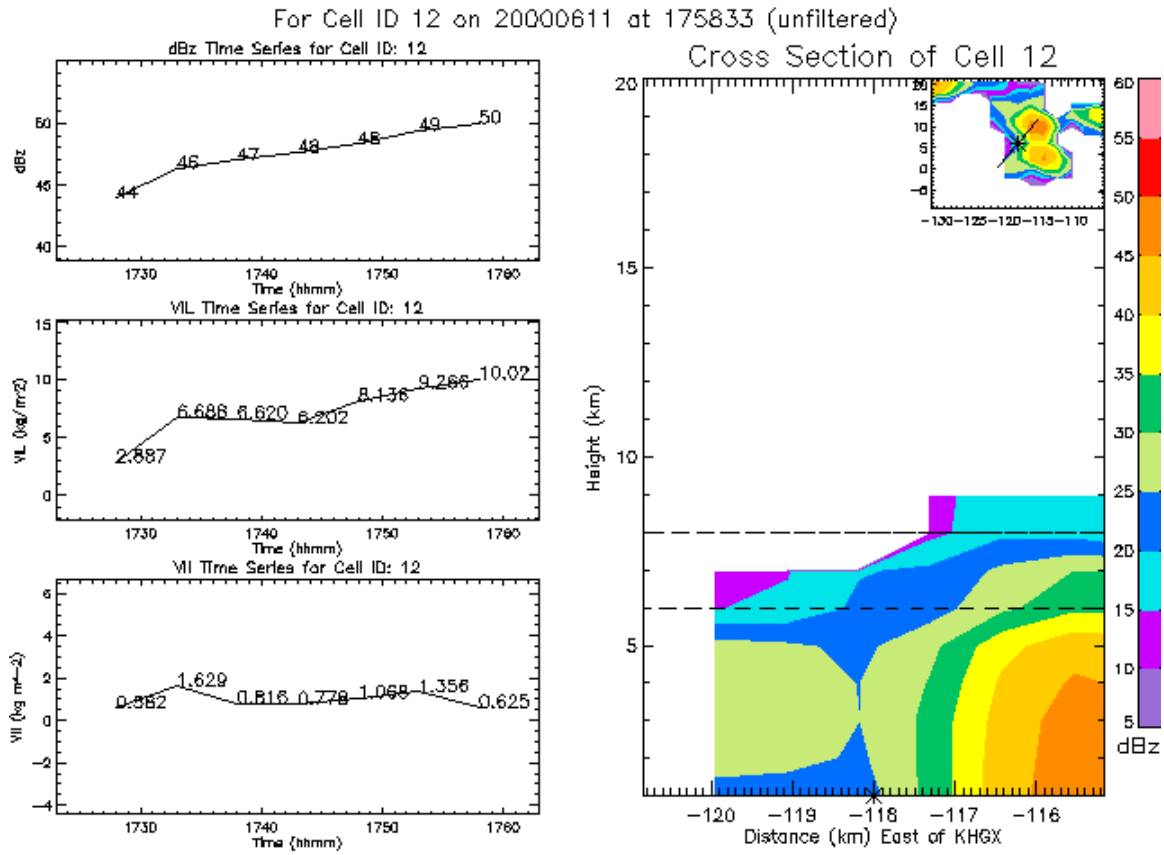

Figure 3.17. Same as Figure 3.10 for cell 12 ending at 1758Z.

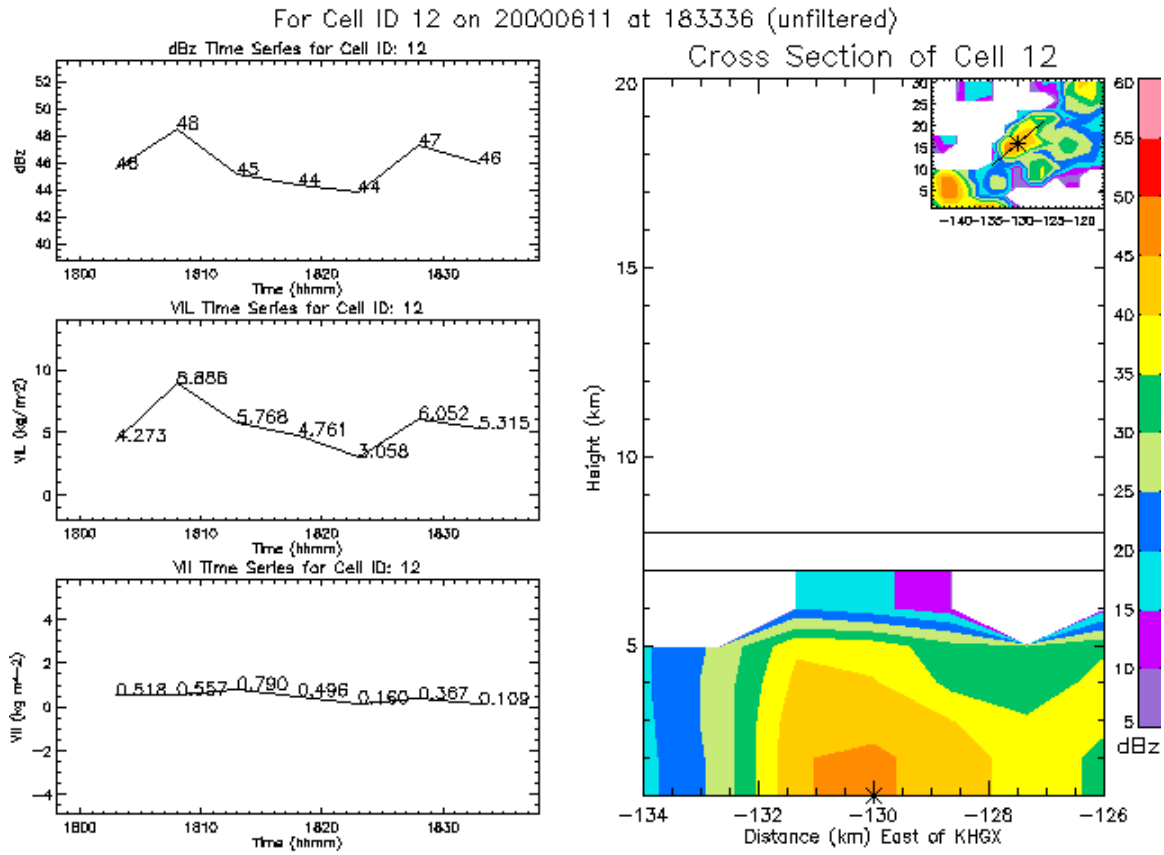

Figure 3.18. Same as Figure 3.10 for cell 12 ending at 1833Z.

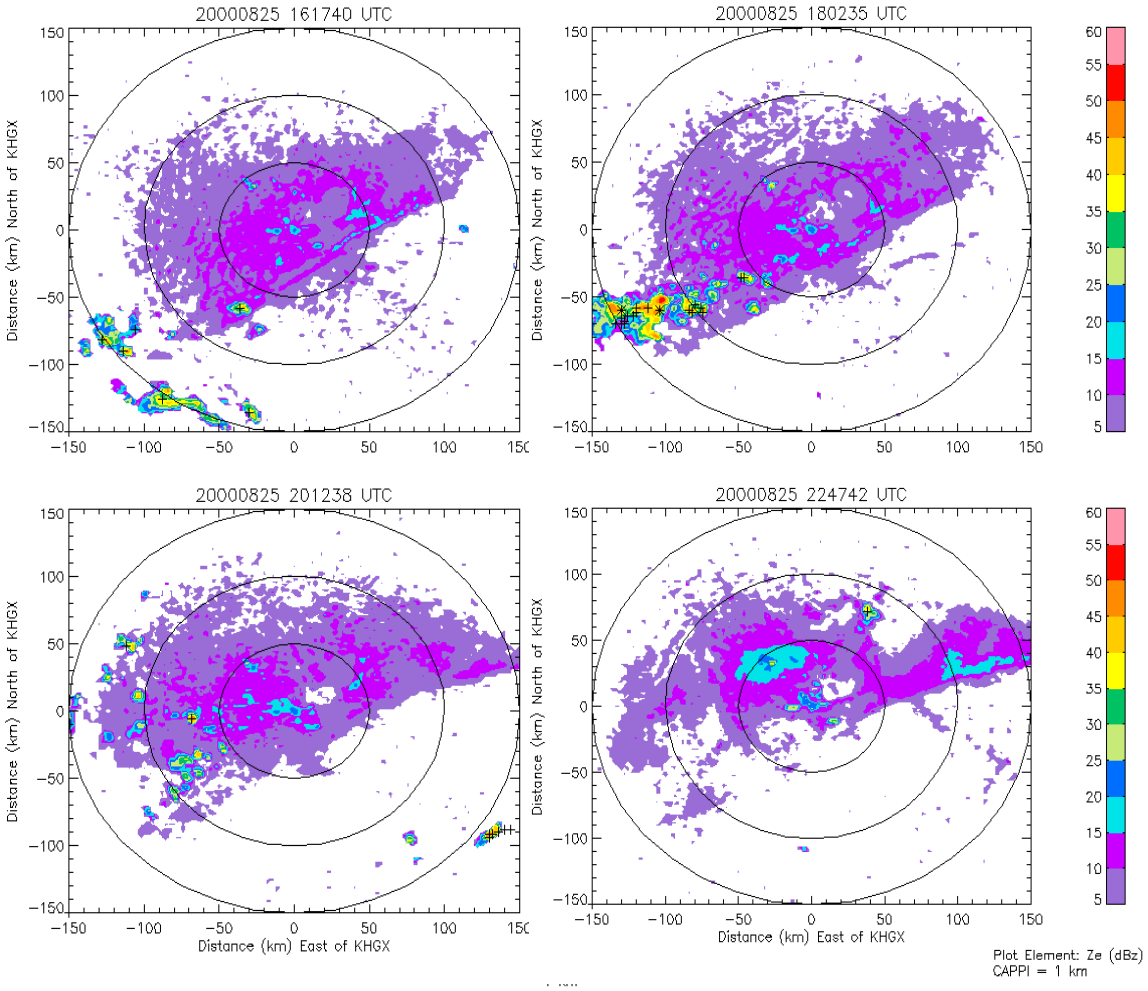

Figure 3.19. Same as Figure 3.7 for 25 August 2000 at 1617Z (top-left), 1802Z (top-right), 2012Z (bottom-left), and 2247Z (bottom-right).

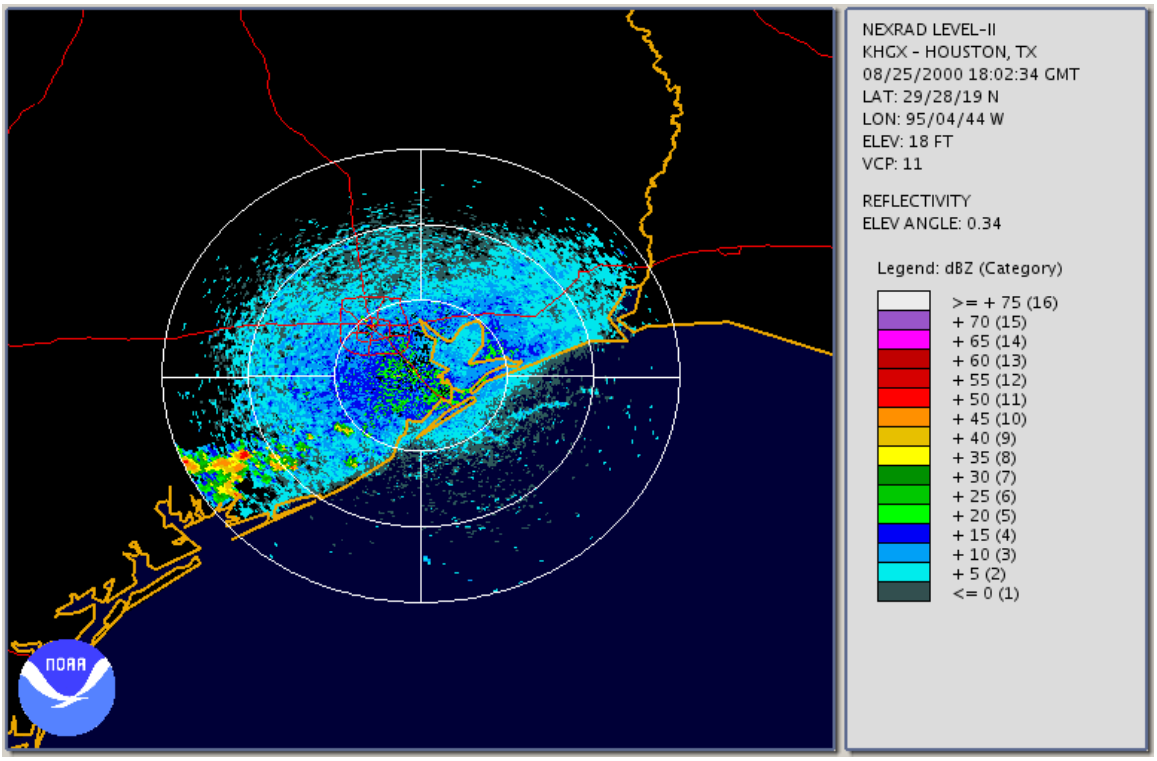

Figure 3.20. Base reflectivity (0.34°) image from 25 August 2000 at 1802Z. Created using the NOAA Weather and Climate Toolkit available from the National Climatic Data Center. Range rings are every 50 km out to 150 km.

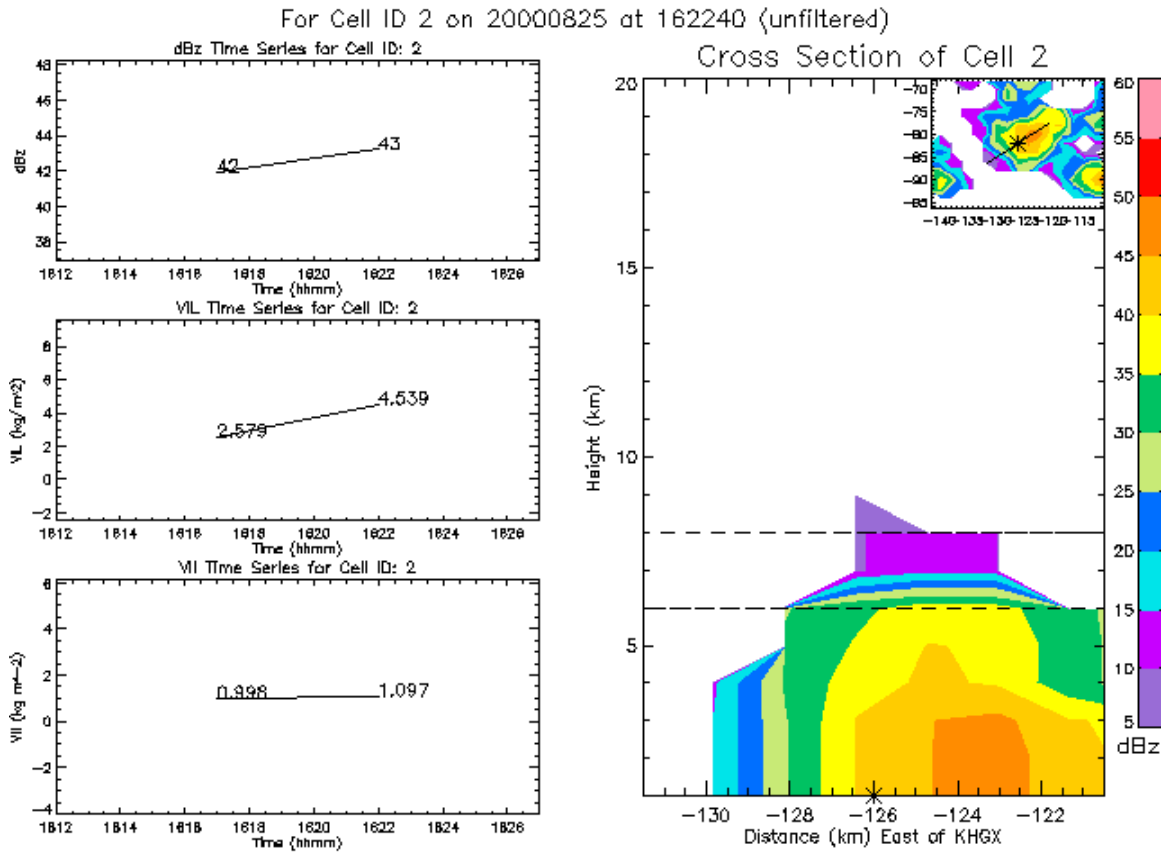

Figure 3.21. Same as Figure 3.10 for cell 2 on 25 August 2000 ending at 1622Z.

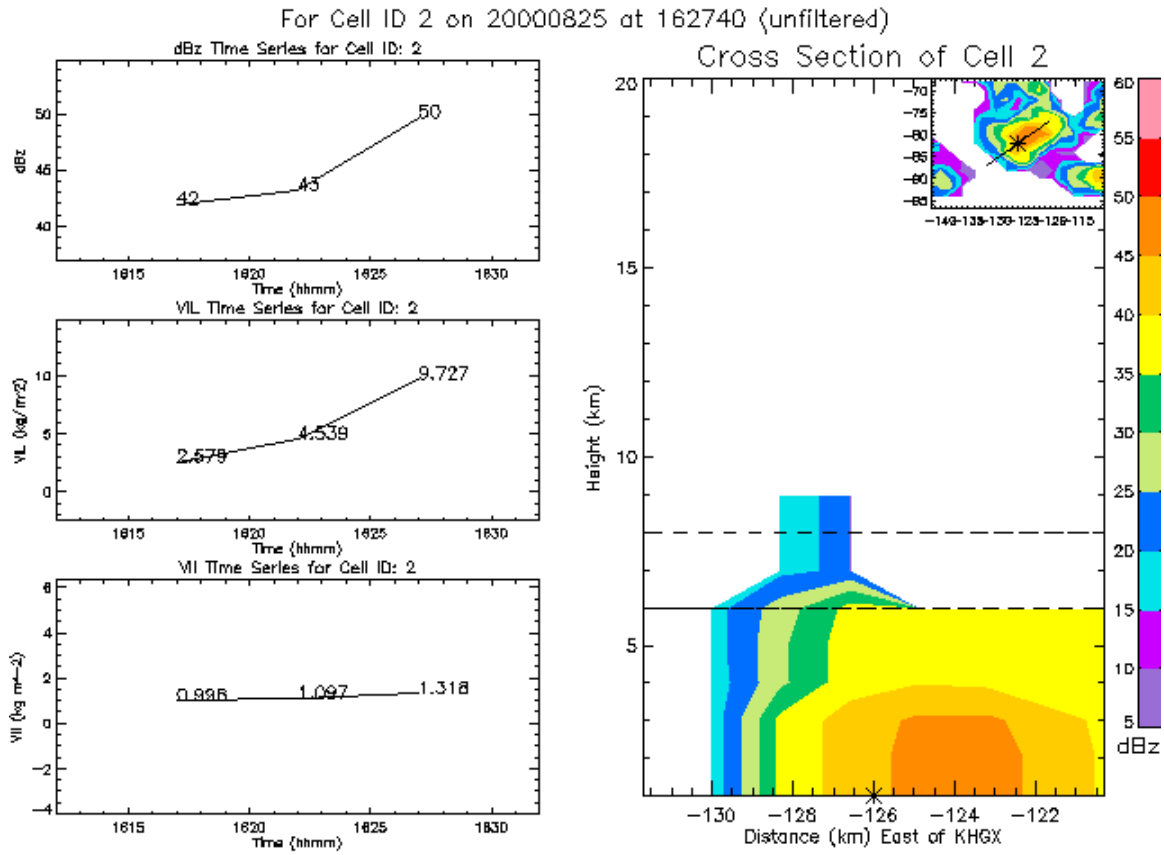

Figure 3.22. Same as Figure 3.10 for cell 2 on 25 August 2000 ending at 1627Z.

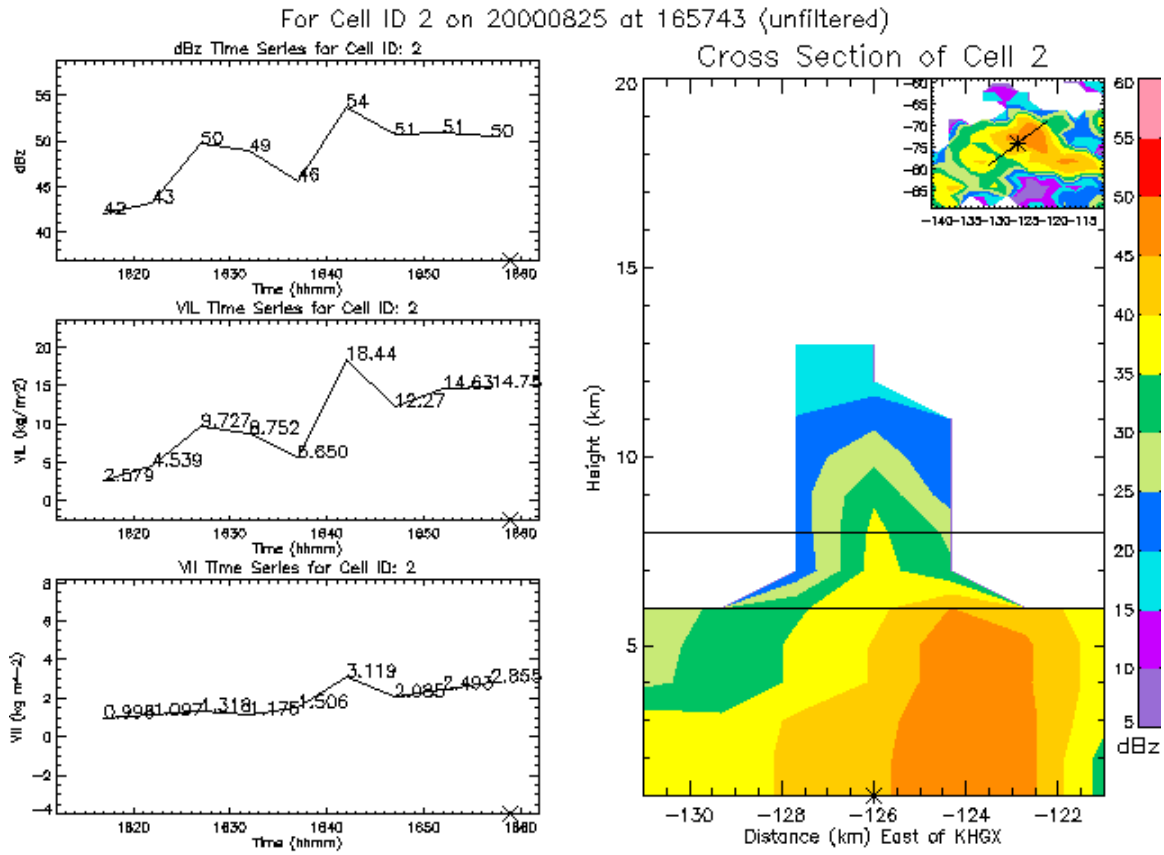

Figure 3.23. Same as Figure 3.10 for cell 2 on 25 August 2000 ending at 1657Z.

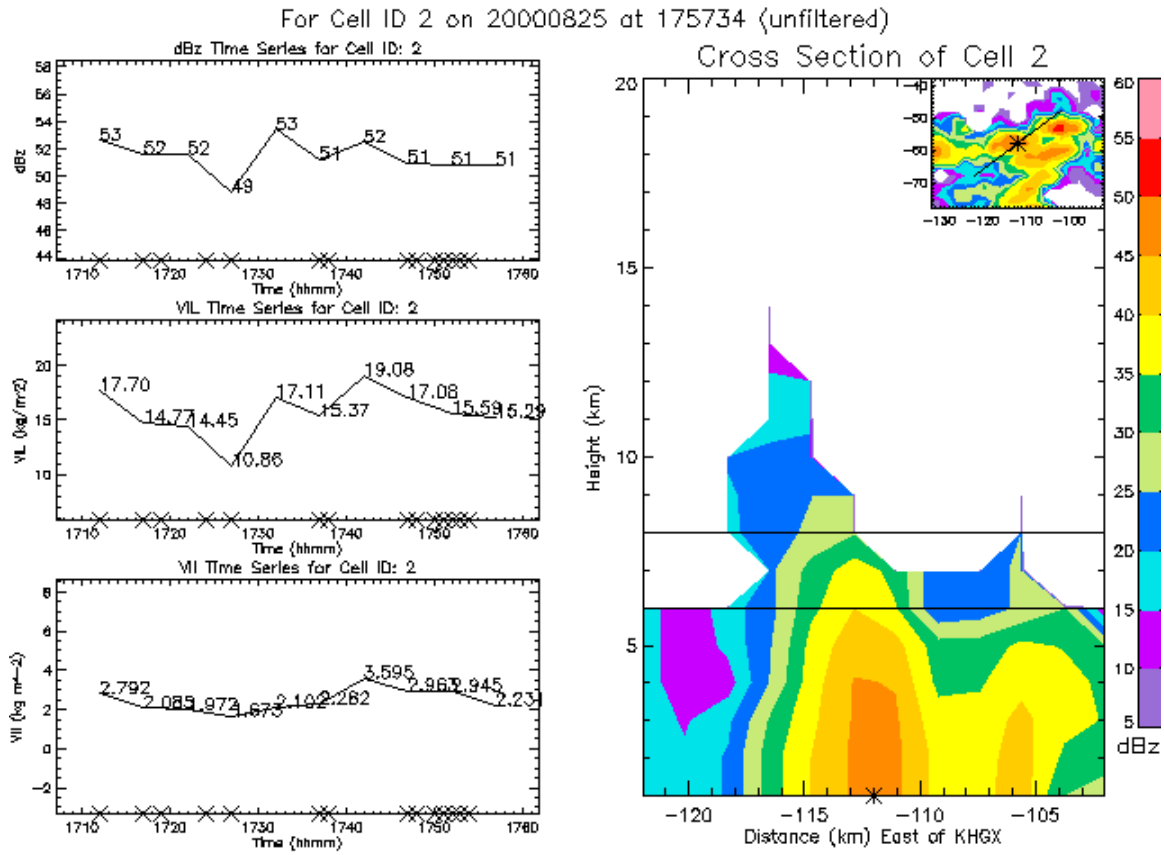

Figure 3.24. Same as Figure 3.10 for cell 2 on 25 August 2000 ending at 1757Z.

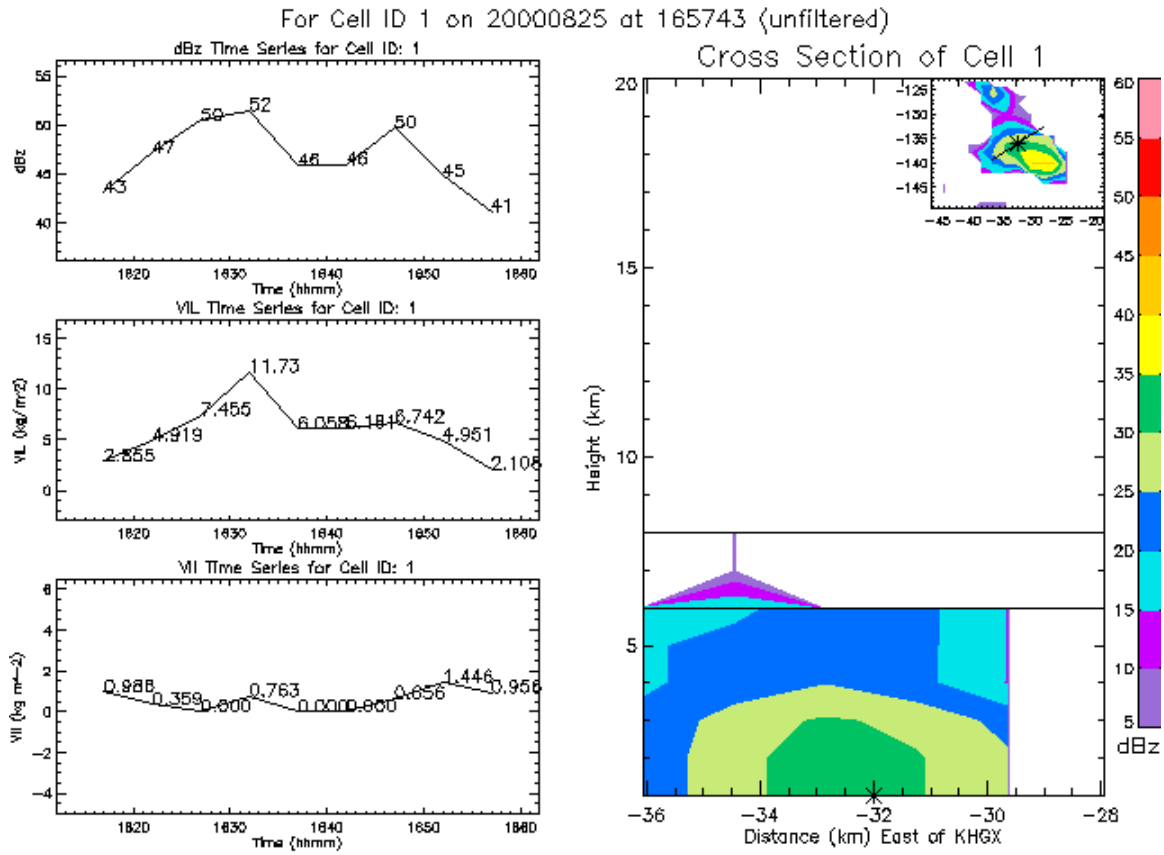

Figure 3.25. Same as Figure 3.11 for cell 1 on 25 August 2000 ending at 1657Z.

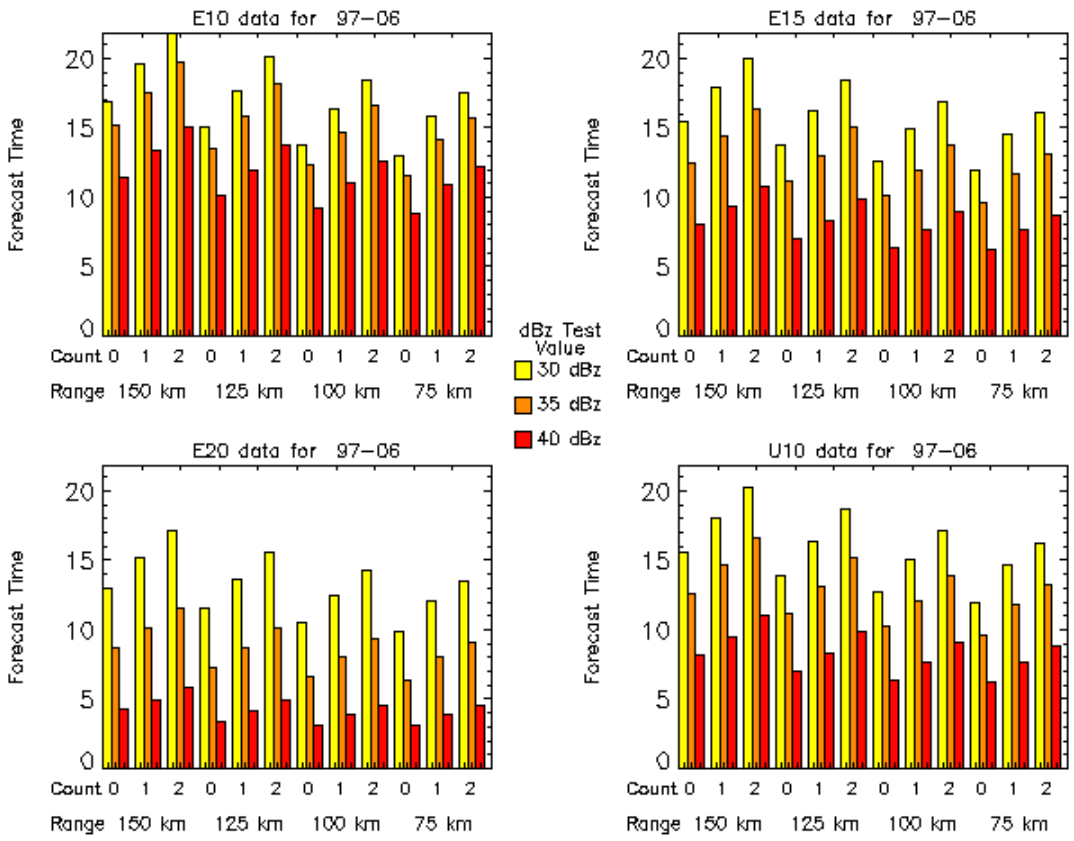

Figure 3.26. Same as Figure 3.1 for forecast time (in minutes).

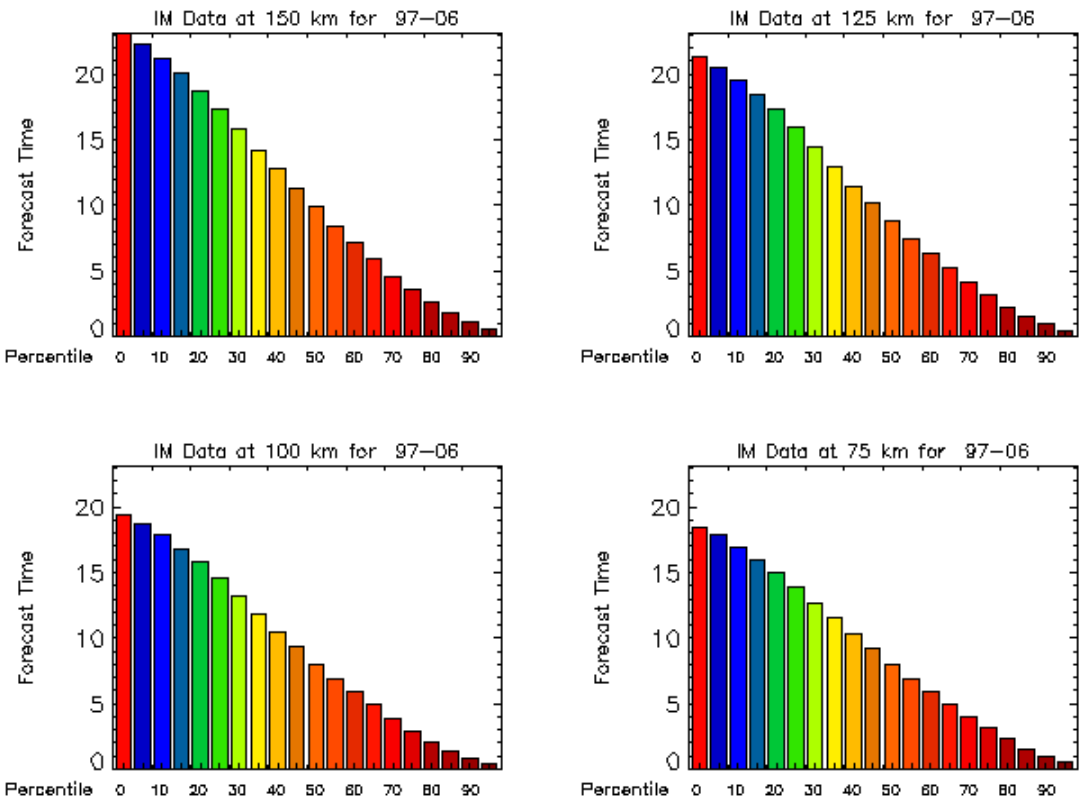

Figure 3.27. Same as Figure 3.5 for the forecast time.

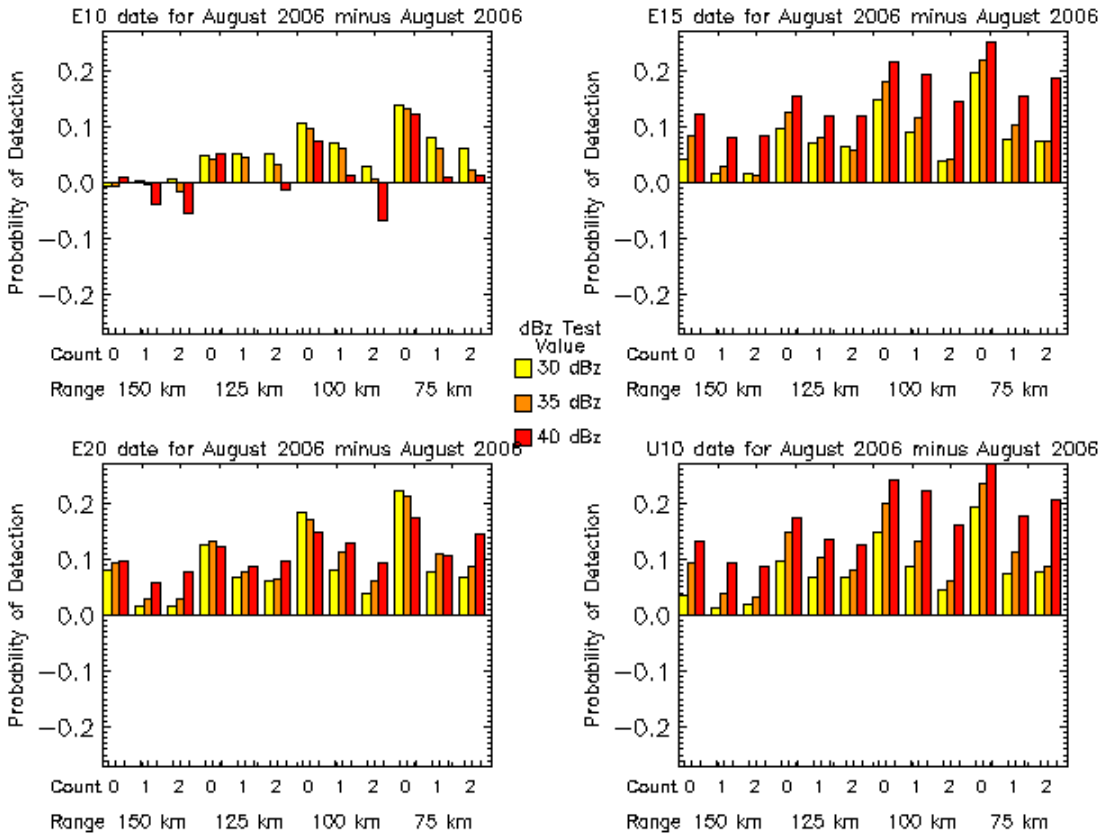

Figure A.1. 1.0 km vertical resolution POD minus 0.5 vertical resolution POD.

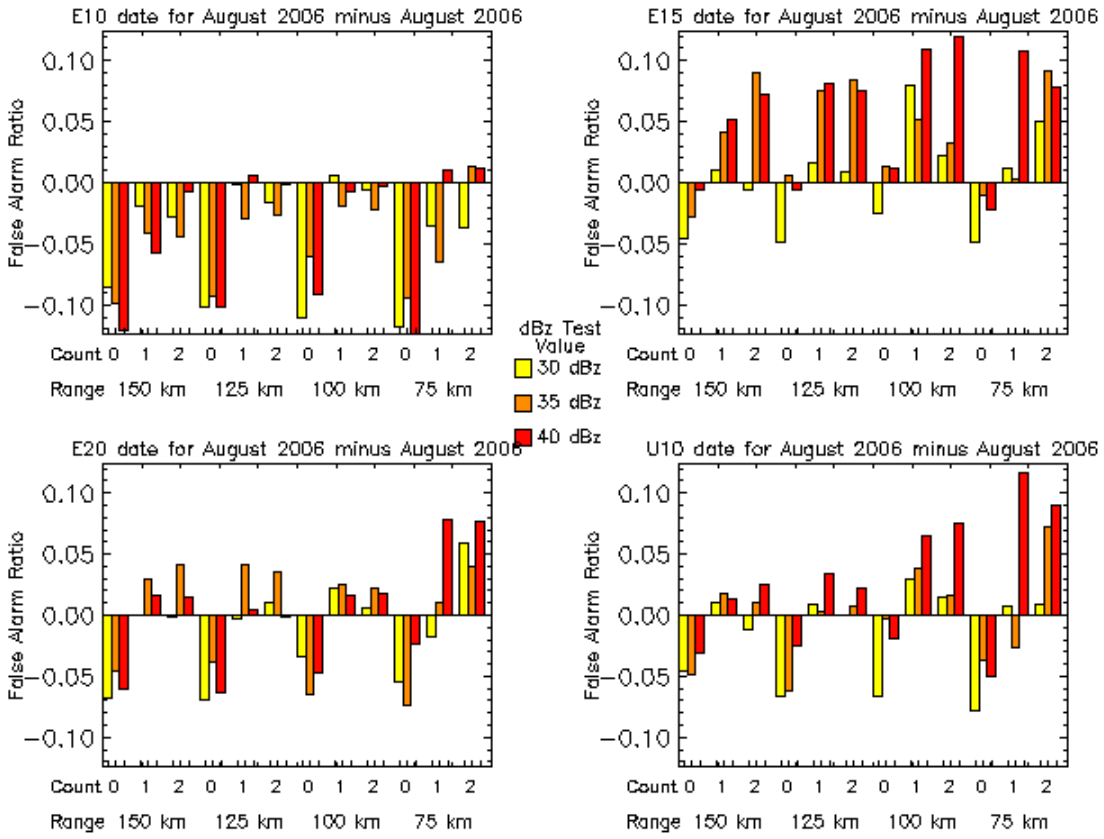

Figure A.2. 1.0 km vertical resolution FAR minus 0.5 vertical resolution FAR.

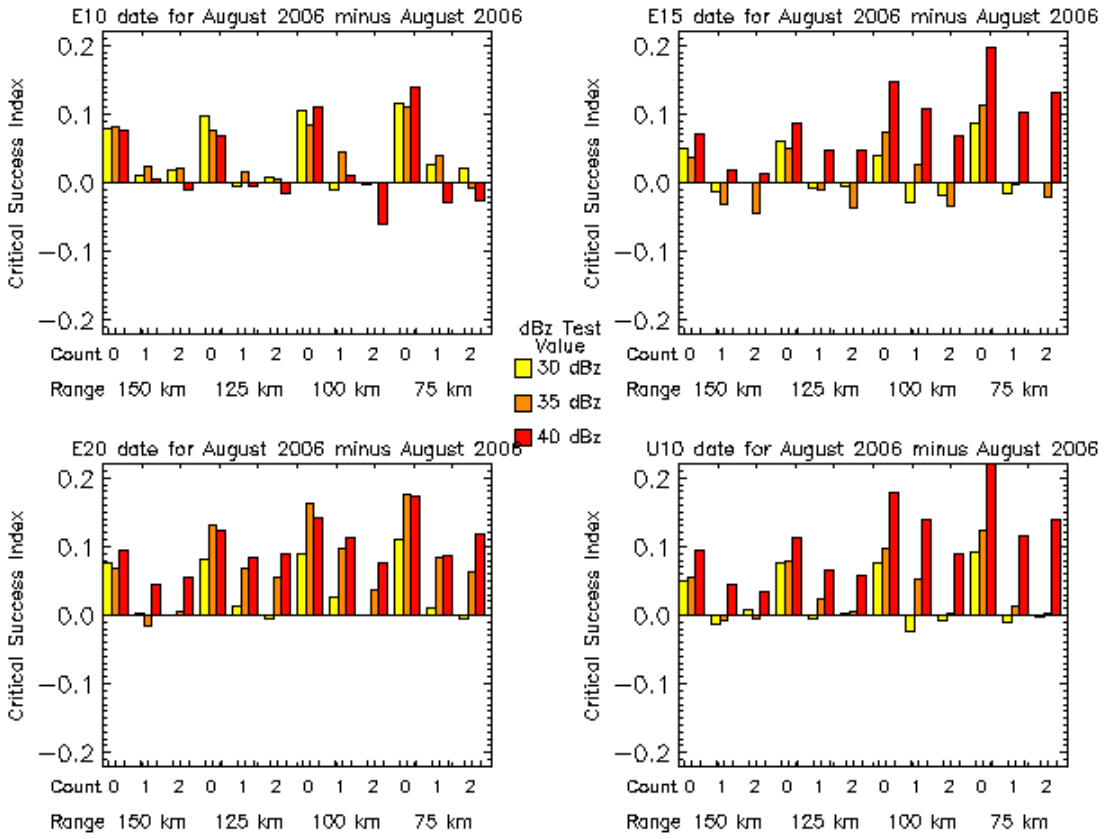

Figure A.3. 1.0 km vertical resolution CSI minus 0.5 vertical resolution CSI.

APPENDIX C

Table 1.1 Statistics on the number of deaths due to hazardous weather (from Curran et al. 2000).

Weather type	30-yr deaths per year	1994 deaths	1994 injuries
Flash flood	139	59	33
River flood		32	14
Lightning	87	69	484
Tornado	82	69	1067
Hurricane	27	9	45
Extreme temperature		81	298
Winter weather		31	2690
Thunderstorm wind		17	315
Other high wind		12	61
Fog		3	99
Other		6	59
Total		388	5165

Table 1.2. Annual convective weather deaths, injuries, and property damage reports from 1992 – 1994 (from Curran et al. 2000).

Convective weather type	Fatalities	Injuries	Damage ($ million)
Lightning	51	345	32
Tornadoes	47	1,114	551
Thunderstorm wind	18	352	295
Hail	0	43	345

Table 1.3. Results for the statistical analysis of lightning initiation signatures in this study. (a) Statistics for -10 °C, (b) -15 °C, (c) -20 °C (from Gremillion and Orville 1999).

(a)

(dBZ)	Probability of detection (%)	False alarm rate (%)	Critical success index (%)	Median time lag (min)
35	88	20	72	7.5
40	84	7	79	7.5
45	29	0	29	12.5

(b)

(dBZ)	Probability of detection (%)	False alarm rate (%)	Critical success index (%)	Median time lag (min)
25	84	24	67	14.8
30	81	14	71	12.5
35	70	16	62	6.0

(c)

(dBZ)	Probability of detection (%)	False alarm rate (%)	Critical success index (%)	Median time lag (min)
20	81	26	63	10.5
25	71	15	63	9.3
30	52	20	46	8.0

Table 1.4. Results using the updraft -10°C level (U-10L) and -6°C level (U-6L) with the 40 dBZ test value (from Wolf 2006).

	CG	*No CG*	*Total*	*POD*
U-10L	*834*	*34*	*868*	*96%*
U-6L	*863*	*5*	*868*	*99%*

	Verified	*Unverified*	*Total*	*FAR*
U-10L	*834*	*99*	*933*	*11%*
U-6L	*863*	*210*	*1073*	*20%*

Table 1.5. Results of using various heights (4,000 and 8,000 ft above updraft -10°C level) of 40dBZ echo to forecast frequent or numerous (F/N) lightning events (from Wolf 2006).

	F/N	*No F/N*	*Total*	*POD*		*Verified*	*Unverified*	*Total*	*FAR*
U-10L+8k	*284*	*12*	*296*	*96%*	***U-10L+8k***	*284*	*136*	*420*	*33%*
U-10L+4k	*296*	*0*	*296*	*100%*	***U-10L+4k***	*296*	*266*	*562*	*47%*

Table 2.1.WSR-88D radar specifications.

Antenna	
Diameter, ft	28
m	8.5
Beamwidth	0.93
Gain	45 dB
Polarization	Linear Horizontal
Transmitter	
Band	C
Wavelength	10.71 cm
Frequency Range	2700 MHz to 3000 MHz
Pulse Length	1.57 and 4.5 μs
Peak Power	750 kW
PRFs	Short: 318 Hz to 1304 Hz
	Long: 318 Hz to 452 Hz
Receiver	
3dB Bandwidth	0.63 MHz
MDS	(-) 113 dBm
Dynamic Range	93 dB
Gate Spacing	250 m
Zmin @ 50km	(-)20.7 dBz

Table 2.2. Summary of the WSR-88D scan strategies (from OFCM 2008).

Quick Reference VCP Comparison Table for RPG Operators					February 2008
Slices	Tilts	VCP	Time*	Usage	Limitations
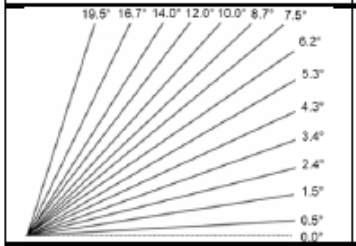	14	11	5 mins	Severe and non-severe convective events. Local 11 has Rmax=80nm. Remote 11 has Rmax=94nm.	Fewer low elevation angles make this VCP less effective for long-range detection of storm features when compared to VCPs 12 and 212.
		211	5 mins	Widespread precipitation events with embedded, severe convective activity (e.g. MCS, hurricane). Significantly reduces range-obscured V/SW data when compared to VCP 11.	All Bins clutter suppression is NOT recommended. PRFs are not editable for SZ-2 (Split Cut) tilts.
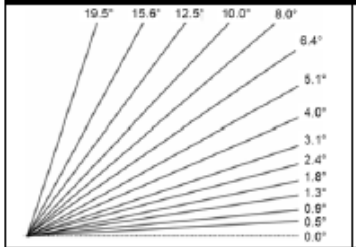	14	12	4 ½ mins	Severe convective events. Extra low elevation angles increase low-level vertical resolution when compared to VCP 11.	High antenna rotation rates slightly decrease accuracy of the base data estimates.
		212	4½ mins	Rapidly evolving, widespread severe convective events (e.g. squall line, MCS). Increased low-level vertical resolution compared to VCP 11. Significantly reduces range-obscured V/SW data when compared to VCP 12.	All Bins clutter suppression is NOT recommended. PRFs are not editable for SZ-2 (Split Cut) tilts. High antenna rotation rates slightly decrease accuracy of the base data estimates.
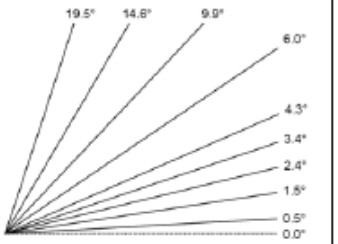	9	21	6 mins	Non-severe convective precipitation events. Local 21 has Rmax=80nm. Remote 21 has Rmax=94nm.	Gaps in coverage above 5°.
		121	6 mins	VCP of choice for hurricanes. Widespread stratiform precipitation events. Significantly reduces range-obscured V/SW data within 230 km when compared to other VCPs.	All Bins clutter suppression is NOT recommended. High antenna rotation rates slightly decrease accuracy of the base data estimates. PRFs are not editable. Gaps in coverage above 5°.
		221	6 mins	Widespread precipitation events with embedded, possibly severe convective activity (e.g. MCS, hurricane). Reduces range-obscured V/SW data out to 300 km when compared to other VCPs.	All Bins clutter suppression is NOT recommended. PRFs are not editable for SZ-2 (Split Cut) tilts. Gaps in coverage above 5°.
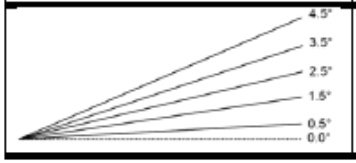	5	31	10 mins	Clear-air, snow, and light stratiform precipitation. Best sensitivity. Detailed boundary layer structure often evident.	Susceptible to velocity dealiasing failures. No coverage above 5°. Rapidly developing convective echoes aloft might be missed.
		32	10 mins	Clear-air, snow, and light stratiform precipitation.	No coverage above 5°. Rapidly developing convective echoes aloft might be missed.

Table 2.3. A 2 x 2 contingency table and formulas for computing forecast skill.

	PREDICTED		
	Yes	No	X = Hit
OBSERVED			Y = Miss
Yes	X	Y	Z = False Alarm
No	Z	W	W = Correct No Forecast
Probability of Detection:			POD = x / (x + y)
False Alarm Ratio:			FAR = z / (x + z)
Critical Success Index:			CSI = x / (x + y + z)

Table 3.1. Forecast statistics using the -10 °C isotherm for the entire dataset (1997 – 2006).

Environmental -10 C Level												
E10-30 dBz Test												
Within Dist	**150**			**125**			**100**			**75**		
Track Count	**0**	**1**	**2**	**0**	**1**	**2**	**0**	**1**	**2**	**0**	**1**	**2**
# of Cells	65399	38272	26734	41814	23908	16420	25028	14101	9676	13255	7324	4947
POD	0.92	0.96	0.97	0.92	0.96	0.98	0.93	0.96	0.98	0.94	0.97	0.99
FAR	0.59	0.5	0.42	0.57	0.46	0.37	0.56	0.45	0.36	0.55	0.42	0.34
CSI	0.39	0.49	0.57	0.41	0.52	0.62	0.42	0.53	0.63	0.44	0.57	0.65
FCST TIME	16.87	19.55	21.81	15.06	17.71	20.12	13.75	16.38	18.42	13.01	15.87	17.52
E10-35 dBz Test												
Within Dist	**150**			**125**			**100**			**75**		
Track Count	**0**	**1**	**2**	**0**	**1**	**2**	**0**	**1**	**2**	**0**	**1**	**2**
# of Cells	65399	38272	26734	41814	23908	16420	25028	14101	9676	13255	7324	4947
POD	0.83	0.88	0.91	0.83	0.88	0.92	0.84	0.9	0.93	0.86	0.92	0.95
FAR	0.52	0.44	0.37	0.49	0.4	0.32	0.49	0.39	0.32	0.47	0.36	0.3
CSI	0.43	0.51	0.59	0.44	0.54	0.63	0.46	0.56	0.65	0.47	0.59	0.68
FCST TIME	15.18	17.58	19.72	13.54	15.89	18.18	12.3	14.65	16.57	11.54	14.09	15.69
E10-40 dBz Test												
Within Dist	**150**			**125**			**100**			**75**		
Track Count	**0**	**1**	**2**	**0**	**1**	**2**	**0**	**1**	**2**	**0**	**1**	**2**
# of Cells	65399	38272	26734	41814	23908	16420	25028	14101	9676	13255	7324	4947
POD	0.67	0.72	0.77	0.67	0.73	0.77	0.69	0.75	0.8	0.71	0.78	0.83
FAR	0.42	0.35	0.3	0.37	0.29	0.24	0.36	0.28	0.23	0.36	0.26	0.21
CSI	0.43	0.49	0.56	0.45	0.53	0.6	0.47	0.56	0.63	0.49	0.59	0.67
FCST TIME	11.46	13.34	15.11	10.08	11.93	13.76	9.23	11.07	12.62	8.84	10.86	12.17

Table 3.2. Forecast statistics using the -15 °C isotherm for the entire dataset (1997 – 2006).

Environmental -15 C Level												
E15-30 dBz Test												
Within Dist	**150**			**125**			**100**			**75**		
Track Count	**0**	**1**	**2**	**0**	**1**	**2**	**0**	**1**	**2**	**0**	**1**	**2**
# of Cells	65399	38272	26734	41814	23908	16420	25028	14101	9676	13255	7324	4947
POD	0.86	0.9	0.93	0.87	0.91	0.94	0.87	0.92	0.95	0.89	0.93	0.96
FAR	0.52	0.44	0.38	0.5	0.41	0.34	0.49	0.4	0.33	0.47	0.36	0.29
CSI	0.44	0.52	0.59	0.45	0.55	0.63	0.47	0.57	0.65	0.48	0.6	0.68
FCST TIME	15.43	17.87	20.03	13.8	16.2	18.49	12.58	14.96	16.9	11.89	14.5	16.05
E15-35 dBz Test												
Within Dist	**150**			**125**			**100**			**75**		
Track Count	**0**	**1**	**2**	**0**	**1**	**2**	**0**	**1**	**2**	**0**	**1**	**2**
# of Cells	65399	38272	26734	41814	23908	16420	25028	14101	9676	13255	7324	4947
POD	0.73	0.79	0.83	0.74	0.8	0.84	0.75	0.82	0.86	0.76	0.82	0.87
FAR	0.43	0.36	0.3	0.4	0.32	0.26	0.39	0.3	0.25	0.39	0.29	0.23
CSI	0.45	0.53	0.6	0.47	0.56	0.64	0.49	0.59	0.66	0.5	0.6	0.68
FCST TIME	12.46	14.4	16.3	11.11	13.01	15.02	10.07	11.97	13.74	9.56	11.71	13.09
E15-40 dBz Test												
Within Dist	**150**			**125**			**100**			**75**		
Track Count	**0**	**1**	**2**	**0**	**1**	**2**	**0**	**1**	**2**	**0**	**1**	**2**
# of Cells	65399	38272	26734	41814	23908	16420	25028	14101	9676	13255	7324	4947
POD	0.52	0.57	0.61	0.52	0.58	0.62	0.54	0.6	0.64	0.56	0.63	0.69
FAR	0.31	0.25	0.22	0.27	0.21	0.16	0.27	0.2	0.16	0.26	0.18	0.13
CSI	0.39	0.45	0.5	0.41	0.48	0.53	0.43	0.5	0.56	0.45	0.54	0.6
FCST TIME	7.99	9.29	10.72	7.05	8.34	9.85	6.36	7.67	8.95	6.19	7.66	8.72

Table 3.3. Forecast statistics using the -20 °C isotherm for the entire dataset (1997 – 2006).

Environmental -20 C Level												
E20-30 dBz Test												
Within Dist	**150**			**125**			**100**			**75**		
Track Count	**0**	**1**	**2**	**0**	**1**	**2**	**0**	**1**	**2**	**0**	**1**	**2**
# of Cells	65399	38272	26734	41814	23908	16420	25028	14101	9676	13255	7324	4947
POD	0.77	0.83	0.87	0.77	0.83	0.87	0.79	0.85	0.89	0.8	0.86	0.9
FAR	0.41	0.35	0.3	0.37	0.3	0.25	0.37	0.3	0.25	0.36	0.28	0.23
CSI	0.48	0.56	0.62	0.51	0.6	0.67	0.52	0.62	0.69	0.54	0.64	0.71
FCST TIME	13.04	15.13	17.08	11.54	13.58	15.59	10.45	12.48	14.23	9.92	12.13	13.54
E20-35 dBz Test												
Within Dist	**150**			**125**			**100**			**75**		
Track Count	**0**	**1**	**2**	**0**	**1**	**2**	**0**	**1**	**2**	**0**	**1**	**2**
# of Cells	65399	38272	26734	41814	23908	16420	25028	14101	9676	13255	7324	4947
POD	0.57	0.62	0.67	0.57	0.63	0.68	0.58	0.64	0.69	0.6	0.67	0.73
FAR	0.31	0.25	0.22	0.25	0.19	0.15	0.24	0.17	0.13	0.24	0.16	0.13
CSI	0.43	0.49	0.55	0.46	0.52	0.59	0.47	0.55	0.62	0.49	0.58	0.65
FCST TIME	8.67	10.09	11.55	7.33	8.69	10.18	6.64	8.06	9.36	6.39	8.03	9.06
E20-40 dBz Test												
Within Dist	**150**			**125**			**100**			**75**		
Track Count	**0**	**1**	**2**	**0**	**1**	**2**	**0**	**1**	**2**	**0**	**1**	**2**
# of Cells	65399	38272	26734	41814	23908	16420	25028	14101	9676	13255	7324	4947
POD	0.32	0.35	0.39	0.32	0.35	0.39	0.32	0.36	0.39	0.33	0.38	0.43
FAR	0.22	0.17	0.15	0.15	0.1	0.08	0.14	0.07	0.06	0.15	0.07	0.06
CSI	0.28	0.31	0.35	0.29	0.33	0.36	0.29	0.34	0.38	0.31	0.36	0.41
FCST TIME	4.23	4.96	5.89	3.44	4.09	4.99	3.11	3.83	4.57	3.08	3.9	4.53

Table 3.4. Forecast statistics using the -10 °C updraft isotherm for the entire dataset (1997 – 2006).

Updraft -10 C Level												
U10-30 dBz Test												
Within Dist	**150**			**125**			**100**			**75**		
Track Count	**0**	**1**	**2**	**0**	**1**	**2**	**0**	**1**	**2**	**0**	**1**	**2**
# of Cells	65399	38272	26734	41814	23908	16420	25028	14101	9676	13255	7324	4947
POD	0.85	0.9	0.93	0.86	0.91	0.94	0.87	0.92	0.95	0.88	0.93	0.96
FAR	0.53	0.45	0.39	0.51	0.42	0.35	0.5	0.41	0.34	0.49	0.38	0.31
CSI	0.43	0.51	0.58	0.44	0.54	0.62	0.46	0.56	0.64	0.47	0.58	0.66
FCST TIME	15.6	18.09	20.27	13.94	16.38	18.7	12.72	15.12	17.13	11.97	14.63	16.22
U10-35 dBz Test												
Within Dist	**150**			**125**			**100**			**75**		
Track Count	**0**	**1**	**2**	**0**	**1**	**2**	**0**	**1**	**2**	**0**	**1**	**2**
# of Cells	65399	38272	26734	41814	23908	16420	25028	14101	9676	13255	7324	4947
POD	0.72	0.78	0.82	0.73	0.79	0.84	0.75	0.81	0.86	0.76	0.82	0.87
FAR	0.44	0.37	0.32	0.42	0.34	0.27	0.4	0.32	0.26	0.4	0.3	0.25
CSI	0.44	0.51	0.58	0.45	0.54	0.62	0.48	0.58	0.65	0.49	0.59	0.67
FCST TIME	12.62	14.65	16.57	11.23	13.17	15.18	10.22	12.14	13.95	9.61	11.83	13.24
U10-40 dBz Test												
Within Dist	**150**			**125**			**100**			**75**		
Track Count	**0**	**1**	**2**	**0**	**1**	**2**	**0**	**1**	**2**	**0**	**1**	**2**
# of Cells	65399	38272	26734	41814	23908	16420	25028	14101	9676	13255	7324	4947
POD	0.52	0.56	0.61	0.52	0.57	0.62	0.54	0.61	0.65	0.56	0.63	0.69
FAR	0.33	0.27	0.23	0.28	0.22	0.17	0.28	0.21	0.16	0.28	0.19	0.14
CSI	0.38	0.44	0.49	0.4	0.47	0.52	0.43	0.5	0.56	0.44	0.53	0.6
FCST TIME	8.16	9.51	10.98	7.06	8.34	9.88	6.4	7.68	9.09	6.23	7.71	8.87

Table 3.5. Results from previous studies. * represents when the criteria must be met for at least two scans. ** represents when using the updraft temperature level.

Study	Num. of Cells	Criteria		POD	FAR	CSI	Lead Time
		Reflectivity	Isotherm				
Buechler and Goodman (1990)	20	40 dBZ	-10	1.00	0.20	0.80	4-33 minutes
Michimoto (1991)		30 dBZ	-20				5 minutes
Hondl and Eilts (1994)	23	10 dBZ	-10	1.00	0.18	0.82	15 minutes
Gremillion and Orville (1999)*	39	35 dBZ	-10	0.88	0.20	0.72	7.5 minutes
		40 dBZ	-10	0.84	0.07	0.79	7.5 minutes
		45 dBZ	-10	0.29	0.00	0.29	12.5 minutes
		25 dBZ	-15	0.84	0.24	0.67	14.8 minutes
		30 dBZ	-15	0.81	0.14	0.71	12.5 minutes
		35 dBZ	-15	0.70	0.16	0.62	6.0 minutes
		20 dBZ	-20	0.81	0.26	0.63	10.5 minutes
		25 dBZ	-20	0.71	0.15	0.63	9.3 minutes
		30 dBZ	-20	0.52	0.20	0.46	8.0 minutes
Vincent et al (2003)	50	35 dBZ	-10	1.00	0.41	0.59	17.5 minutes
		35 dBZ	-15	0.93	0.37	0.60	14.6 minutes
		40 dBZ	-10	1.00	0.37	0.61	14.7 minutes
		40 dBZ	-15	0.86	0.31	0.63	11.0 minutes
		35 dBZ*	-10	0.93	0.37	0.60	13.1 minutes
		35 dBZ*	-15	0.76	0.37	0.52	8.7 minutes
		40 dBZ*	-10	0.83	0.37	0.56	8.9 minutes
		40 dBZ*	-15	0.62	0.31	0.49	7.7 minutes
Wolf (2006)	1,100	40 dBZ**	-6	0.99	0.20	0.79	n/a
		40 dBZ**	-10	0.96	0.11	0.86	n/a
Clements and Orville (2008)	37	30 dBZ	-10				16.14 minutes
		40 dBZ	-10				12.07 minutes

Table 3.6. Comparison of the result from Gremillion and Orville (1999; GO) to the results from this study. NOTE: Criteria for GO must be met for at least two consecutive scans.

Criteria		POD		FAR		CSI	
dBZ Test Value	**Isotherm**	**GO**	**This Study**	**GO**	**This Study**	**GO**	**This Study**
35 dBZ	-10	0.88	0.89	0.20	0.41	0.72	0.55
40 dBZ	-10	0.84	0.74	0.07	0.31	0.79	0.54
45 dBZ	-10	0.29	n/a	0.00	n/a	0.29	n/a
25 dBZ	-15	0.84	n/a	0.24	n/a	0.67	n/a
30 dBZ	-15	0.81	0.91	0.14	0.41	0.71	0.55
35 dBZ	-15	0.70	0.80	0.16	0.33	0.62	0.56
20 dBZ	-20	0.81	n/a	0.26	n/a	0.63	n/a
25 dBZ	-20	0.71	n/a	0.15	n/a	0.63	n/a
30 dBZ	-20	0.52	0.84	0.20	0.32	0.46	0.60

Table 3.7. Comparison of the results from Vicent et al. (2003; V) to the results from the study.

Criteria		POD		FAR		CSI	
dBZ Test Value	Isotherm	V	This Study	V	This Study	V	This Study
35 dBZ	-10	1.00	0.89	0.41	0.41	0.59	0.56
40 dBZ	-10	1.00	0.74	0.37	0.31	0.61	0.54
35 dBZ	-15	0.93	0.80	0.37	0.33	0.60	0.56
40 dBZ	-15	0.86	0.60	0.31	0.22	0.63	0.49

Table 3.8. VII percentiles. VII values in kg m^{-2}.

1997-2006	
Percentile	**VII**
0	0.000
5	0.249
10	0.420
15	0.576
20	0.740
25	0.907
30	1.090
35	1.286
40	1.501
45	1.733
50	1.985
55	2.264
60	2.566
65	2.927
70	3.332
75	3.816
80	4.416
85	5.216
90	6.354
95	8.456
100	51.629

Table 3.9. Number of CG flashes correlated to different cell IDs for 11 June 2000.

June 11, 2000	
Cell ID	**# of Flashes**
0	22
1	39
2	44
3	8
4	110
5	61
6	61
7	75
8	24
9	78
10	75
11	14
12	0
13	23
14	14
15	1
16	26
17	6
18	0
19	0
20	0
21	24
22	7
23	0
24	0
25	0
26	0
27	3

Table 3.10. Same at Table 3.8 for 25 August 2000.

August 25, 2000	
Cell ID	**# of Flashes**
0	16
1	0
2	65
3	1
4	0
5	4

Table 3.11. Forecast statistics for -10 °C that result from analysis of 11 June 2000 when cells with a VII less than 2.56 kg m^{-2} are excluded at Only cells with a minimum track count of 2 are included.

Environmental -10 C Level				
E10-30 dBz Test				
Within Dist	**150**	**125**	**100**	**75**
Track Count	**2**	**2**	**2**	**2**
# of Cells	105	60	35	16
POD	0.59	0.75	0.75	1
FAR	0.28	0.18	0.25	0
CSI	0.48	0.64	0.6	1
E10-35 dBz Test				
Within Dist	**150**	**125**	**100**	**75**
Track Count	**2**	**2**	**2**	**2**
# of Cells	105	60	35	16
POD	0.59	0.75	0.75	1
FAR	0.28	0.18	0.25	0
CSI	0.48	0.64	0.6	1
E10-40 dBz Test				
Within Dist	**150**	**125**	**100**	**75**
Track Count	**2**	**2**	**2**	**2**
# of Cells	105	60	35	16
POD	0.59	0.75	0.75	1
FAR	0.28	0.18	0.25	0
CSI	0.48	0.64	0.6	1

Table 3.12. Same as Table 3.11 for -15 °C.

Environmental -15 C Level				
E15-30 dBz Test				
Within Dist	**150**	**125**	**100**	**75**
Track Count	**2**	**2**	**2**	**2**
# of Cells	105	60	35	16
POD	0.59	0.75	0.75	1
FAR	0.28	0.18	0.25	0
CSI	0.48	0.64	0.6	1
E15-35 dBz Test				
Within Dist	**150**	**125**	**100**	**75**
Track Count	**2**	**2**	**2**	**2**
# of Cells	105	60	35	16
POD	0.59	0.75	0.75	1
FAR	0.24	0.18	0.25	0
CSI	0.5	0.64	0.6	1
E15-40 dBz Test				
Within Dist	**150**	**125**	**100**	**75**
Track Count	**2**	**2**	**2**	**2**
# of Cells	105	60	35	16
POD	0.59	0.75	0.75	1
FAR	0.19	0.1	0.25	0
CSI	0.52	0.69	0.6	1

Table 3.13. Same as Table 3.11 for -20 °C.

Environmental -20 C Level				
E20-30 dBz Test				
Within Dist	**150**	**125**	**100**	**75**
Track Count	**2**	**2**	**2**	**2**
# of Cells	105	60	35	16
POD	0.59	0.75	0.75	1
FAR	0.28	0.18	0.25	0
CSI	0.48	0.64	0.6	1
E20-35 dBz Test				
Within Dist	**150**	**125**	**100**	**75**
Track Count	**2**	**2**	**2**	**2**
# of Cells	105	60	35	16
POD	0.5	0.67	0.75	1
FAR	0.15	0.11	0	0
CSI	0.46	0.62	0.75	1
E20-40 dBz Test				
Within Dist	**150**	**125**	**100**	**75**
Track Count	**2**	**2**	**2**	**2**
# of Cells	105	60	35	16
POD	0.29	0.5	0.5	1
FAR	0.14	0	0	0
CSI	0.27	0.5	0.5	1

Table 3.14. Same as Table 3.11 for updraft -10 °C.

Updraft -10 C Level				
U10-30 dBz Test				
Within Dist	**150**	**125**	**100**	**75**
Track Count	**2**	**2**	**2**	**2**
# of Cells	105	60	35	16
POD	0.59	0.75	0.75	1
FAR	0.28	0.18	0.25	0
CSI	0.48	0.64	0.6	1
U10-35 dBz Test				
Within Dist	**150**	**125**	**100**	**75**
Track Count	**2**	**2**	**2**	**2**
# of Cells	105	60	35	16
POD	0.59	0.75	0.75	1
FAR	0.24	0.18	0.25	0
CSI	0.5	0.64	0.6	1
U10-40 dBz Test				
Within Dist	**150**	**125**	**100**	**75**
Track Count	**2**	**2**	**2**	**2**
# of Cells	105	60	35	16
POD	0.59	0.75	0.75	1
FAR	0.19	0.1	0.25	0
CSI	0.52	0.69	0.6	1

Table 3.15. Forecast statistics for -10 °C that result from 11 June 2000 when cells with a VII less than 1.09 kg m^{-2} are excluded. Only cells with a minimum track count of 2 are included.

Environmental -10 C Level				
E10-30 dBz Test				
Within Dist	**150**	**125**	**100**	**75**
Track Count	**2**	**2**	**2**	**2**
# of Cells	105	60	35	16
POD	0.8	0.77	0.8	1
FAR	0.67	0.71	0.76	0.88
CSI	0.31	0.27	0.22	0.13
E10-35 dBz Test				
Within Dist	**150**	**125**	**100**	**75**
Track Count	**2**	**2**	**2**	**2**
# of Cells	105	60	35	16
POD	0.8	0.77	0.8	1
FAR	0.67	0.71	0.76	0.88
CSI	0.31	0.27	0.22	0.13
E10-40 dBz Test				
Within Dist	**150**	**125**	**100**	**75**
Track Count	**2**	**2**	**2**	**2**
# of Cells	105	60	35	16
POD	0.8	0.77	0.8	1
FAR	0.64	0.67	0.73	0.86
CSI	0.33	0.3	0.25	0.14

Table 3.16. Same as Table 3.15 for -15 °C.

Environmental -15 C Level				
E15-30 dBz Test				
Within Dist	**150**	**125**	**100**	**75**
Track Count	**2**	**2**	**2**	**2**
# of Cells	105	60	35	16
POD	0.8	0.77	0.8	1
FAR	0.64	0.68	0.73	0.88
CSI	0.33	0.29	0.25	0.13
E15-35 dBz Test				
Within Dist	**150**	**125**	**100**	**75**
Track Count	**2**	**2**	**2**	**2**
# of Cells	105	60	35	16
POD	0.8	0.77	0.8	1
FAR	0.57	0.64	0.69	0.86
CSI	0.38	0.32	0.29	0.14
E15-40 dBz Test				
Within Dist	**150**	**125**	**100**	**75**
Track Count	**2**	**2**	**2**	**2**
# of Cells	105	60	35	16
POD	0.79	0.75	0.75	1
FAR	0.44	0.4	0.57	0.67
CSI	0.49	0.5	0.38	0.33

Table 3.17. Same as Table 3.15 for -20 °C.

Environmental -20 C Level				
E20-30 dBz Test				
Within Dist	**150**	**125**	**100**	**75**
Track Count	**2**	**2**	**2**	**2**
# of Cells	105	60	35	16
POD	0.8	0.77	0.8	1
FAR	0.55	0.55	0.64	0.8
CSI	0.41	0.4	0.33	0.2
E20-35 dBz Test				
Within Dist	**150**	**125**	**100**	**75**
Track Count	**2**	**2**	**2**	**2**
# of Cells	105	60	35	16
POD	0.65	0.67	0.75	1
FAR	0.41	0.38	0.4	0.5
CSI	0.45	0.47	0.5	0.5
E20-40 dBz Test				
Within Dist	**150**	**125**	**100**	**75**
Track Count	**2**	**2**	**2**	**2**
# of Cells	105	60	35	16
POD	0.38	0.5	0.5	1
FAR	0.27	0	0	0
CSI	0.33	0.5	0.5	1

Table 3.18. Same as Table 3.15 for updraft -10°C.

Updraft -10 C Level				
U10-30 dBz Test				
Within Dist	**150**	**125**	**100**	**75**
Track Count	**2**	**2**	**2**	**2**
# of Cells	105	60	35	16
POD	0.8	0.77	0.8	1
FAR	0.64	0.68	0.73	0.88
CSI	0.33	0.29	0.25	0.13
U10-35 dBz Test				
Within Dist	**150**	**125**	**100**	**75**
Track Count	**2**	**2**	**2**	**2**
# of Cells	105	60	35	16
POD	0.8	0.77	0.8	1
FAR	0.57	0.64	0.69	0.86
CSI	0.38	0.32	0.29	0.14
U10-40 dBz Test				
Within Dist	**150**	**125**	**100**	**75**
Track Count	**2**	**2**	**2**	**2**
# of Cells	105	60	35	16
POD	0.79	0.75	0.75	1
FAR	0.44	0.4	0.57	0.67
CSI	0.49	0.5	0.38	0.33

Table 3.19. Average CSI values when using different percentile VII test values.

	June	July	August	All
Percentile				
None	0.566	0.572	0.600	0.583
10th	0.568	0.565	0.588	0.577
20th	0.579	0.575	0.588	0.580
30th	0.574	0.586	0.563	0.574
40th	0.581	0.556	0.494	0.533
60th	0.493	0.424	0.360	0.409

Table A.1. 1.0 km vertical resolution forecast statistics and lead times for August 2006 using the -10 ºC environmental level criteria.

Environmental -10 C Level												
E10,30 dBz Test												
Within Dist	**150**			**125**			**100**			**75**		
Track Count	**0**	**1**	**2**	**0**	**1**	**2**	**0**	**1**	**2**	**0**	**1**	**2**
# of Cells	2351	1379	946	1622	939	650	1038	593	406	582	323	220
POD	0.88	0.91	0.92	0.85	0.88	0.89	0.83	0.89	0.93	0.87	0.93	0.88
FAR	0.60	0.51	0.41	0.56	0.45	0.36	0.53	0.43	0.32	0.54	0.33	0.26
CSI	0.38	0.48	0.57	0.42	0.54	0.63	0.41	0.56	0.66	0.44	0.66	0.72
FCST TIME	16.39	18.66	21.23	13.33	15.68	17.72	12.64	15.63	19.17	13.71	16.99	19.55
E10,35 dBz Test												
Within Dist	**150**			**125**			**100**			**75**		
Track Count	**0**	**1**	**2**	**0**	**1**	**2**	**0**	**1**	**2**	**0**	**1**	**2**
# of Cells	2351	1379	946	1622	939	650	1038	593	406	582	323	220
POD	0.80	0.86	0.87	0.78	0.82	0.83	0.76	0.84	0.89	0.80	0.87	0.83
FAR	0.54	0.45	0.37	0.50	0.40	0.33	0.47	0.32	0.28	0.43	0.28	0.25
CSI	0.42	0.51	0.59	0.45	0.56	0.63	0.45	0.60	0.68	0.47	0.66	0.70
FCST TIME	14.63	16.68	19.23	11.81	13.93	16.07	11.13	13.83	17.33	12.15	15.11	17.88
E10,40 dBz Test												
Within Dist	**150**			**125**			**100**			**75**		
Track Count	**0**	**1**	**2**	**0**	**1**	**2**	**0**	**1**	**2**	**0**	**1**	**2**
# of Cells	2351	1379	946	1622	939	650	1038	593	406	582	323	220
POD	0.66	0.71	0.74	0.64	0.68	0.71	0.59	0.66	0.70	0.62	0.63	0.65
FAR	0.41	0.33	0.28	0.37	0.30	0.24	0.33	0.26	0.25	0.34	0.27	0.18
CSI	0.42	0.50	0.55	0.45	0.52	0.57	0.45	0.54	0.59	0.47	0.51	0.54
FCST TIME	10.62	12.14	14.09	8.34	9.87	11.47	7.63	9.57	12.12	8.78	11.00	13.39

Table A.2. Same as Table A.1 for -15 ºC.

Environmental -15 C Level												
E15,30 dBz Test												
Within Dist	**150**			**125**			**100**			**75**		
Track Count	**0**	**1**	**2**	**0**	**1**	**2**	**0**	**1**	**2**	**0**	**1**	**2**
# of Cells	2351	1379	946	1622	939	650	1038	593	406	582	323	220
POD	0.85	0.88	0.90	0.83	0.85	0.86	0.80	0.86	0.90	0.83	0.87	0.82
FAR	0.58	0.49	0.40	0.54	0.43	0.35	0.52	0.42	0.32	0.52	0.31	0.26
CSI	0.39	0.49	0.58	0.43	0.54	0.62	0.42	0.55	0.64	0.45	0.61	0.66
FCST TIME	15.66	17.84	20.30	12.61	14.84	16.76	11.87	14.69	18.02	13.04	16.13	18.83
E15,35 dBz Test												
Within Dist	**150**			**125**			**100**			**75**		
Track Count	**0**	**1**	**2**	**0**	**1**	**2**	**0**	**1**	**2**	**0**	**1**	**2**
# of Cells	2351	1379	946	1622	939	650	1038	593	406	582	323	220
POD	0.73	0.78	0.81	0.72	0.76	0.77	0.70	0.77	0.81	0.71	0.75	0.71
FAR	0.51	0.43	0.35	0.47	0.38	0.31	0.42	0.29	0.25	0.40	0.27	0.24
CSI	0.41	0.49	0.57	0.45	0.54	0.59	0.46	0.57	0.64	0.45	0.57	0.59
FCST TIME	13.55	15.45	17.77	10.91	12.87	14.81	10.34	12.82	16.09	11.45	14.20	16.93
E15,40 dBz Test												
Within Dist	**150**			**125**			**100**			**75**		
Track Count	**0**	**1**	**2**	**0**	**1**	**2**	**0**	**1**	**2**	**0**	**1**	**2**
# of Cells	2351	1379	946	1622	939	650	1038	593	406	582	323	220
POD	0.57	0.62	0.66	0.56	0.60	0.63	0.52	0.59	0.63	0.52	0.57	0.59
FAR	0.37	0.31	0.27	0.34	0.27	0.23	0.29	0.24	0.23	0.29	0.23	0.15
CSI	0.39	0.45	0.50	0.42	0.47	0.52	0.41	0.48	0.54	0.40	0.46	0.50
FCST TIME	9.32	10.64	12.28	7.10	8.42	9.70	6.47	8.14	10.17	7.40	9.30	11.43

Table A.3. Same as Table A.1 for -20 ºC.

Environmental -20 C Level												
E20,30 dBz Test												
Within Dist	**150**			**125**			**100**			**75**		
Track Count	**0**	**1**	**2**	**0**	**1**	**2**	**0**	**1**	**2**	**0**	**1**	**2**
# of Cells	2351	1379	946	1622	939	650	1038	593	406	582	323	220
POD	0.80	0.84	0.87	0.78	0.81	0.83	0.76	0.82	0.87	0.78	0.83	0.79
FAR	0.49	0.41	0.35	0.46	0.36	0.31	0.43	0.30	0.26	0.43	0.26	0.23
CSI	0.46	0.54	0.61	0.49	0.59	0.64	0.48	0.60	0.68	0.49	0.63	0.66
FCST TIME	14.38	16.36	18.79	11.25	13.25	15.23	10.47	12.91	16.10	11.39	13.98	16.57
E20,35 dBz Test												
Within Dist	**150**			**125**			**100**			**75**		
Track Count	**0**	**1**	**2**	**0**	**1**	**2**	**0**	**1**	**2**	**0**	**1**	**2**
# of Cells	2351	1379	946	1622	939	650	1038	593	406	582	323	220
POD	0.66	0.70	0.75	0.65	0.68	0.71	0.61	0.67	0.73	0.63	0.67	0.64
FAR	0.35	0.29	0.20	0.26	0.20	0.16	0.21	0.16	0.14	0.22	0.14	0.10
CSI	0.49	0.55	0.62	0.50	0.56	0.60	0.50	0.57	0.63	0.49	0.58	0.56
FCST TIME	11.34	12.92	15.03	8.47	10.05	11.77	8.11	10.02	12.94	8.38	10.48	13.11
E20,40 dBz Test												
Within Dist	**150**			**125**			**100**			**75**		
Track Count	**0**	**1**	**2**	**0**	**1**	**2**	**0**	**1**	**2**	**0**	**1**	**2**
# of Cells	2351	1379	946	1622	939	650	1038	593	406	582	323	220
POD	0.44	0.47	0.52	0.43	0.46	0.48	0.36	0.41	0.44	0.36	0.40	0.42
FAR	0.20	0.15	0.13	0.15	0.09	0.07	0.15	0.09	0.08	0.18	0.10	0.08
CSI	0.39	0.44	0.47	0.40	0.44	0.46	0.34	0.39	0.42	0.35	0.39	0.41
FCST TIME	5.72	6.55	7.69	3.47	4.22	4.79	2.95	3.69	4.80	3.45	4.63	6.15

Table A.4. Same as Table A.1 for updraft -10 ºC.

Updraft -10 C Level												
U10,30 dBz Test												
Within Dist	**150**			**125**			**100**			**75**		
Track Count	**0**	**1**	**2**	**0**	**1**	**2**	**0**	**1**	**2**	**0**	**1**	**2**
# of Cells	2351	1379	946	1622	939	650	1038	593	406	582	323	220
POD	0.86	0.89	0.91	0.84	0.86	0.87	0.81	0.87	0.92	0.84	0.88	0.83
FAR	0.60	0.50	0.41	0.55	0.44	0.35	0.52	0.42	0.32	0.53	0.32	0.26
CSI	0.38	0.48	0.57	0.43	0.54	0.63	0.42	0.56	0.66	0.45	0.62	0.67
FCST TIME	16.13	18.35	20.81	13.16	15.44	17.40	12.47	15.36	18.75	13.60	16.77	19.32
U10,35 dBz Test												
Within Dist	**150**			**125**			**100**			**75**		
Track Count	**0**	**1**	**2**	**0**	**1**	**2**	**0**	**1**	**2**	**0**	**1**	**2**
# of Cells	2351	1379	946	1622	939	650	1038	593	406	582	323	220
POD	0.76	0.81	0.85	0.75	0.79	0.81	0.73	0.80	0.85	0.75	0.80	0.76
FAR	0.52	0.43	0.35	0.47	0.37	0.31	0.42	0.30	0.26	0.40	0.27	0.24
CSI	0.42	0.51	0.59	0.47	0.56	0.62	0.48	0.60	0.68	0.48	0.61	0.63
FCST TIME	14.25	16.24	18.66	11.59	13.65	15.71	10.94	13.54	16.91	11.94	14.79	17.55
U10,40 dBz Test												
Within Dist	**150**			**125**			**100**			**75**		
Track Count	**0**	**1**	**2**	**0**	**1**	**2**	**0**	**1**	**2**	**0**	**1**	**2**
# of Cells	2351	1379	946	1622	939	650	1038	593	406	582	323	220
POD	0.61	0.67	0.71	0.60	0.65	0.67	0.56	0.63	0.67	0.57	0.62	0.63
FAR	0.38	0.31	0.26	0.34	0.28	0.24	0.30	0.25	0.24	0.31	0.24	0.17
CSI	0.42	0.48	0.54	0.45	0.51	0.55	0.45	0.53	0.58	0.45	0.51	0.54
FCST TIME	10.20	11.63	13.47	7.93	9.36	10.85	7.10	8.80	11.14	8.20	10.27	12.54

Table A.5. 0.5 km vertical resolution forecast statistics and lead times for August 2006 using the -10 ºC environmental level criteria.

Environmental -10 C Level												
E10,30 dBz Test												
Within Dist	**150**			**125**			**100**			**75**		
Track Count	**0**	**1**	**2**	**0**	**1**	**2**	**0**	**1**	**2**	**0**	**1**	**2**
# of Cells	4110	1510	1050	2907	978	700	1858	543	390	1096	267	192
POD	0.93	0.95	0.95	0.88	0.9	0.91	0.84	0.9	0.95	0.81	0.89	0.9
FAR	0.69	0.53	0.45	0.66	0.45	0.37	0.67	0.42	0.33	0.66	0.36	0.3
CSI	0.3	0.47	0.55	0.33	0.54	0.62	0.32	0.57	0.66	0.33	0.63	0.7
FCST TIME	14.74	17.87	20.27	11.98	14.73	16.85	11.66	14.77	17.79	11.27	14.78	16.85
E10,35 dBz Test												
Within Dist	**150**			**125**			**100**			**75**		
Track Count	**0**	**1**	**2**	**0**	**1**	**2**	**0**	**1**	**2**	**0**	**1**	**2**
# of Cells	4110	1510	1050	2907	978	700	1858	543	390	1096	267	192
POD	0.85	0.9	0.92	0.81	0.85	0.87	0.77	0.85	0.92	0.74	0.85	0.89
FAR	0.64	0.5	0.43	0.59	0.43	0.35	0.55	0.35	0.3	0.54	0.35	0.24
CSI	0.33	0.49	0.56	0.38	0.54	0.62	0.38	0.58	0.68	0.38	0.62	0.7
FCST TIME	13.61	16.55	18.95	10.98	13.52	15.72	10.64	13.55	16.45	10.17	13.41	15.39
E10,40 dBz Test												
Within Dist	**150**			**125**			**100**			**75**		
Track Count	**0**	**1**	**2**	**0**	**1**	**2**	**0**	**1**	**2**	**0**	**1**	**2**
# of Cells	4110	1510	1050	2907	978	700	1858	543	390	1096	267	192
POD	0.67	0.78	0.83	0.64	0.73	0.78	0.59	0.7	0.8	0.55	0.68	0.73
FAR	0.55	0.41	0.31	0.48	0.3	0.25	0.45	0.28	0.26	0.48	0.27	0.19
CSI	0.37	0.51	0.58	0.4	0.55	0.61	0.38	0.55	0.65	0.35	0.56	0.62
FCST TIME	11.16	13.69	15.91	9.08	11.21	13.27	8.69	11.15	13.87	8.15	10.85	12.66

Table A.6. Same as Table A.5 for -15 ºC.

Environmental -15 C Level												
E15,30 dBz Test												
Within Dist	**150**			**125**			**100**			**75**		
Track Count	**0**	**1**	**2**	**0**	**1**	**2**	**0**	**1**	**2**	**0**	**1**	**2**
# of Cells	4110	1510	1050	2907	978	700	1858	543	390	1096	267	192
POD	0.841	0.905	0.919	0.804	0.855	0.869	0.76	0.849	0.898	0.709	0.828	0.821
FAR	0.625	0.478	0.414	0.588	0.415	0.343	0.562	0.339	0.3	0.567	0.316	0.222
CSI	0.343	0.501	0.567	0.373	0.553	0.624	0.393	0.584	0.662	0.364	0.629	0.661
FCST TIME	13.37	16.17	18.59	10.52	12.89	15.08	10.06	12.72	15.79	9.258	12.04	14.68
E15,35 dBz Test												
Within Dist	**150**			**125**			**100**			**75**		
Track Count	**0**	**1**	**2**	**0**	**1**	**2**	**0**	**1**	**2**	**0**	**1**	**2**
# of Cells	4110	1510	1050	2907	978	700	1858	543	390	1096	267	192
POD	0.674	0.786	0.834	0.655	0.741	0.781	0.611	0.718	0.804	0.552	0.682	0.707
FAR	0.542	0.391	0.272	0.459	0.303	0.229	0.42	0.258	0.22	0.427	0.283	0.159
CSI	0.368	0.522	0.606	0.399	0.546	0.63	0.398	0.562	0.67	0.36	0.569	0.61
FCST TIME	11.36	13.84	16.02	8.827	10.88	12.92	8.499	10.81	13.58	7.715	10.11	12.54
E15,40 dBz Test												
Within Dist	**150**			**125**			**100**			**75**		
Track Count	**0**	**1**	**2**	**0**	**1**	**2**	**0**	**1**	**2**	**0**	**1**	**2**
# of Cells	4110	1510	1050	2907	978	700	1858	543	390	1096	267	192
POD	0.471	0.569	0.607	0.452	0.535	0.566	0.367	0.444	0.509	0.312	0.435	0.456
FAR	0.397	0.276	0.222	0.355	0.2	0.16	0.301	0.138	0.113	0.329	0.133	0.091
CSI	0.33	0.447	0.5	0.349	0.446	0.494	0.299	0.396	0.469	0.225	0.362	0.394
FCST TIME	6.638	8.245	9.55	4.702	5.848	6.893	4.261	5.556	6.794	3.855	5.122	6.386

Table A.7. Same as Table A.5 for -20 ºC.

Environmental -20 C Level												
E20,30 dBz Test												
Within Dist	150			125			100			75		
Track Count	0	1	2	0	1	2	0	1	2	0	1	2
# of Cells	4110	1510	1050	2907	978	700	1858	543	390	1096	267	192
POD	0.75	0.86	0.89	0.72	0.82	0.84	0.68	0.82	0.87	0.63	0.79	0.79
FAR	0.56	0.41	0.36	0.52	0.37	0.3	0.48	0.29	0.26	0.49	0.29	0.18
CSI	0.38	0.54	0.6	0.41	0.57	0.65	0.41	0.6	0.68	0.38	0.62	0.67
FCST TIME	12.37	15	17.39	9.52	11.73	13.88	9.06	11.5	14.29	8.24	10.75	13.13
E20,35 dBz Test												
Within Dist	150			125			100			75		
Track Count	0	1	2	0	1	2	0	1	2	0	1	2
# of Cells	4110	1510	1050	2907	978	700	1858	543	390	1096	267	192
POD	0.59	0.71	0.75	0.57	0.66	0.71	0.52	0.62	0.7	0.47	0.59	0.61
FAR	0.41	0.28	0.2	0.32	0.18	0.14	0.3	0.15	0.12	0.31	0.14	0.07
CSI	0.41	0.55	0.62	0.41	0.54	0.6	0.4	0.52	0.62	0.36	0.52	0.56
FCST TIME	9.3	11.4	13.23	6.95	8.61	10.28	6.52	8.33	10.48	5.75	7.52	9.3
E20,40 dBz Test												
Within Dist	150			125			100			75		
Track Count	0	1	2	0	1	2	0	1	2	0	1	2
# of Cells	4110	1510	1050	2907	978	700	1858	543	390	1096	267	192
POD	0.36	0.44	0.46	0.34	0.41	0.43	0.26	0.32	0.36	0.24	0.33	0.34
FAR	0.29	0.15	0.14	0.22	0.1	0.08	0.22	0.08	0.08	0.22	0.04	0.02
CSI	0.3	0.4	0.42	0.31	0.39	0.42	0.24	0.31	0.36	0.21	0.32	0.33
FCST TIME	4.77	5.96	6.7	3.02	3.78	4.23	2.87	3.74	4.31	2.65	3.43	4.5

Table A.8. Same as Table A.5 for updraft -10 ºC.

Updraft -10 C Level												
U10,30 dBz Test												
Within Dist	150			125			100			75		
Track Count	0	1	2	0	1	2	0	1	2	0	1	2
# of Cells	4110	1510	1050	2907	978	700	1858	543	390	1096	267	192
POD	0.86	0.91	0.93	0.81	0.87	0.88	0.78	0.86	0.91	0.72	0.84	0.84
FAR	0.64	0.49	0.43	0.61	0.43	0.35	0.61	0.39	0.31	0.61	0.33	0.26
CSI	0.33	0.49	0.56	0.36	0.55	0.62	0.36	0.58	0.66	0.36	0.63	0.67
FCST TIME	13.72	16.59	18.98	10.94	13.4	15.51	10.46	13.24	16.2	9.76	12.8	15.24
U10,35 dBz Test												
Within Dist	150			125			100			75		
Track Count	0	1	2	0	1	2	0	1	2	0	1	2
# of Cells	4110	1510	1050	2907	978	700	1858	543	390	1096	267	192
POD	0.7	0.81	0.85	0.67	0.76	0.8	0.63	0.74	0.83	0.58	0.72	0.74
FAR	0.57	0.42	0.35	0.53	0.37	0.3	0.45	0.28	0.24	0.46	0.3	0.18
CSI	0.36	0.51	0.59	0.39	0.54	0.62	0.4	0.57	0.67	0.37	0.59	0.63
FCST TIME	12.06	14.64	16.87	9.52	11.7	13.8	9.08	11.57	14.35	8.29	10.92	13.22
U10,40 dBz Test												
Within Dist	150			125			100			75		
Track Count	0	1	2	0	1	2	0	1	2	0	1	2
# of Cells	4110	1510	1050	2907	978	700	1858	543	390	1096	267	192
POD	0.51	0.61	0.65	0.48	0.57	0.6	0.4	0.47	0.54	0.35	0.47	0.49
FAR	0.43	0.32	0.26	0.38	0.26	0.22	0.35	0.19	0.17	0.37	0.14	0.09
CSI	0.34	0.46	0.51	0.36	0.47	0.52	0.31	0.41	0.49	0.25	0.39	0.43
FCST TIME	8.06	9.91	11.65	6.29	7.71	9.37	5.81	7.48	9.68	5.16	6.85	8.79

VITA

Name:	Richard Matthew Mosier
Address:	National Weather Service Dallas/Fort Worth, TX Weather Forecast Office 3401 Northern Cross Blvd. Fort Worth, TX 76137
Email Address:	Richard.Mosier@noaa.gov
Education:	B. S., Meteorology, Texas A&M University, 2007 M. S., Atmospheric Sciences, Texas A&M University, 2009